Chapter Four: Results, discussion and conclusion

4.1 CNF synthesis and proposed growth mechanism

The world's energy demands are increasing and 80% of these demands are being met by fossil fuels; 40% of this percentage is being met by coal [1]. Coal is abundant, geographically available and its cost can be easily predicted with changing economic conditions, thus it is an economically viable option for energy generation. According to the 2013 World Energy Council report, coal consumption is predicted to increase by 42.8% by the year 2020 [2]. Coal consumption generates fly ash in large quantities in pulverised coal power stations. In 2013 about 600 million tons of fly ash were produced worldwide; and so the production of fly ash is also expected to grow tremendously. In South Africa alone, 109 million tons of coal were consumed in 2013 and 25 million tons of ash (90% being fly ash) were produced. Of the total fly ash produced in South Africa that year only 1.2 million tons were sold to the cement and other industries [3]. The rest of the raw fly ash was stacked in huge dumps or slurry dams. It is reported that in the world at large, roughly 16% of the raw fly ash produced annually is used in further industry.

Attempting to understand the physical and chemical nature of fly ash is a challenging task because of its complexity. Visually fly ash is a grey, refractory and alkaline material [4]. Under light microscopy it is seen to consist of cenospheres (hollow spheres), plerospheres (filled with other spheres), stereaspheres (silicate solid spheres) and ferro-carbonaceous spheres (which contain Fe_xO_y and carbonaceous material in different proportions) [5]. While surveying the literature it is obvious that plerospheres (as they will be called in this study), have been called plenospheres by other researchers [6].

Fly ash particles and their formation processes have been studied before. It has been suggested that most non-spherical particles have not been exposed to high temperatures for long enough for them to melt and spherify [5]. South African fly ash is primarily made up of silica and aluminosilicates, iron oxides and small amounts of carbonaceous materials in some instances (**refer to Fig 1(a & b) in Appendix I**).

The primary minerals in fly ash are: SiO_2, Al_2O_3, Fe_2O_3, FeO, CaO, MgO and SO_3 with small amounts of unburnt angular carbo [7]. It should be noted that the chemical

composition of the raw fly ash will vary according to its geographical location. South African fly ash is classified as Class-F ash according to the American Society for Testing Materials (ASTM), because it has a low calcium content, which ranges from 1-12% in the form of hydroxides and sulphates. If it had a calcium hydroxide content ranging from 30-40% and great amounts of alkali earth minerals then it would be Class-C fly ash [4].

Fly ash has been used as: a pozzolan (also known as prozzolan i.e. to assist in the formation of cementitious materials), a filler for mines, a replacement for cement in the construction industry, as well as for the production of ceramics, lightweight aggregates and bricks [4], [8], [9]. It has also been used for soil enrichment [4], [8], [10]. Chemically it has been used to synthesise high cation exchange capacity zeolites for heavy metal sequestration and for water purification [11]. Metallurgists have managed to extract valuable minerals and metals from the ash like: alumina, silica, Al, [12] Si, Fe, Ge, Ga, V, Ni [8].

Other beneficial but non-commercialised uses of fly ash involve its application as a catalyst support for: hydrogen production, waste gas cleaning, as a catalyst for methane reformation and gas oxidation of volatile organic compounds [13], [14].

To date few researchers have reported the possibility of using fly ash as a catalyst or support for the synthesis of CNMs [13]-[18]. Fly ash can be used as a support for the synthesis of the CNFs because of the presence of minerals like: SiO_2 and Al_2O_3 which are common supports for their synthesis [14]. Dunens *et al*. managed to impregnate fly ash with Fe salts to synthesise CNTs using CVD [14]. In another case, Yasui *et al.* used Japanese fly ash (with ~5% of Fe_xO_y ($1 \leq x \leq 3$, $1 \leq y \leq 4$)) to synthesise MWCNTs using CVD [16]. Their conclusion was that Fe nanoparticles in the raw fly ash were responsible for the formation of the CNFs.

Salah *et al.* used heat treated fly ash in a low pressure environment to synthesise CNTs. They used acetylene as their carbon source and N_2 gas for their reducing environment at 750 °C. In a recent report Hintsho *et al.* indicated that they too were able to synthesise CNFs using acetylene as a carbon source at a temperature of 650 °C [19]. In this study a modified version of their method to synthesise CNFs was chosen. Raw South African fly ash has about 5% iron content, just as the Japanese fly ash used by Yasui *et al.* [16] and his colleagues produced nano-carbonaceous materials by the chemical

vapour deposition method (CVD); thus it seemed possible that the same could be done with South African fly ash.

CVD is a chemical synthesis technique where a gaseous carbon source is catalytically decomposed at moderate temperatures in a furnace, in the presence of a metal catalyst [14]. There are several types of furnaces in CVD: horizontal, vertical, fluidised bed reactor and plasma enhanced [20]. These furnaces have temperature ranges between 600 – 1200 °C. The carbon sources in this process are typically hydrocarbons (e.g. acetylene, methane, xylene, ethane, isobutene, ethanol and their mixtures [21]) because they decompose at low temperatures, however CO gas has been used too [22]. Such carbon sources are advantageous because they accommodate a variety of substrates [22] that can be used for templating the growth of CNFs [21].

It is accepted that straight CNFs grow through tip and root growth mechanisms in CVD [23] [24]. The hydrocarbon gas adsorbs, decomposes, dissolves and then the carbon species diffuses through the catalyst, followed by the precipitation of carbon on the opposite surface of the catalyst particle to form the nanofibres [25]. Although many may agree on this, Rodriguez *et al*. have shown that this approach is limited and doesn't account for more complex CNF structures.

This present study served to explore the growth mechanism CNFs on South African coal fly ash (CFA) in more detail as this has not been carried out in detail and systematically. All the following results chapters are laid out in publication format.

Experimental and characterisation

Synthesis of CNFs

Pristine CNFs were prepared by decomposing acetylene over raw fly ash particles using the CVD method. This work was done in a horizontal thermal furnace. The flow rate of the hydrocarbon gas and the hydrogen were 200 ml/min. The reaction was ramped from room temperature to 650 °C at a temperature gradient of 10 °C/min. The reaction was held at this temperature for an hour. The furnace was allowed to cool down to room temperature and the product was collected into sample vials.

To determine the growth mechanism, 2.5 g of the raw fly ash was loaded into the furnace in a quartz boat. The first reaction was allowed to run for 15 min under the above-mentioned conditions. It was allowed to cool down to room temperature from

150 °C. The product was collected into a sample vial and characterised thereafter. The proceeding reactions were performed in 10 min incremental intervals from the former reaction up to 125 min. From 65 min to 125 min the reaction was held at 650 °C.

The typical colour of the products from the reaction was grey to black, compared to the light grey colour of the raw fly ash, and the yield was always twice or above the amount of fly ash added by mass.

Characterisation

The phases of the minerals and elements present in the raw fly ash and CNFs were determined using powder X-ray diffraction (PXRD). The diffractometer used was the Bruker D2 PHASER with a LYNXEYE detector and a Co K_{α} source at 30 kV.

Surface area analyses were performed on the raw fly ash and on the pristine CNFs to compare them to each other. The surface area analyses were performed using a Micromeritics Tristar 3000 Brunauer-Emmett-Teller surface area analyser.

Laser Raman spectra were obtained for the products using the Bruker Senterra Dispersive Micro-Raman system which was equipped with a 532 nm line or the Horiba, Jobin-Yvon LabRAM Raman spectrometer equipped with a 514.5 nm line. The laser Raman provided information on the graphitic nature of the materials that were formed. Furthermore it provided information on the change of the type of carbon across the development of the pristine CNFs. Attenuated total reflection-Fourier transform infrared (ATR-FTIR) spectra were obtained for the as-synthesised CNFs using the Bruker Tensor 27 with a ZnSe window (500–6000 cm^{-1}). ATR-FTIR helped to deduce the presence of C=C bonds, which confirmed the formation of the CNFs.

Thermogravimetric analyses were performed on the raw fly ash and on the pristine CNFs to determine the amount of ash remaining in the product after synthesis. This analysis was performed using a Perkin-Elmer Simultaneous Thermal Analyser (STA 6000). X-ray fluorescence (XRF) elemental data was obtained using a Bruker S2 Ranger. This technique was used to characterise the raw fly ash and subsequently the CNFs that were formed, to estimate the variance of the elements before and after the synthesis of these.

For the morphology, chemical composition and visual particle size determination the FEI Tecnai T12 (TEM) working at 120 kV and equipped with an Oxford Inca system was

used. To further understand the surface characteristics of the materials the FEI Nova Nanolab 600 FIB/SEM (30 kV) was used.

Results and discussion

Characterisation of CNFs and fly ash

PXRD characterisation

PXRD patterns were obtained for the pristine CNFs and raw fly ash as seen in **Fig 4.1.1**. Haematite peaks were observed at 2θs of 28.10, 38.69, 41.6, and 78.50 and at 82.90° [26]. Carbon peaks were also observed at a 2θ angle of about 27° [27].

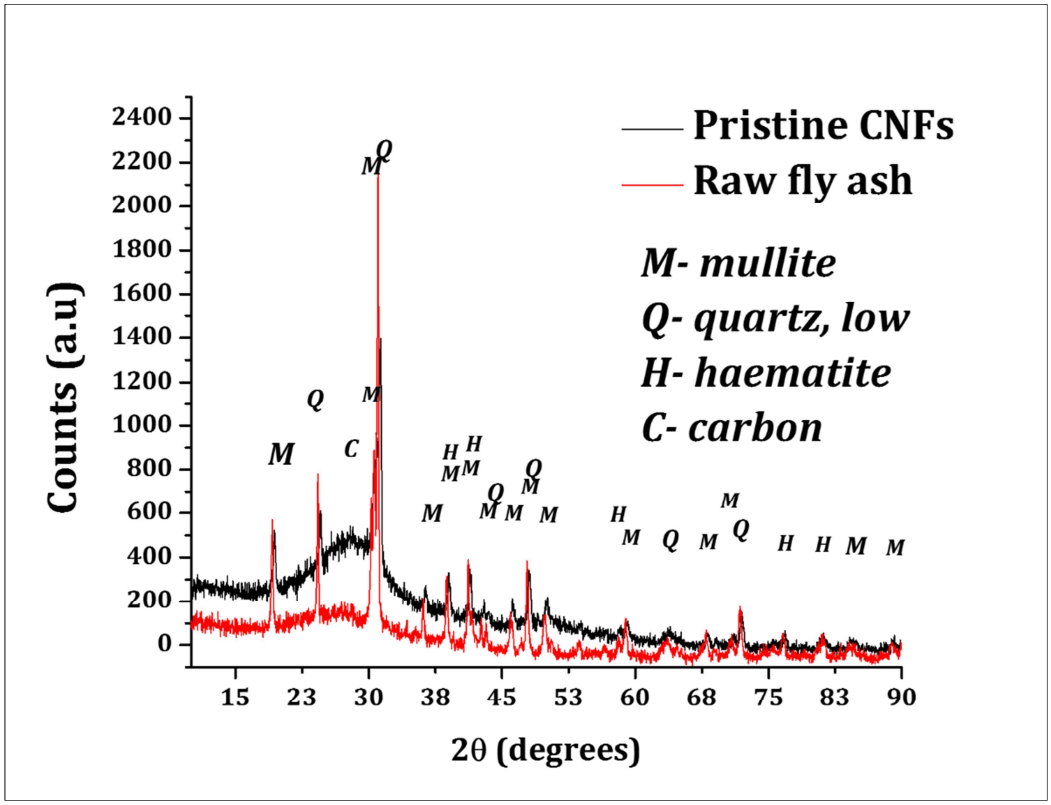

Figure 4.1.1: PXRD pattern of raw fly ash and pristine CNFs showing the presence of carbon in both materials.

The rest of the phases in both materials were due to the presence of mullite and quartz. Overall, the patterns for pristine CNFs and raw fly ash were not that different, but the counts of the mullite, quartz and haematite in the pristine CNFs, as compared to the raw fly ash sample, were low.

The carbon peak for the CNFs was broad and larger than that of the raw fly ash. This may imply that the carbon formed was predominantly amorphous or nanoparticulate.

The above observations showed that the CNFs that were synthesised still contained fly ash.

BET of the pristine CNFs and the raw fly ash

The colour of the product, yield and the PXRD suggested that a different product was formed on the initial raw fly ash. So, to further confirm this observation, surface area measurements of the raw fly ash and the pristine CNFs were taken. **Fig 4.1.2** shows linear isotherm plots that were obtained during N_2 adsorption measurements for both the raw fly ash (black) and the pristine CNFs (blue).

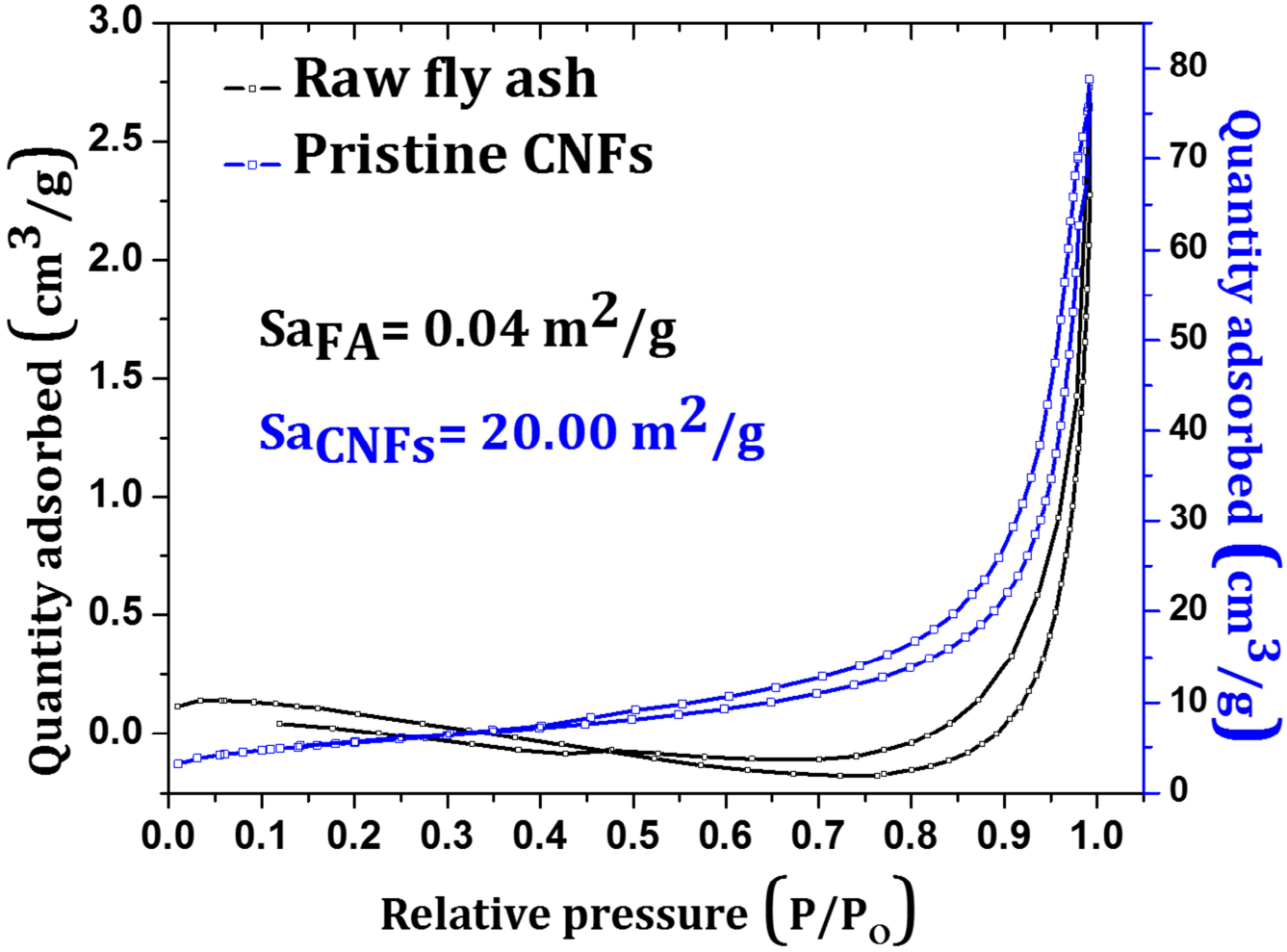

Figure 4.1.2: N_2 BET linear isotherms showing the low surface area of raw fly ash (black) as compared to pristine CNFs' (blue) one.

The isotherms showed type IV trends according to the IUPAC classification [28]. The formation of hysteresis loops at relative pressures above 0.4 indicated that a multilayer adsorption process, characteristic of a mesoporous material, had occurred for both raw fly ash and pristine CNFs [29]. The average BET surface areas of the raw fly ash and the

CNFs were 0.04 m^2/g and 20.00 m^2/g, respectively and this showed that a different product with a higher surface area was formed, namely CNFs.

Laser Raman spectroscopy characterisation

After the BET measurements were taken, the materials were further characterised using laser Raman spectroscopy to determine the graphitic nature of raw fly ash as compared to the pristine CNFs. Laser Raman spectra for the pristine CNFs (a) and the raw fly ash (b) clearly showed that both materials contained carbon because both the disordered (D) peak at 1343.9 cm^{-1} and graphitic (G) peak at 1635.2 cm^{-1} which were characteristic of carbon, were found to be present (**Fig 4.1.3** (**a-b**)).

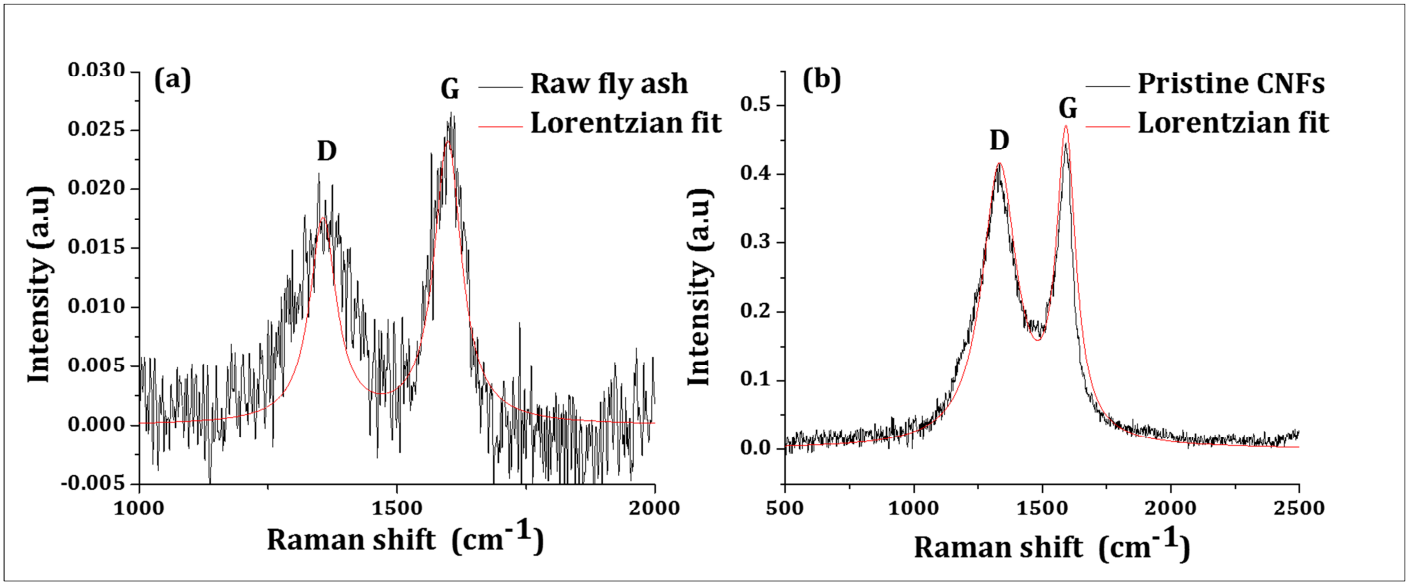

Figure 4.1.3: Laser Raman spectra of the raw fly ash (a) and the pristine CNFs (b) along with the sum of their Lorentzian curve fits showing the presence of carbon in both samples.

Blisset and Rowson have previously observed that fly ash contained angular carbonaceous material [30]. This explained the presence of the D and G carbon peaks in the raw fly ash used in this study. Some samples of fly ash that were studied didn't contain any carbonaceous material (refer to **Fig 1** (**c**) in **Appendix I**) hence the absence of the D and G bands.

The calculated I_G/I_D ratio of the raw fly ash was 1.25 and 1.13 for the pristine CNFs, respectively. This suggested that the angular carbon found in the raw fly ash had more long range order as compared to the pristine CNFs. This being the case, it was observed

that the overall intensity of the D and G peaks of the pristine CNFs was nearly 20 times greater than the ones for the raw fly ash. This observation confirmed the fact that more carbon was formed after the CVD treatment with C_2H_2 and H_2.

ATR-FTIR of the pristine CNFs and the raw fly ash

To further understand the chemical nature of the pristine CNFs, ATR-FTIR was performed on them and the raw fly ash. This was done to assess if there was any chemical bond vibration difference in the newly made carbon of the CNFs and that of the raw fly ash.

However, upon inspection of the ATR-FTIR spectra for the raw fly ash and the pristine CNFs, except for intensity, there was no difference in their band positions (**Fig 4.1.4** (**a-b**)).

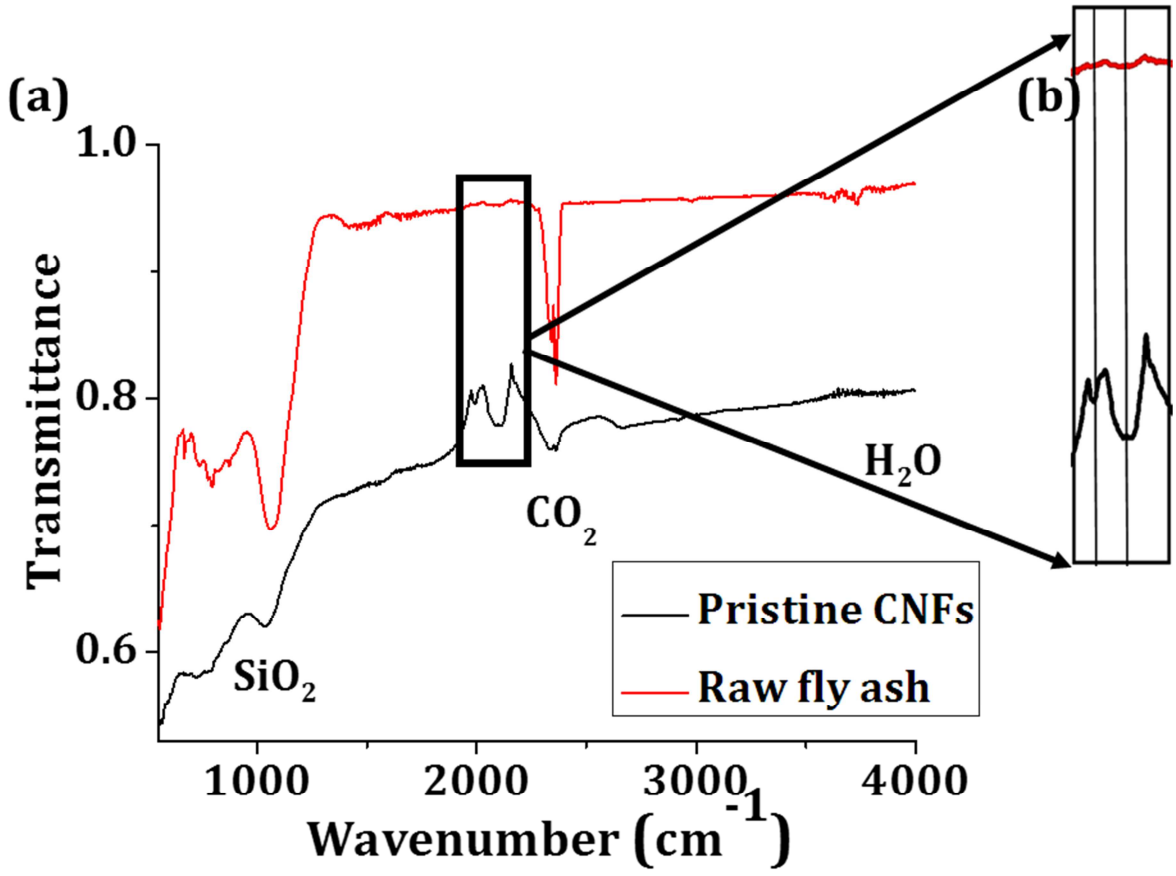

Figure 4.1.4: (a-b) The ATR-FTIR pattern of pristine CNFs and raw fly ash showing that pristine CNFs have the same bond vibrations as raw fly ash.

The difference in intensity as seen in the inset (**Fig 4.1.4** (**b**)) confirmed the observations obtained by laser Raman spectroscopy. This showed that after treatment with C_2H_2 and H_2 more carbonaceous materials (CNFs) were formed on the fly ash.

TGA of the pristine CNFs and the raw fly ash

TGA thermograms were obtained for raw fly ash and the pristine CNFs (**Fig 4.1.5** (**a**)) as well as their first derivative plots **Fig 4.1.5** (**b**).

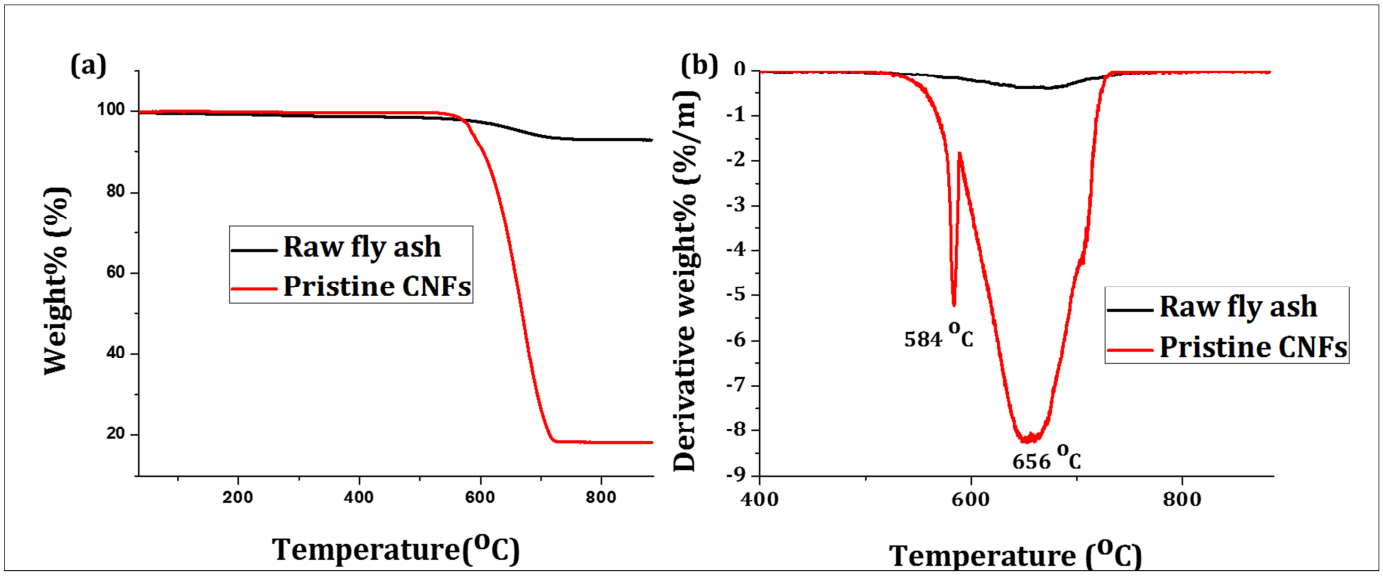

Figure 4.1.5: (a) TGA thermograms of the pristine CNFs and the raw fly ash and (b) first derivative curves showing their thermal decomposition temperatures.

The thermograms showed that raw fly ash lost 7% of its initial mass after combustion from room temperature to 900 °C, whereas pristine CNFs lost 82% of their initial mass under the same conditions. This observation suggested that roughly 75%, by mass, of the product after synthesis was carbon from the CNFs and 7% was carbon from the fly ash. The first derivative plot of the thermograms showed the temperature where there was the highest mass loss and this corresponded to 656 °C. This meant that the synthesised CNFs were thermally stable up to this temperature. Unlike the raw fly ash, a decomposition peak was observed at 584 °C in the pristine CNFs, which was sharp, indicating carbonaceous materials with a very small size range. This material was not identified in TEM, but may also be attributed to CNFs with smaller diameters [31].

XRF characterisation

Further characterisation using XRF spectroscopy was performed on the pristine CNFs and the raw fly ash to elucidate if any particular elements in the ash may have been responsible for the formation of the CNFs. The standard deviation for all the elements was less than 5% based on a repeat analysis of the standard USGS Andesite GV-2 sample. **Fig 4.1.6** shows the major elemental analyses that were obtained for the raw fly ash and the pristine CNFs.

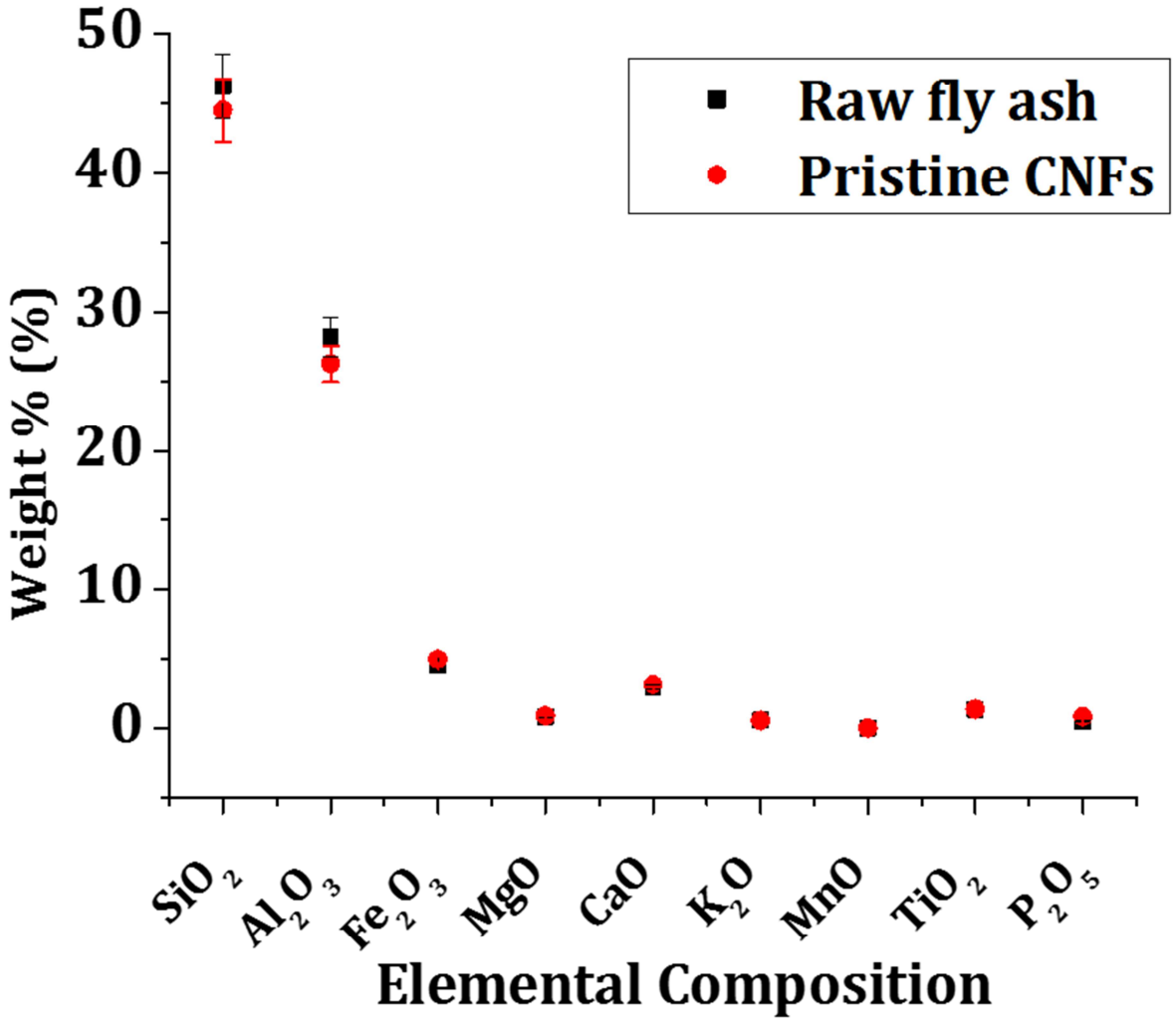

Figure 4.1.6: Graphical summary of the XRF data obtained for the pristine CNFs and raw fly ash.

The difference in composition of the raw fly ash and pristine CNFs was less than 5% as shown by the error bars. The differences lie within the instrumental error margin and thus made it difficult to pinpoint the element that was responsible for the formation of the CNFs from the raw fly ash. This result indicated that the formation of CNFs came

about as a consequence of a small amount of one or more of the fly ash's major elemental components.

In order to confirm the morphological and physical differences of the pristine CNFs and the raw fly ash, electron microscopy was performed on both.

TEM and SEM/EDS characterisation

SEM characterisation of the products showed the presence of a dense network of CNFs bound together by Van der Waals forces or due to entangling through growth **Fig 4.1.7**

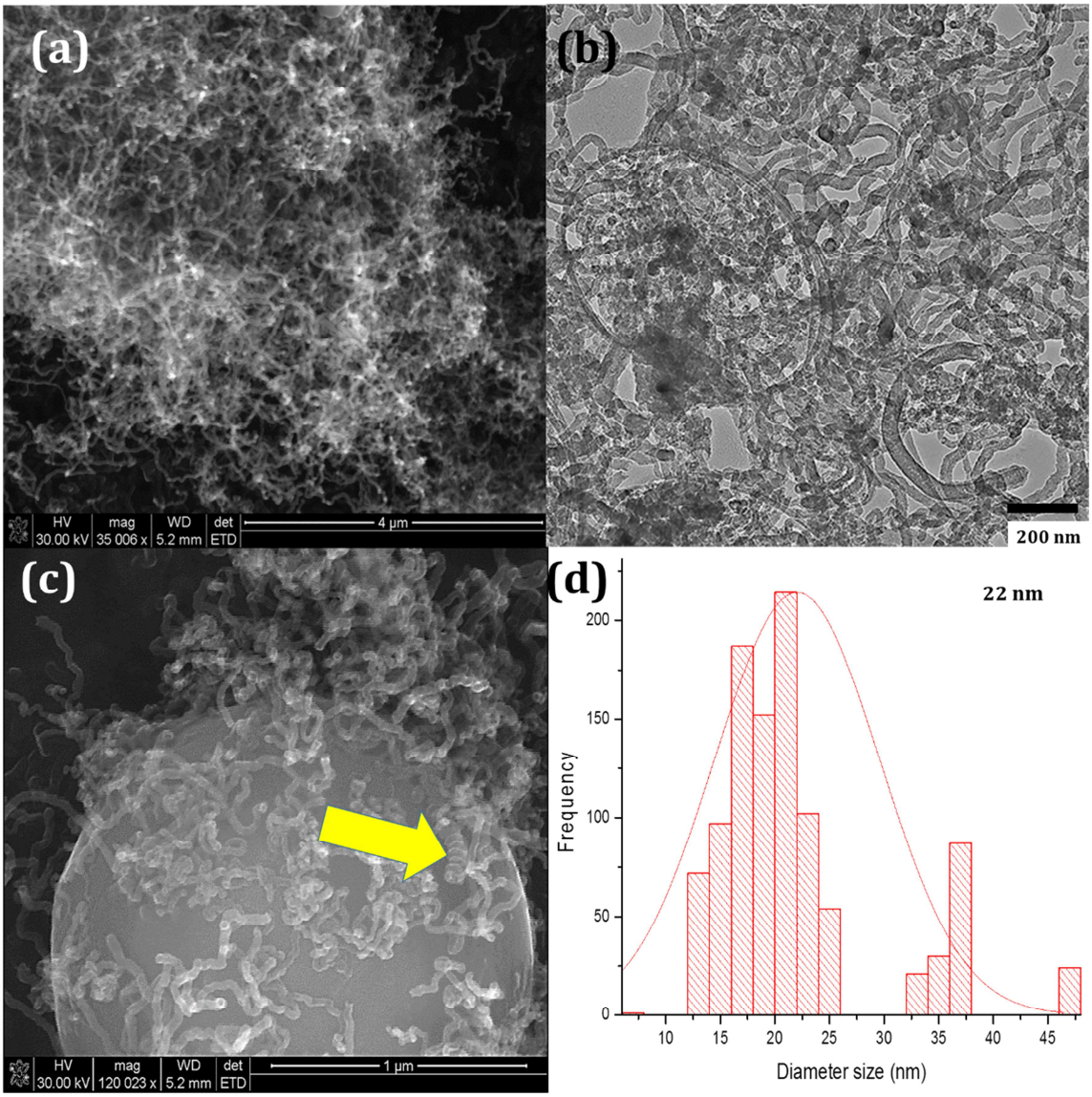

(a) [32].

Figure 4.1.7: (a) SEM and (b) TEM image of CNFs, (c) SEM image of CNFs on a raw fly ash (arrow pointing at spirals) and (d) the diameter size distribution plot of the CNFs.

TEM studies indicated that CNFs were successfully synthesised with various diameters, along with some amorphous carbonaceous materials (**Fig 4.1.7** (**b**)). Some of the CNFs synthesised were hollow. However, CNFs with diameters close to 47 nm or smaller were not found to be hollow. Surface analysis of the raw fly ash, at a magnification of x120k, indicated that the pristine CNFs may have been anchored on their surface and that some of the pristine CNFs were spiral in form (yellow arrow on **Fig 4.1.7** (**c**)). Even though these observations were made, the actual structural arrangement in the CNFs remained a matter of speculation.

The particle size distribution plot (**Fig 4.1.7** (**d**)) showed that the average diameter of the CNFs was 22.0±7 nm and the minimum and maximum diameters were 13.0 nm and 47.0 nm, respectively. This suggested that the catalyst nanoparticles responsible for the formation of the CNFs had roughly an average diameter of 22.0±7 nm, since the diameter of the pristine CNFs has been shown to depend highly on the diameter of the activated catalyst particle [33].

Although TEM confirmed that the CNFs had been successfully synthesised from raw fly ash, the initial observations did not provide an understanding of how this occurred. This was therefore the subject of the study which followed.

Growth mechanism study

The use of TEM characterisation to understand the growth mechanism of CNF formation

Using electron microscopy, the processes that took place in the CVD reactor were monitored in 10 min intervals after the first 15 min of exposure to C_2H_2 and H_2. Each reaction was repeated with new batches of raw fly ash over the reaction time, to make sure that the observations were reproducible.

TEM images taken from raw fly ash particles **Fig 4.1.8** (**a**) before exposure to C_2H_2 and H_2, revealed spherical along with angular particles [4]. A point analysis EDS of these particles was performed on the spot labelled (i) (**Fig 4.1.9**). This showed that the raw fly ash contained metals like: Sb, Fe, Cr, Mg, Os, Al and Si as either alloys, phosphates, sulphates or oxides.

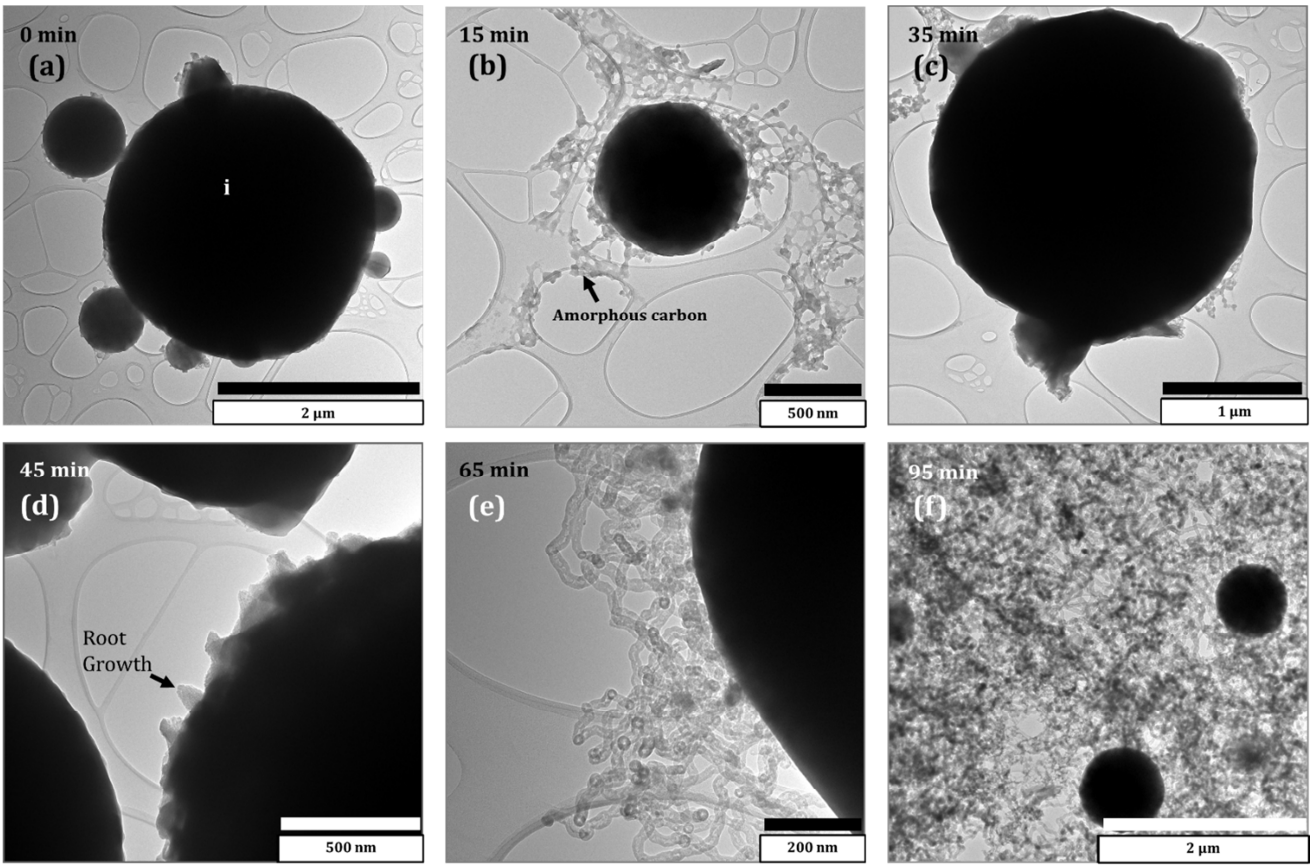

Figure 4.1.8: (a) Raw fly ash particles before any CVD treatment, (b) Amorphous carbon forming on the surface of raw fly ash particles after 15 min (150 °C) of exposure to C_2H_2 and H_2, (c) Initial growth of filamentous CNFs, after 35 min (350 °C) of exposure to C_2H_2 and H_2, (d) Root growth of CNFs from the fly ash particle after 45 min (450 °C) of exposure to C_2H_2 and H_2, (e) CNFs on the surface of fly ash particles after 65 min (650 °C) of exposure to C_2H_2 and H_2, (f) Two fly ash particles surrounded by a great number of CNFs after 95 min (held at 650 °C for 30 min) exposure to C_2H_2 and H_2.

Fig 4.1.8 (**b**) showed that the raw fly ash particles after exposure to C_2H_2 and H_2 at 150 °C (after 15 min) became surrounded by carbonaceous material.

At 350 °C i.e. after 35 min of exposure to C_2H_2 and H_2 (**Fig 4.1.8** (**c**)) the carbonaceous material formed at 150 °C became depleted. At 450 °C or after 45 min of exposure to C_2H_2 and H_2 (**Fig 4.1.8** (**d**)) root growth had begun to be initiated on the surface of the raw fly ash particles. After 65 min **Fig 4.1.8** (**e**) a low yield of CNFs rooted on the surfaces of fly ash particles was noted. 95 min into the total reaction time i.e. at 650 °C (**Fig 4.1.8** (**f**)) the lengths of these CNFs increased substantially.

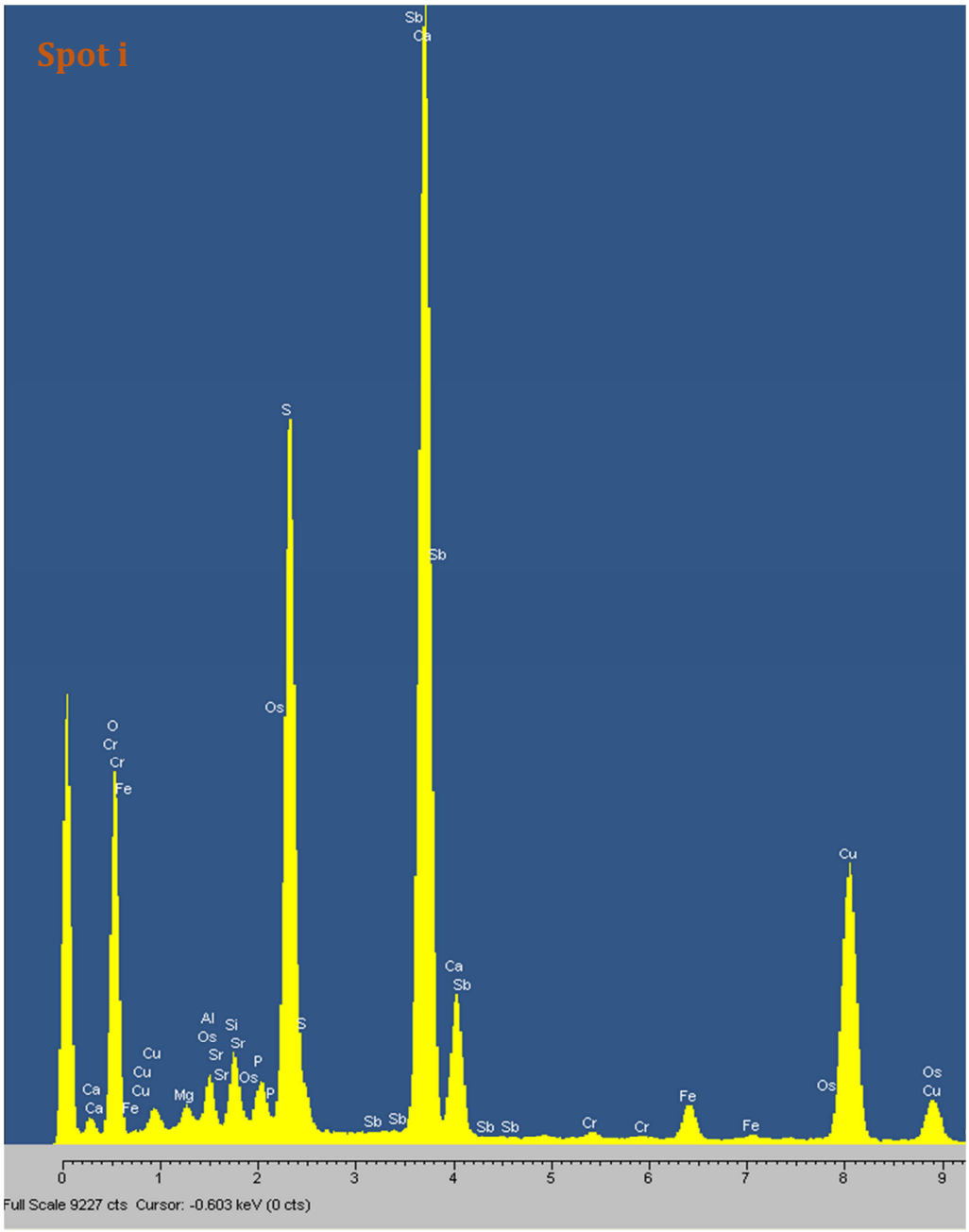

Figure 4.1.9: A typical EDS pattern obtained for raw spherical fly ash particle showing the presence of a cocktail of: Cr, Fe, Mg, Al, Si, Sr, Os, Sb and Os metals as well as P, O and S.

Raw fly ash was also found to be composed of irregular shaped metal oxide particle agglomerates (**Fig 4.1.10** (**a**)).

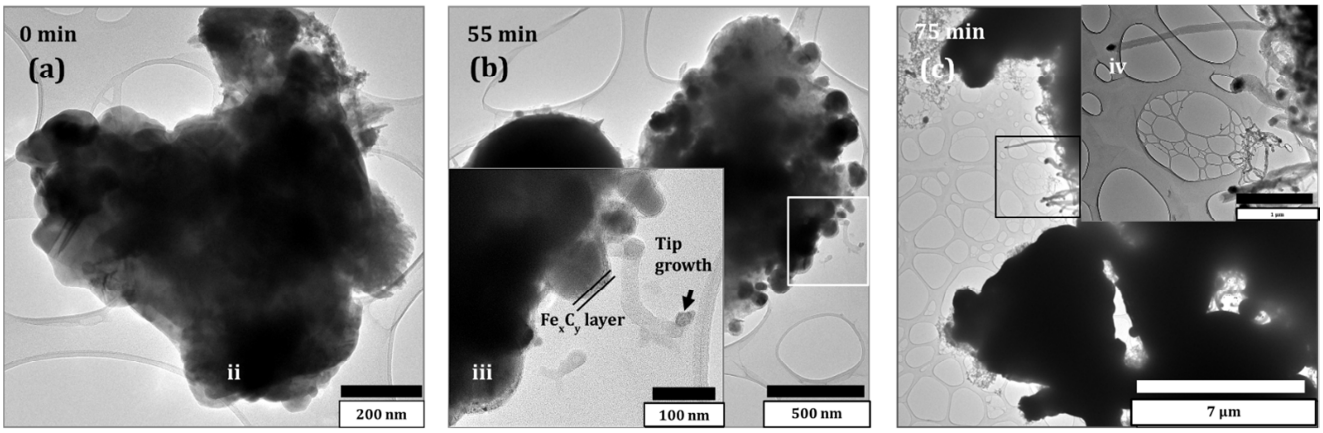

Figure 4.1.10: Representative TEM micrographs of unbound alloy particles and clusters at different times of the reaction: (a) Cluster of metal particles in raw fly ash, (b) Metal nanoparticles with a carbide/ carbon coating on the surface at 55 min (550 °C) of exposure to C_2H_2 and H_2 and an inset showing the initial stages of tip growth from a cluster, (c) Tip growth in an advanced stage with nanoparticles driving growth at 70 min (held at 650 °C for 10 min) of exposure to C_2H_2 and H_2.

EDS was performed on a representative (80%) agglomerate on the spot labelled (ii) and the pattern as shown in **Fig 4.1.11**. This figure suggested that it contained the same metals as the spherically shaped raw fly ash particles with an addition of: C, Ti, Ge, Sn and the exclusion of S, Sb and Os, in their alloy, phosphate, and oxide or carbide states.

Here, unlike before, after 55 min of exposure to C_2H_2 and H_2 at 550 °C (**Fig 4.1.10** (**b**)) the irregular shaped metal particle aggregates became carburised, and appeared to dust into smaller pieces which were further coated with carbon layers. At this stage it was evident that tip growth was initiated, as seen in the inset.

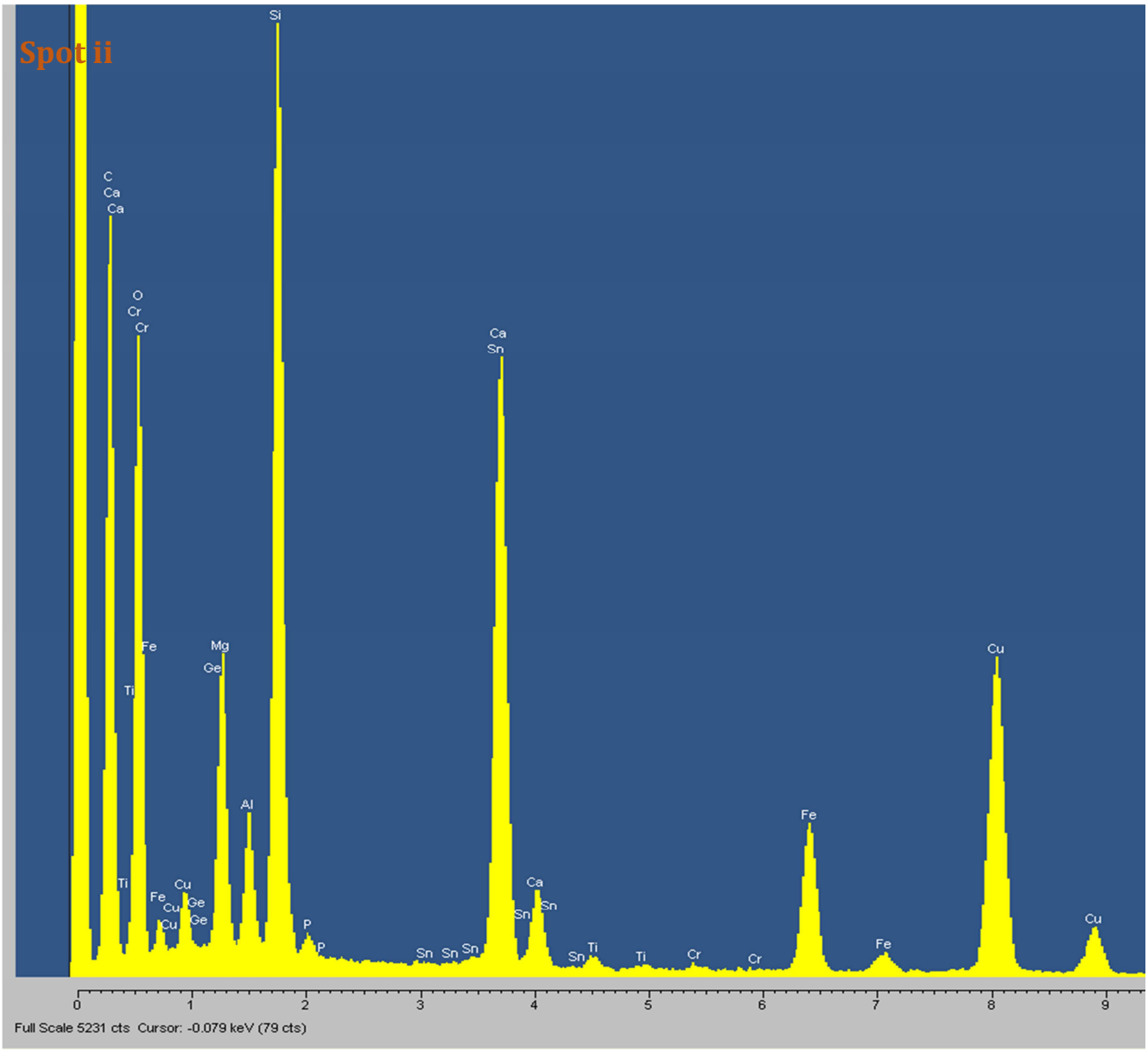

Figure 4.1.11: An EDS pattern obtained from the irregular shaped metal particle agglomerate found in a raw fly ash showing the presence of: Ge, Cr, Fe, Mg, Al, Si, Sn, Ti, Sb and Os metals and P and O.

An EDS pattern **Fig 4.1.12** was obtained for the spot labelled (iii) on **Fig 4.1.10** (**b**) and it suggested that the particle contained: Fe, Ca and some Si. This may have alluded that Fe and Ca were the active agents for the formation of the CNFs. XRF showed the presence of haematite, and in agreement with it, EDS data suggested that the main metal oxide responsible for the formation of the CNFs was an iron oxide, possibly haematite.

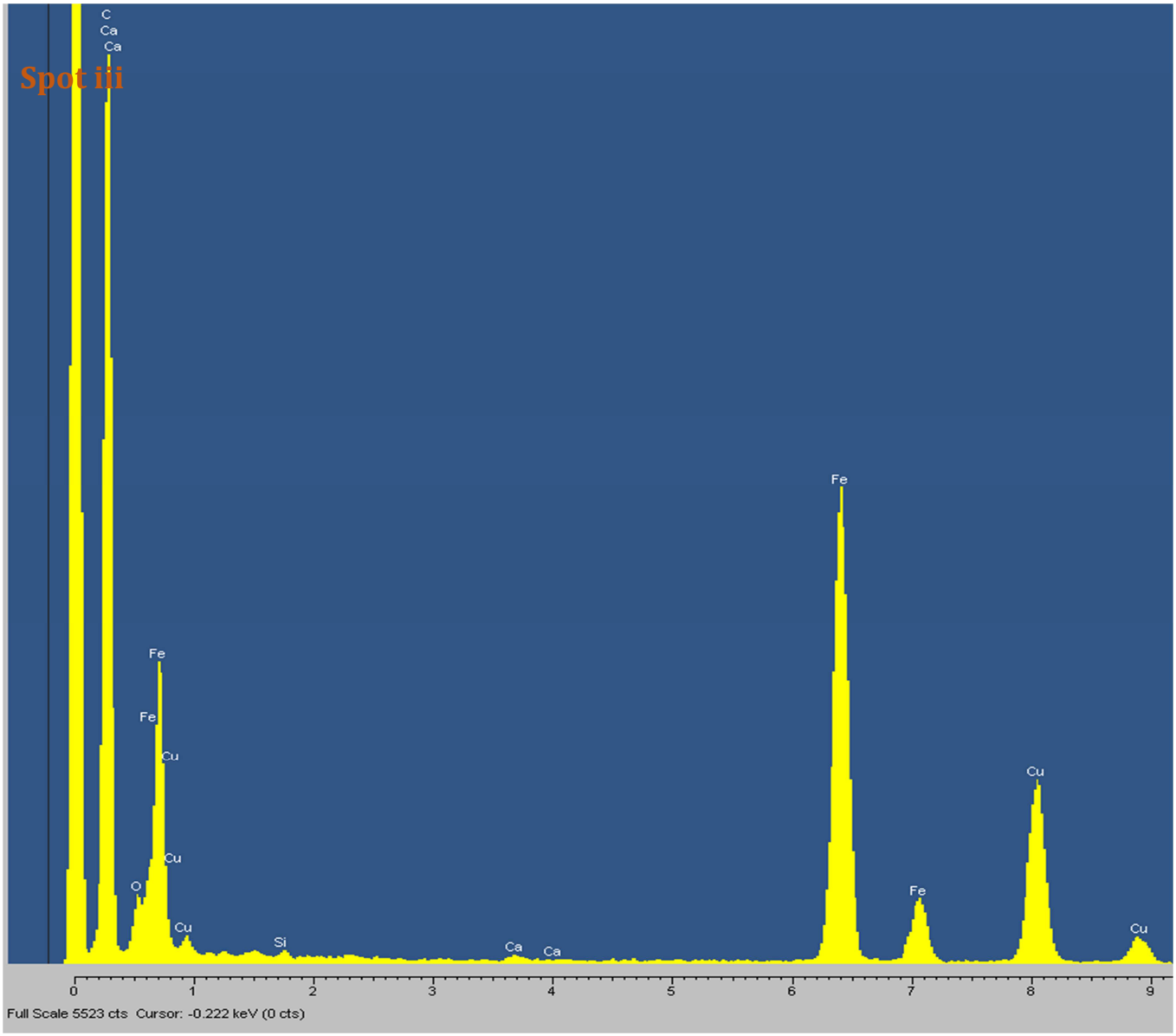

Figure 4.1.12: An EDS pattern of a carburised Fe-rich particle coated with a carbon layer, showing the presence of: Fe, Ca and Si with O.

After 75 min of exposure to C_2H_2 and H_2, it was observed that some metal aggregates (**Fig 4.1.10** (**c**)) showed tip growth in an advanced stage, because it was noted that the CNFs had become longer and increased in number from 55 min to 75 min.

This observation implied that carburisation of these aggregates continued as the reaction proceeded. Another EDS pattern was obtained (**Fig 4.1.13**) for the spot labelled (iv) on the insert in **Fig 4.1.10** (**c**) and this once again confirmed the initial observations that the particles that were found on the tips of the pristine CNFs were Fe-

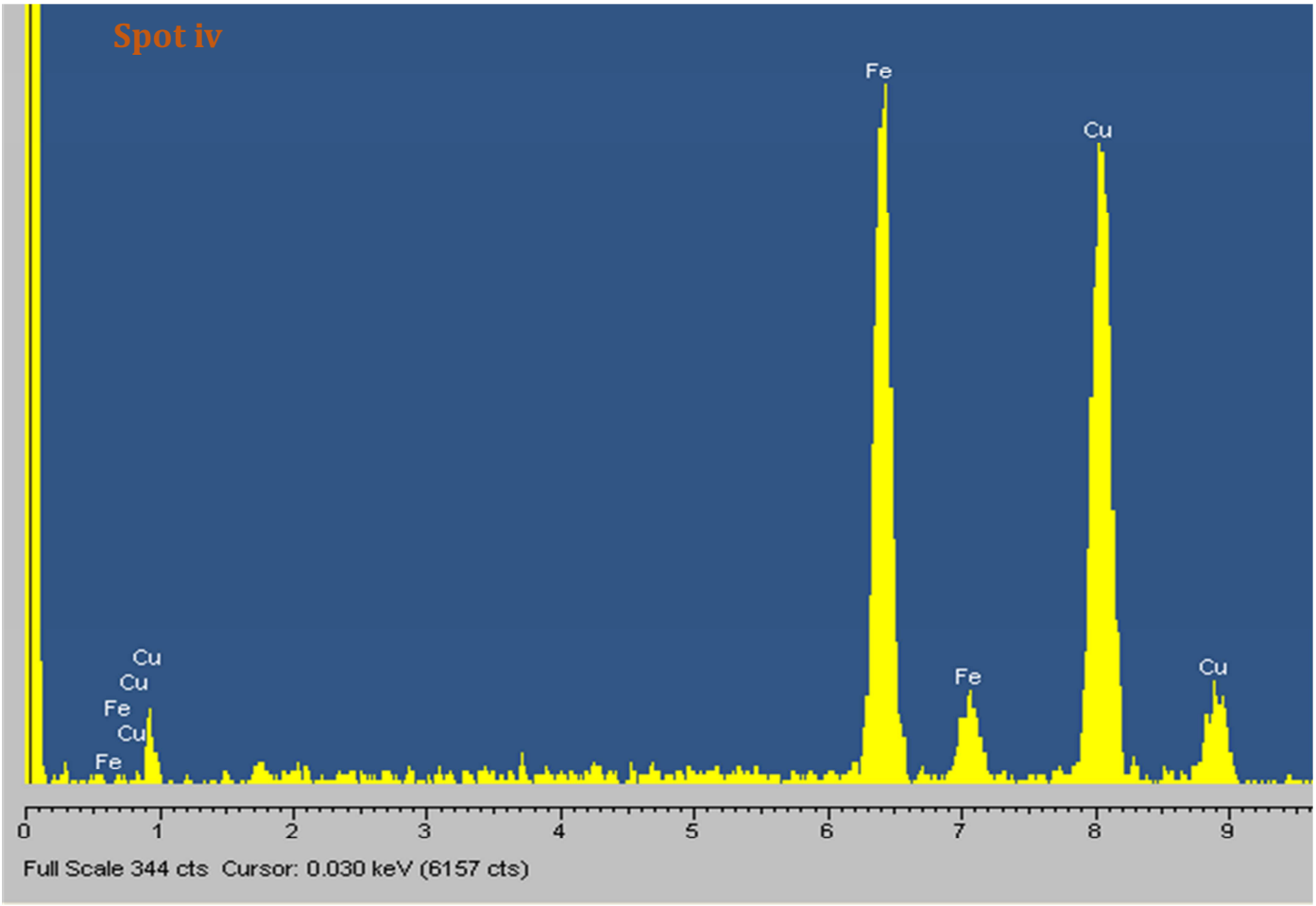

Figure 4.1.13: An EDS pattern obtained from the metal particle at the tip of a CNF which was Fe-rich.

The use of laser Raman spectroscopy to understand the growth mechanism of CNF formation

Dispersive laser Raman was performed on the raw fly ash and the samples of fly ash that were exposed to C_2H_2 and H_2 for different times. The first reaction was run for 15 min, cooled to room temperature under hydrogen gas flow, and then the samples were collected for characterisation. Every new reaction after that was run in increments of 10 min following the same procedure as above. The Raman spectra were obtained on the centre area (30 µm x 30 µm) of the given reflected light images (**Fig 4.1.14** (**a**)).

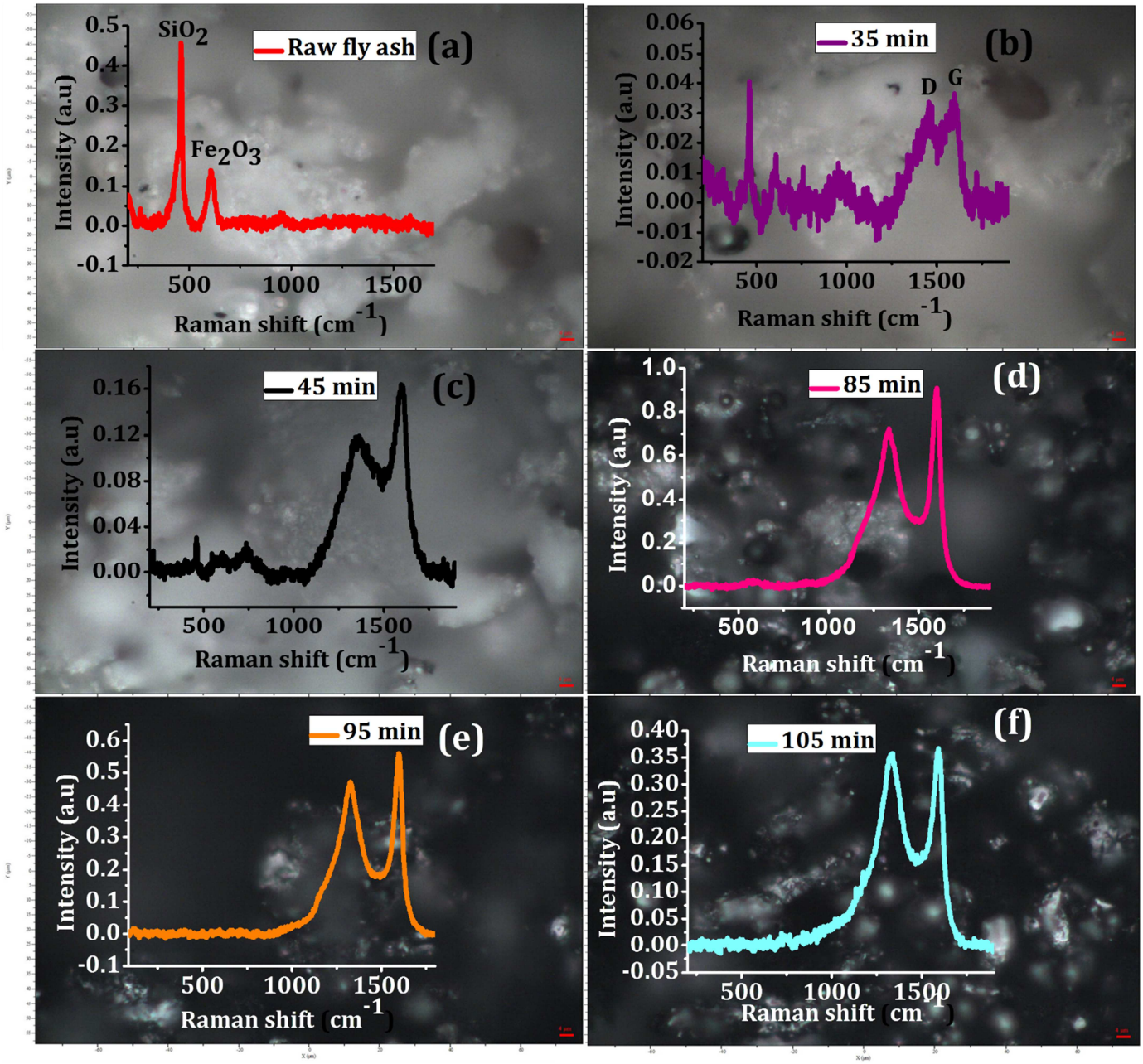

Figure 4.1.14: Raman spectra of the raw fly ash after different exposure times to C_2H_2 and H_2 superimposed over their reflected light images: (a) Raw fly ash. Fly ash particles at exposure of (b) 35 min, (c) 45 min, (d) 85 min, (e) 95 min and (f) 105 min.

At 0 min of exposure to C_2H_2 and H_2 the raw fly ash showed the presence of α-SiO_2 vibrational modes at 463 cm^{-1}, which corresponded to the A_1 vibration. Another band was also observed at 613 cm^{-1} which corresponded to the O- displacements occurring in haematite [34].

After 35 min of exposure to C_2H_2 and H_2 the typical D (1415 cm^{-1}) and G (1599 cm^{-1}) vibrational modes of carbon emerged and the silica and haematite modes disappeared

(**Fig 4.1.14** (**b**)). This indicated that the CNF layer that coated the fly ash particles was becoming thicker. After 45 min of exposure to C_2H_2 and H_2 the carbon peaks continued to become more prominent, while the rest of the peaks began to disappear (**Fig 4.1.14** (**c**)).

From 85 min to 105 min (**Fig 4.1.14** (**c-e**)) the carbonaceous material thoroughly covered the fly ash particles and suppressed the silica and haematite peaks completely. From the laser Raman and TEM studies a total reaction scheme for the formation of CNFs from CFA as a catalyst was proposed (**Fig 4.1.15**).

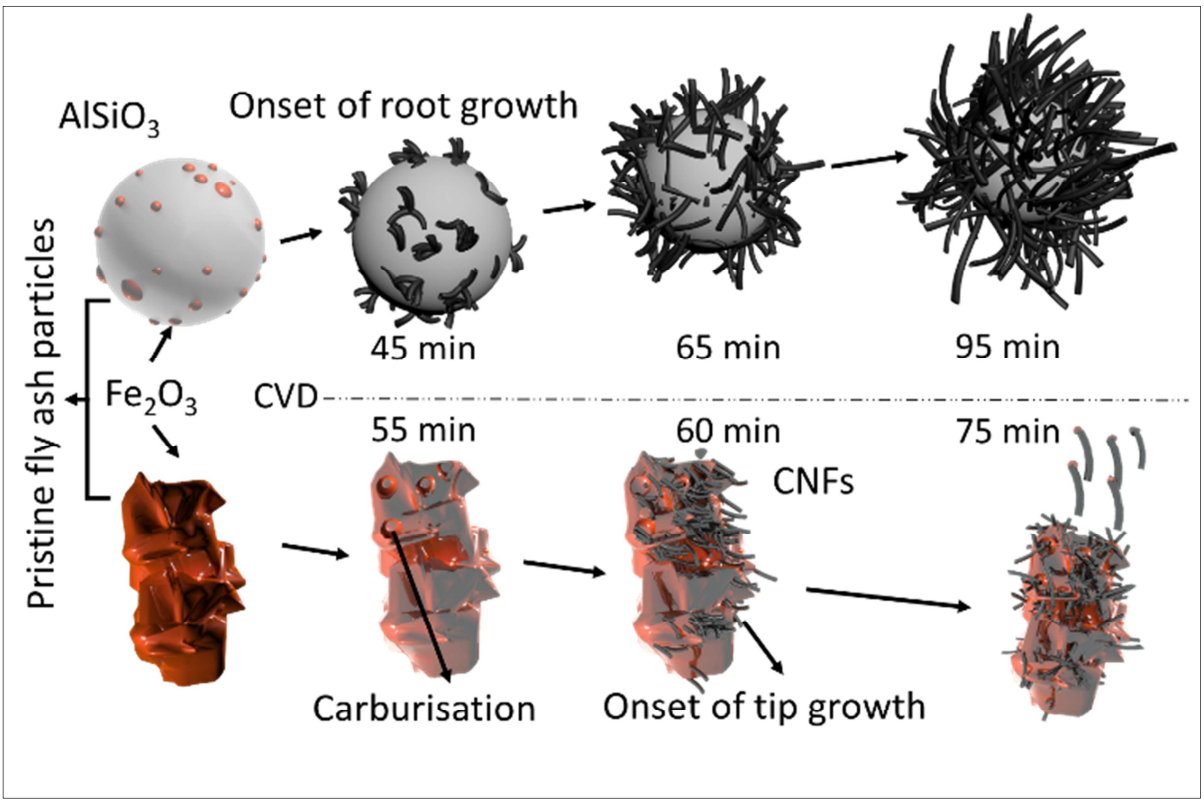

Figure 4.1.15: A proposed reaction scheme for the growth of CNFs from CFA particles over the reaction time.

Conclusions

Raw fly ash could be used for the CVD synthesis of CNFs at 650 °C under reaction of C_2H_2 and H_2. Here the fly ash changed from grey to black when CNFs were formed. This was confirmed through the use of: PXRD, BET, XRF, ATR-FTIR, TGA, TEM and SEM. PXRD showed that all the phases that were found in raw fly ash were also found in the CNFs, the difference being the high intensity of carbon peak for the CNFs. It also confirmed the presence of haematite in the raw fly ash. BET showed that the surface

area of 0.04 m^2/g of the starting material (raw fly ash) increased substantially to 20.00 m^2/g when it was reacted with C_2H_2 and H_2 to form CNFs. This meant that the presence of CNFs increased the surface area of the overall mixture. Laser Raman spectroscopy suggested that both raw fly ash and fly ash reacted with C_2H_2 and H_2 contained carbonaceous materials; but the high intensity of the D and G shifts for the fly ash reacted with C_2H_2 and H_2 suggested a greater amount of carbonaceous material had formed. A similar conclusion was derived from ATR-FTIR data which showed that both the raw fly ash and the fly ash reacted with C_2H_2 and H_2 had the same bonds present, with the former having more intense peaks. TGA confirmed the presence of a new dominant phase after the exposure of fly ash to C_2H_2 and H_2 at higher temperatures. This dominant phase (CNFs) formed roughly 75% of the total mass of the mixture.

XRF showed that all the phases that were present in the raw fly ash were also present in the pristine CNFs. The differences in the amounts of the components between raw fly ash and pristine CNFs were found to be less than 5%. This value corresponded to the standard deviation error obtained when analysing a USGS certified standard, which made it difficult to determine if any of the elements present in the raw fly ash had been responsible for the formation of the CNFs. However, it showed that whatever it was, it was barely consumed during the reaction. Electron microscopy fully confirmed the formation of the tubular CNFs from the raw fly ash. The particle size obtained using the micrographs revealed that the pristine CNFs had an average diameter of 22.0±7 nm.

The growth mechanism of the raw fly ash from the CNFs was monitored using electron microscopy with EDS and laser Raman spectroscopy. A systematic examination of the TEM micrographs, monitoring the growth of the CNFs on the surface of the fly ash showed that the observations made there were in agreement with those made with laser Raman spectroscopy.

Laser Raman spectroscopy suggested that before exposure of the fly ash to C_2H_2 and H_2, the only prominent peaks were those of silica and haematite. After subsequent exposure these peaks disappeared and the emergence of the D and G bands characteristic of carbon- carbon vibrations began and continued to intensify until the completion of the reaction. Laser Raman spectroscopy showed that carbonaceous materials started forming at 350 °C.

Based upon these observations, the proposed growth mechanism for CNFs from fly ash particles could be broken into two general types: (i) root and (ii) tip growth. The root growth mechanism was predominantly apparent on the spherical raw fly ash particles (80% m/m) and the tip growth route was predominant on the irregular shaped agglomerates of metal particles that were Fe-rich. From EDS observations it could be conclusively said that the particles responsible for the growth of the pristine CNFs were Fe-rich [19].

4.2 Chemical functionalisation of the carbon nanofibres

Carbon nanofibres are chemically inert and agglomerate [35], [36] in aqueous environments [37]. This is a challenge when the intention is to treat them chemically in such environments. Many researchers have sought to bind CNFs chemically with other metal oxide nanoparticles, because of possible synergistic enhancements of properties that the CNFs and metal oxide nanoparticles may have with each other. Hydrothermal methods have been highly studied for synthesising metal oxide nanoparticles and if the CNFs were not going to be treated to interact with metal oxides in an aqueous medium it would be difficult to disperse them [38]. Some researchers have developed techniques to enable the dispersion and chemical versatility of CNFs in different media. They have managed to functionalise the CNF framework physically and chemically to achieve both dispersion and chemical reactivity [32], [39], [40].

Physical functionalisation techniques lead to a non-destructive process of binding CNFs with other moieties; thus their chemical, electronic and physical properties do not change [32], [41]. There are generally three types of physical functionalisation: polymer functionalisation (van der Waals and π-π stacking interactions), surfactant functionalisation (hydrophobic attractions) and endohedral functionalisation (storage of guest molecules into the inner cavity of the CNFs provided that they are the hollow-type). Physical functionalisation methods cost less, are non-invasive and the fibres remain intact. CNFs functionalised this way are good, but there is a concern when synthesising these for load-bearing nanocomposites because the interaction of the CNFs and the matrix would be facilitated by weak bonds [41].

Strong covalent bonds between metal oxide particles and the CNFs prevent their easy removal, while allowing for electron transfer to take place [42]. Chemical functionalisation is therefore the best route to forming chemical bonds between the frameworks of CNFs and metal oxide particles. CNFs can be functionalised on their termini or their walls through a variety of methods. Methods such as: fluorination [43], halogenation, chemical treatments such as Diels-Alder [44], hydrogenation [45] and azomethine ylide reactions have been successfully used for the functionalisation of CNFs [40]. The most conventional way to functionalise CNFs is by treating them with concentrated acids or their mixtures.

CNTs/CNFs are often treated with acids like concentrated nitric [46] and/or sulphuric acid [47] to introduce carboxylic, hydroxyl, quinones, lactones, phenol, carbonyl, nitro, hydroxyl and sulphonic groups on the surface [48].

This type of functionalisation of CNFs thrives because of the presence of defects on the surface of the CNFs as these serve as anchors for the attachment of other functional groups [49], [50]. For instance, five or seven membered rings in the C framework result in bending the fibre/tube, while the presence of sp^3 hybridised C centres with (OH and H) attached to the surface allow for more functionalisable areas on the CNFs. Likewise, the presence of carboxylic groups (the same type that occurs when CNFs are functionalised with a HNO_3:H_2SO_4 mixture) that result from oxidative destruction, also allows for better functionalisation [50].

CNFs made from South African fly ash were systematically treated with concentrated HNO_3:H_2SO_4 mixtures for different times. This was done to assess the effect of the duration of functionalisation on the structure and chemical behaviour of the CNFs. The intention was to bind titania (anatase) nanoparticles onto the surface of these CNFs, with the aim of using the resulting CNF-TiO_2 hybrid as a catalyst for photosensitive reactions or as a potential supports for catalysts in other reactions. Literature suggests that CNFs have the potential to lower the bandgap of anatase because they can act as a sink for the electrons that are photogenerated and delay the e^+/h^- pair recombination. In this regard, the Ti-O-C bond is suspected to facilitate the channelling of electrons from anatase to the CNFs and back [51]-[55].

Although, Yasui *et al.* have suggested the possibility of using their materials for optical applications [16], so far none of the workers in this research area have actually beneficiated their fly ash derived carbonaceous materials for direct application. Hence, using waste fly ash (an abundant waste material) to make TiO_2 decorated CNF hybrids in this way is highly desirable and makes this process potentially feasible for commercial use, if successful.

Experimental and characterisation

The functionalisation of pristine CNFs

A fixed amount of pristine CNFs (4 g) was placed in a round bottom (RB) flask equipped with a stirrer bar. A total of 60 ml of a HNO_3: H_2SO_4 (3:1 v/v) mixture was added into the RB flask while stirring. The (67%) HNO_3 (obtained from ACE) and (98%) H_2SO_4 (purchased from Merck-Millipore) were used. The pristine CNFs were functionalised for 2, 6 and 12 h at 110 °C, then the products were diluted with deionised water to a pH of 3 before suction filtering and rinsing to a pH of 6. The functionalised CNFs (fCNFs) were then oven dried at 100°C for 8-12 hours and then characterised.

Characterisation of the fCNFs

For the morphology, a possible surface roughening indicator, and manual particle size determination the FEI Tecnai T12 TEM (working at 120 kV) was used.

The Horiba, Jobin-Yvon LabRAM Raman and the Bruker Senterra Dispersive Micro-Raman spectrometers, equipped with the 514.5 nm and 532 nm lines respectively, were used to determine the laser Raman spectra. Laser Raman spectroscopy provided information on the graphitic nature of these materials and showed the effects of prolonged acid functionalisation on the surface of the fCNFs.

Attenuated total reflection-Fourier transform infrared (ATR-FTIR) spectra were obtained for the pristine CNFs using the Bruker Tensor 27 with a ZnSe window (500 – 6000 cm^{-1}). ATR-FTIR helped establish the presence of carboxylic moieties and other bonds which confirmed the functionalisation of the CNFs as well as qualitatively indicated the extent of functionalisation of these with time.

Thermogravimetric analysis was performed on the fCNFs to determine the amount of ash that remained in the product after functionalisation. This analysis was performed using a Perkin-Elmer Simultaneous Thermal Analyser (STA 6000).

Surface area analyses were performed on the fCNFs to compare them with each other as well as to see the effect of the functionalisation time on their surface areas. The surface area analysis were performed using a Micromeritics Tristar 3000 Brunauer-Emmett-Teller surface area analyser.

The phases of the minerals and elements present in the raw fly ash and CNFs were determined using powder X-ray diffraction. The diffractometer used was the Bruker D2 PHASER with a LYNXEYE detector. It had a Co K_{α} source at 30 kV. This was performed to assess if any phases were leached out of the fly ash after prolonged acid functionalisation.

X-ray fluorescence (XRF) elemental data was obtained using a Bruker S2 Ranger. This technique was used to characterise the fCNFs. As before with PXRD the concentration of elements in the raw fly ash, incorporated into the CNFs, and their variation with functionalisation were monitored using this technique.

Results and discussion

TEM characterisation

The TEM micrographs shown in **Figs 4.2.1 a-c** reveal the effect of functionalisation time on the surface of the CNFs. Here it could be seen that the fCNFs began with a smooth surface (**Fig 4.2.1** (**a**)) and as time proceeded the surface roughness increased (**Fig 4.2.1** (**a**))

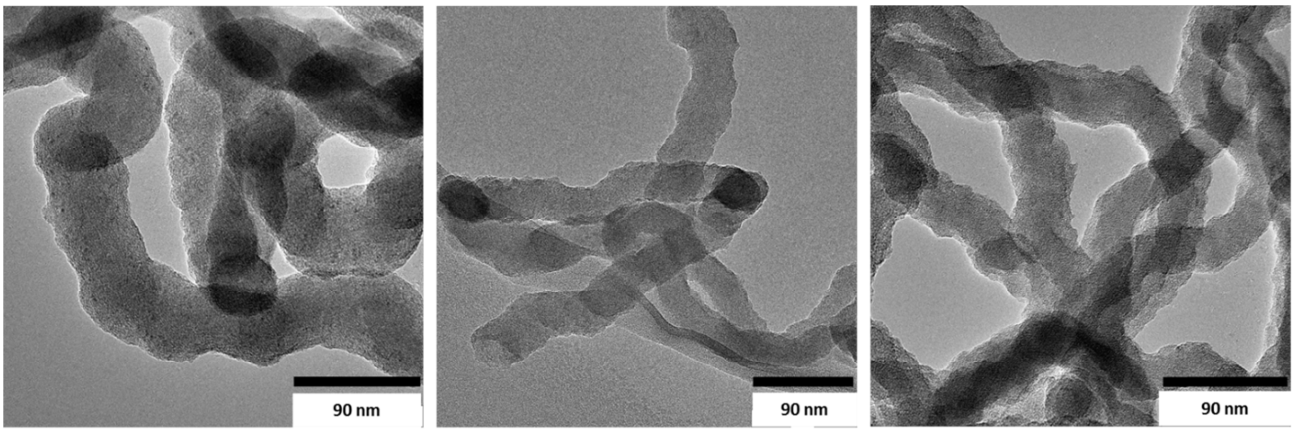

Figure 4.2.1: (a) TEM images of 2 h fCNFs, (b) 6 h fCNFs and (c) 12 h fCNFs showing increasing surface roughening progression.

Laser Raman spectroscopy characterisation

The laser Raman spectra obtained for the CNFs and the fCNFs functionalised at 2, 6 and 12 h as shown in **Fig 4.2.2** (**a**). As before the characteristic D (~ 1350 cm^{-1}) and G (~ 1624 cm^{-1}) bands of carbon were evident on the CNFs and fCNFs.

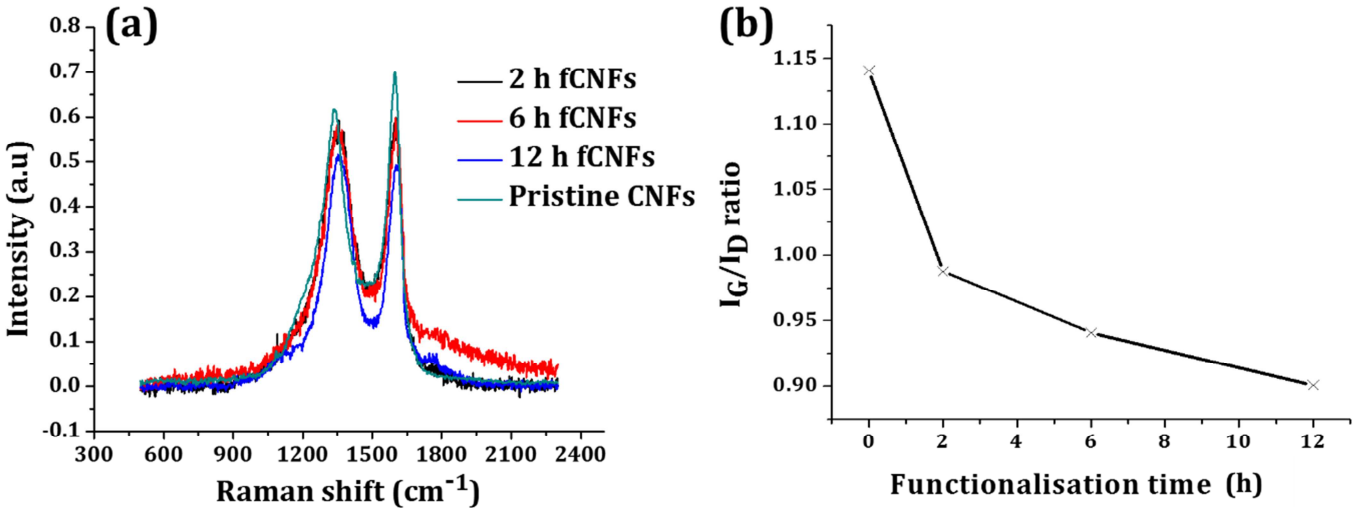

Figure 4.2.2: Laser Raman spectra of (a) CNFs (turquoise), 2 h fCNFs (black), 6 h fCNFs (red) and 12 h fCNFs (blue) and (b) the corresponding plot of the I_G/I_D ratio as a function of the duration of functionalisation.

A plot of the I_G/I_D ratio vs the functionalisation time (**Fig 4.2.2** (**b**)) revealed that this ratio decreased with increasing functionalisation time. This suggested that the CNFs ended up with more surface defects because of functionalisation. This observation is in agreement with what is found generally in literature [56]. However, in some rare cases this ratio has been known to have increased under such conditions due to the high removal of defects and/ or amorphous carbon on the CNFs [48].

A systematic drop of the I_G/I_D ratio as a function of the duration of functionalisation from 1.14 for pristine CNFs to 0.90 for 12 h fCNFs was observed. This functionalisation in the acid mixture resulted in the surface of the CNFs being rougher. However, the final goal was to introduce functional groups and defects on their surfaces to enable bonding between CNFs and TiO_2 nanoparticles. The functional groups on the surface of the CNFs were then studied using ATR-FTIR.

ATR-FTIR spectroscopy characterisation

ATR-FTIR studies of the surfaces of carbon nanotubes treated under similar conditions revealed that these CNFs might have been expected to have had: carbonyls, carboxylics, quinones, hydroxyls, lactones and even the sulphonic functional groups [48]. However, most researchers have reported the presence of carboxylic (OHC=O) functional groups only. In this study the presence of the carbonyl (C=O) groups were observed on the functionalised CNFs (**Fig 4.2.3**).

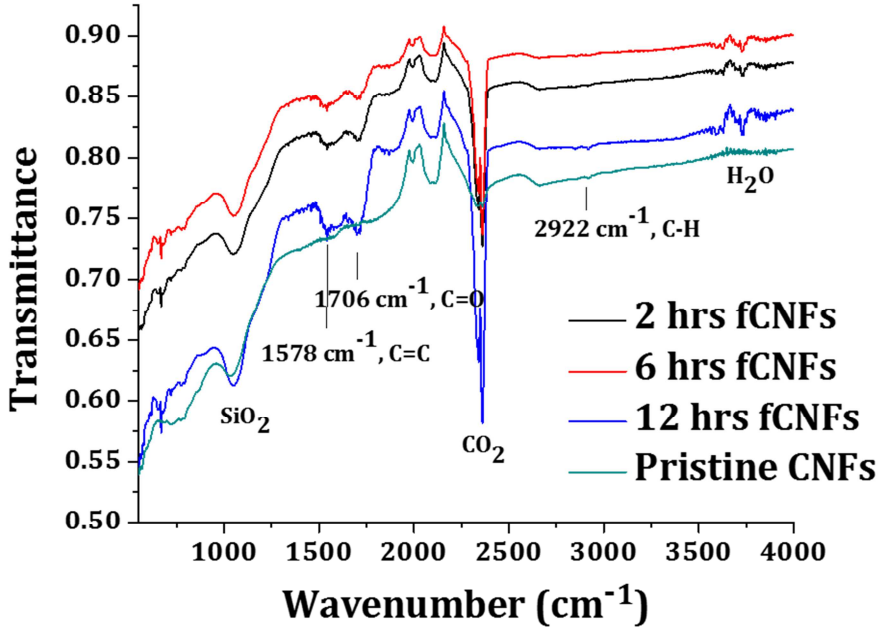

Figure 4.2.3: ATR-FTIR spectra of CNFs (turquoise), 2h fCNFs (black), 6 h fCNFs (red) and 12 h fCNFs (blue).

This was observed through the presence of the band at 1706 cm^{-1}, due to the C=O stretch, and the absence of the –OH stretch at about 3400- 3500 cm^{-1} [57]. It must be noted that the absence of the –OH stretch does not rule out the possibility of the C=O being an acid or any of the other carbonyl compounds.

The bands indicating the framework of the CNFs (C=C, 1578 cm^{-1}) was not intense before acid treatment but afterwards it was. This observation in conjunction with laser Raman spectroscopy suggested that some amorphous carbon had been removed from the pristine CNFs compared to the acid treated ones. Other bands as seen in **Fig 4.2.3** indicated the presence of adsorbed atmospheric CO_2 (2357 cm^{-1}) and H_2O (3750 cm^{-1}). In the case of the latter band (i.e. H_2O), it appeared to increase as the functionalisation time increased. This suggested that the fCNFs had become more hydrophilic. Silica was present in all samples which indicated that the acid treatment did not appear to have removed much, if any of it.

Since it was not clear if any of the silica or any of the other major oxide phases in fly ash had been removed by the acid treatment, the pristine and functionalised samples were then studied by PXRD.

PXRD characterisation

The PXRD patterns of raw fly ash, pristine CNFs and 2, 6, 12 h fCNFs are shown in **Fig 4.2.4**.

Results from PXRD confirmed those that were obtained from the preceding characterisation techniques. Here it was again noted that not only was silica present in the fCNFs, but also the other major oxides such as mullite and haematite were too. Haematite peaks were observed at 2θs of: 28.10, 38.69, 41.6, 78.50 and 82.90° [26]. Carbon peaks were also observed at a 2θ angle of about 27° [27].

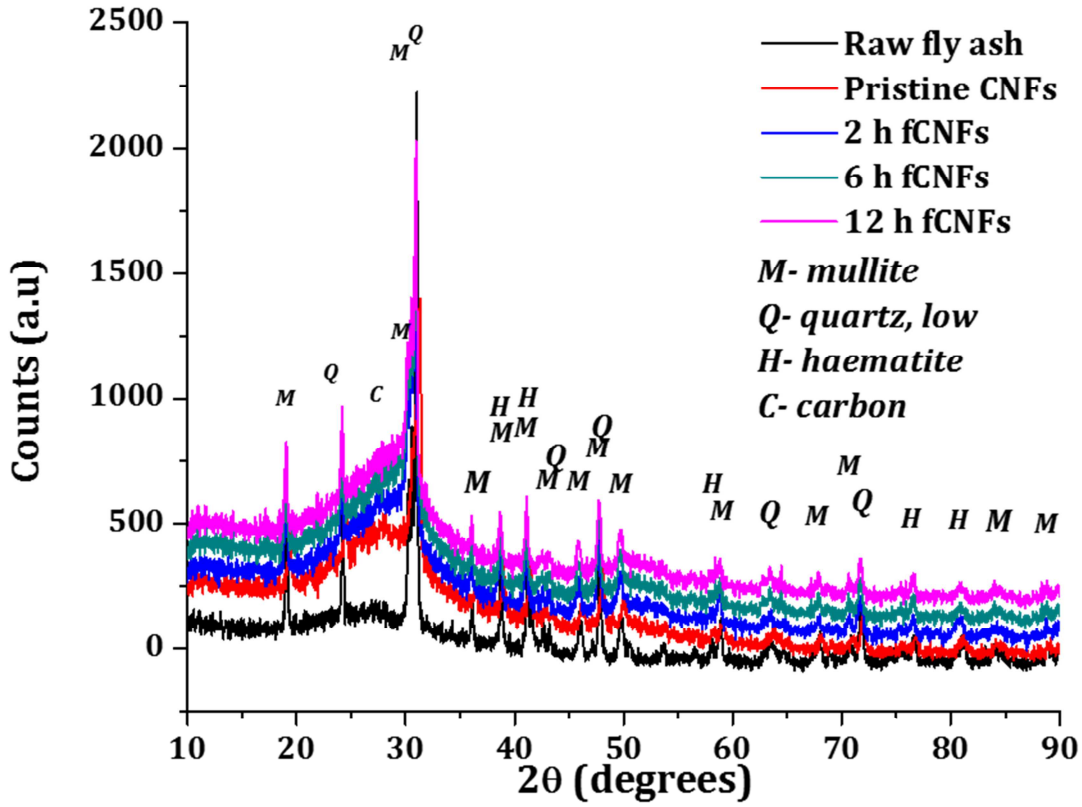

Figure 4.2.4: PXRD patterns of raw fly ash (black), pristine CNFs (red) and 2 h fCNFs (blue), 6 h fCNFs (turquoise) and 12 h fCNFs (pink).

This in conjunction with the ATR-FTIR data confirmed the observation that fly ash was still present in the products and that functionalisation had no significant effect on the major XRD detectable phases therein. These observations were in agreement with what Yasui *et al.* found when they had made MWCNTs from fly ash using CVD [16].

XRF spectroscopy characterisation

XRF characterisation was performed to monitor the effects of acid treatment on the possible leaching of the metal oxides. **Fig 4.2.5(a)** shows the major elemental composition of pristine CNFs and fCNFs which were functionalised at: 2, 6, and 12 h. Here, the presence of the oxides of: Si, Al, Fe, Ca, K, Mn, Mg, Ti and P were observed. After functionalisation only Fe_2O_3, P_2O_5 and CaO seemed to have varied notably in **Fig 4.2.5(b)** and they were leached out with higher functionalisation times.

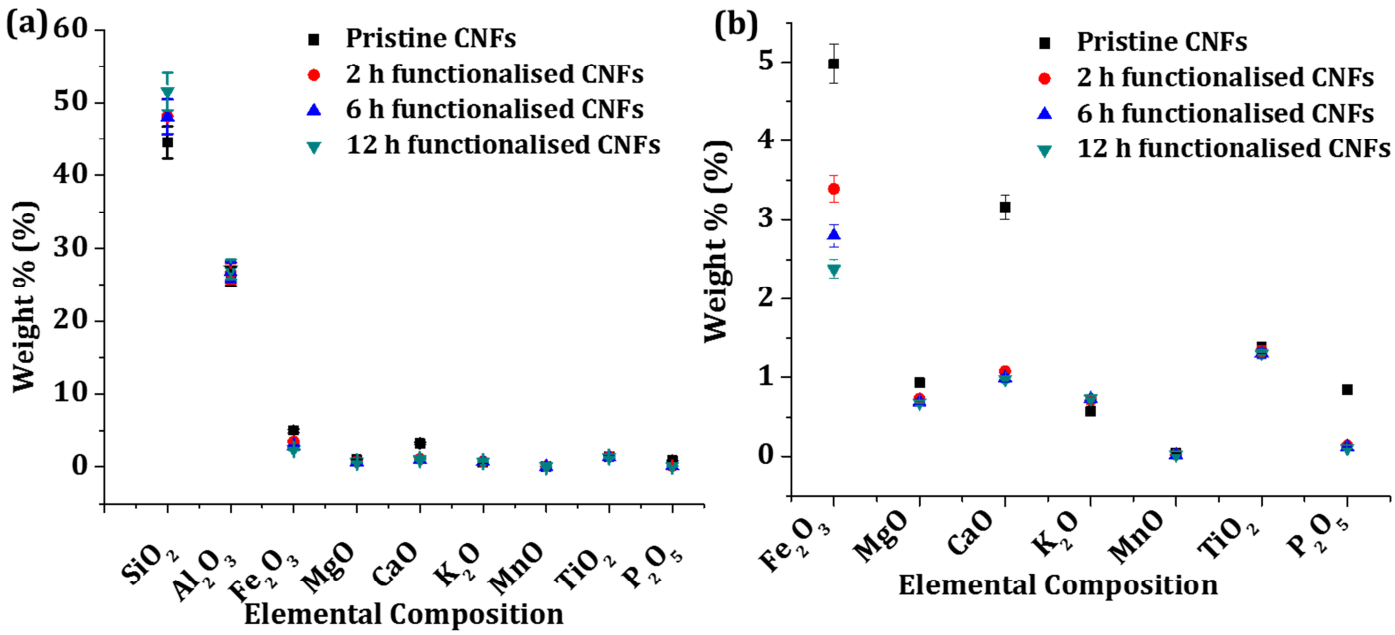

Figure 4.2.5: A XRF plot of the major metal oxides found in raw fly ash, pristine CNFs and 2 h fCNFs, 6 h fCNFs and 12 h fCNFs.

This observation was in agreement with that of Shivpuri *et al.* [58]. These authors realised that Fe was more tightly bound to fly ash particles than Ca, thus it was harder to leach out. It was also in agreement with the PXRD results because it showed that the oxides of: Si, Al and Fe remained dominant even after functionalisation.

It should be noted that the standard deviation (indicated by the added error bars on the measurement points) of all the measurements was less than 5%. This was confirmed by a repeat analysis of the standard USGS Andesite GV-2 sample. These observations provisionally corroborate what other authors discovered.

In the previous chapter it was seen that the surface area of fly ash was low as compared to the mixture of the CNFs and fly ash. In this study the focus was to determine the effect of functionalisation on the surface area of the fCNFs using N_2 adsorption BET surface area analysis.

BET characterisation

Isotherm plots were obtained during N_2 adsorption measurements for CNFs and fCNFs, functionalised at 2, 6 and 12 h **Fig 4.2.6** (**a-d**). According to IUPAC these represented type IV isotherms [28]. The formation of hysteresis loops at relative pressures above 0.4 indicated that the multilayer adsorption process characteristic of mesoporous

materials, had occurred for fCNFs and CNFs [29]. According to these BET results CNFs (**Fig 4.2.6** (**a**)) had a surface area of 20.00 m^2/g and fCNFs functionalised at 2 h (**Fig 4.2.6** (**b**)), 6 h (**Fig 4.2.6** (**c**)) and 12 h (**Fig 4.2.6** (**d**)) had 23.00 m^2/g, 16.00 m^2/g and 15.00 m^2/g surface areas, respectively.

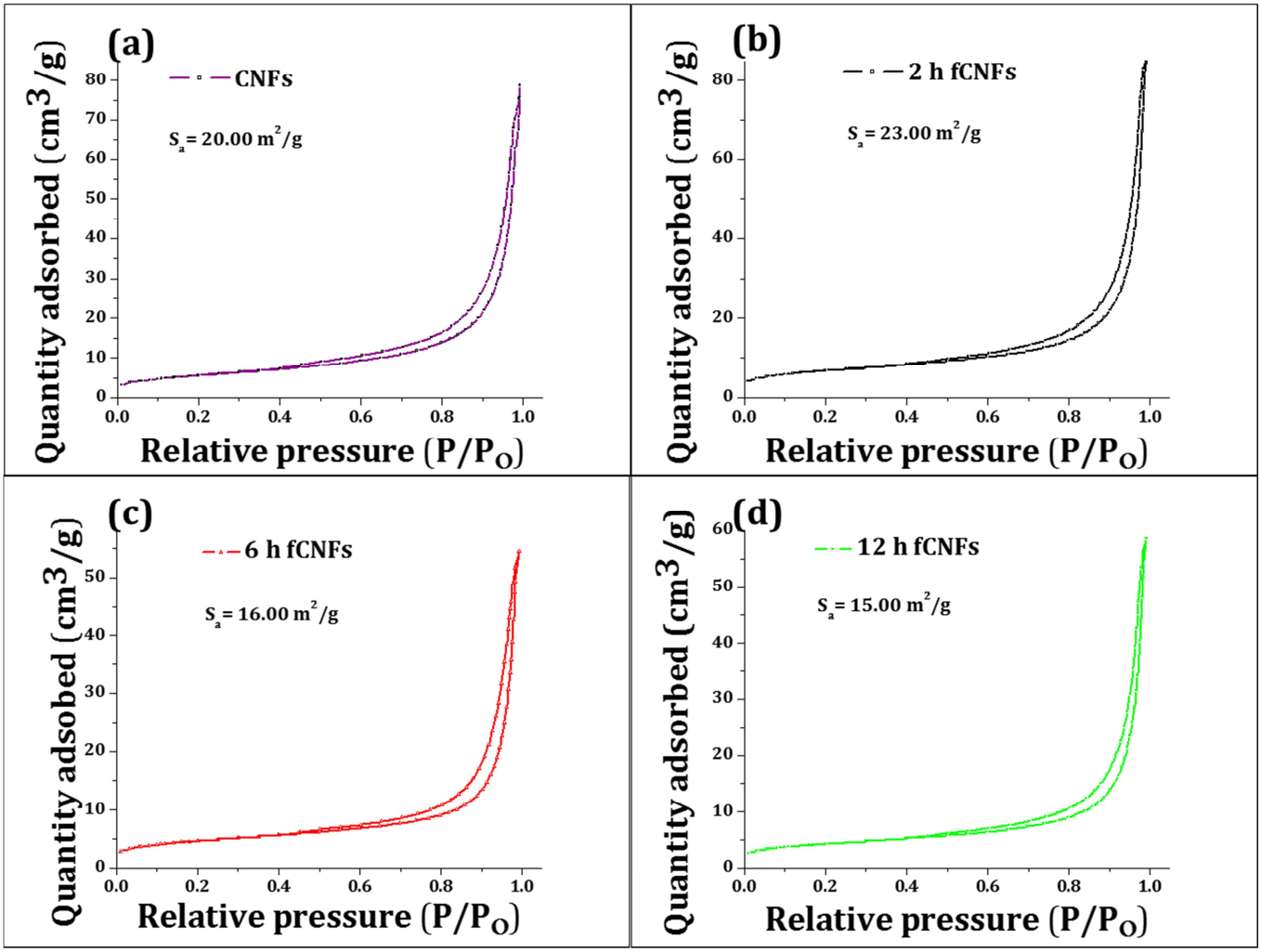

Figure 4.2.6: N_2 BET isotherms of: (a) pristine CNFs, (b) 2 h fCNFs, (c) 6 h fCNFs and (d) 12 h fCNFs.

In their study, Toebes and co-workers found that the total surface area of CNFs increased with increasing severity of the oxidation treatment. They attributed the increase of the surface area to an increase in pore volume of the material [59]. Similarly, another study by Birch and co-workers concluded that the acid functionalisation of their CNF surfaces led to an increase of their surface area. Here they attributed this to the roughening of the CNF surfaces, together with the disruption of their π-π interactions which they believed led to their dispersion and debundling (reduced agglomeration) [60]. Contrary to their observations the data obtained in this study suggested otherwise.

With increased functionalisation time, it was noted that the surface area of the CNFs dropped.

It should be noted that a number of factors influenced the surface areas of the CNFs that they synthesised. These included: the presence of fly ash particles (containing SiO_2 and Al_2O_3), remnant amorphous carbon, their average diameter, surface functionalisation and particle agglomeration [60].

In this study the presence of fly ash particles could potentially have lowered the surface area of the CNFs, functionalised or pristine. In this regard, Hemraj-Benny and his colleagues found that the surface area of their CNTs decreased substantially after ozonolysis-type functionalisation [61]. These authors attributed this observed decrease to the closure of the pores in these CNTs by intercalated acid molecules as well as the introduction of functional groups. In this study, it is plausible to attribute the decrease in the surface area to the abovementioned reason without overlooking the potential contribution by the raw fly ash particles. Hence further studies will need to be conducted to quantify the exact effect of the presence of the fly ash particles on the surface areas of the CNFs produced from raw South African CFA.

TGA characterisation

In order to understand the effects of functionalisation on the thermal stability of the pristine CNFs, TGA analyses were performed. **Fig 4.2.7**(**a**) shows the thermograms of pristine CNFs, fCNFs, and their first derivative curves **Fig 4.2.7** (**b**). The thermograms showed that 18~30% residual mass on average remained after the analysis. This was attributed to the remains of fly ash that were in the pristine CNFs and the fCNFs. The first derivative curves (**Fig 4.2.7** (**b**)) gave the temperatures where the greatest mass loss in the decomposition process were observed. **Fig 4.2.7**(**b**) shows that both the pristine CNFs and fCNFs had two major areas of mass loss: in temperatures close to 500 °C and temperatures above 600 °C. The peaks that appeared at 500 °C were attributed to the decomposition of pristine CNFs and fCNFs with low diameters [31]. They could not be attributed simply to remnant amorphous carbon because it has been well documented in literature that amorphous carbon burns at temperatures below 500 °C [62]. The peaks that were at or above 600 °C were attributed to graphitic carbon of CNFs with larger diameters [19].

Functionalised CNFs were observed to have other regions of mass loss near 100 °C and 300 °C. These were attributed to water that was adsorbed onto their surface [63] and acid moieties. These peaks were not present on pristine CNFs and thus confirmed that functionalisation had led to acid groups attaching to the CNFs and making them more hydrophilic than they were before functionalisation.

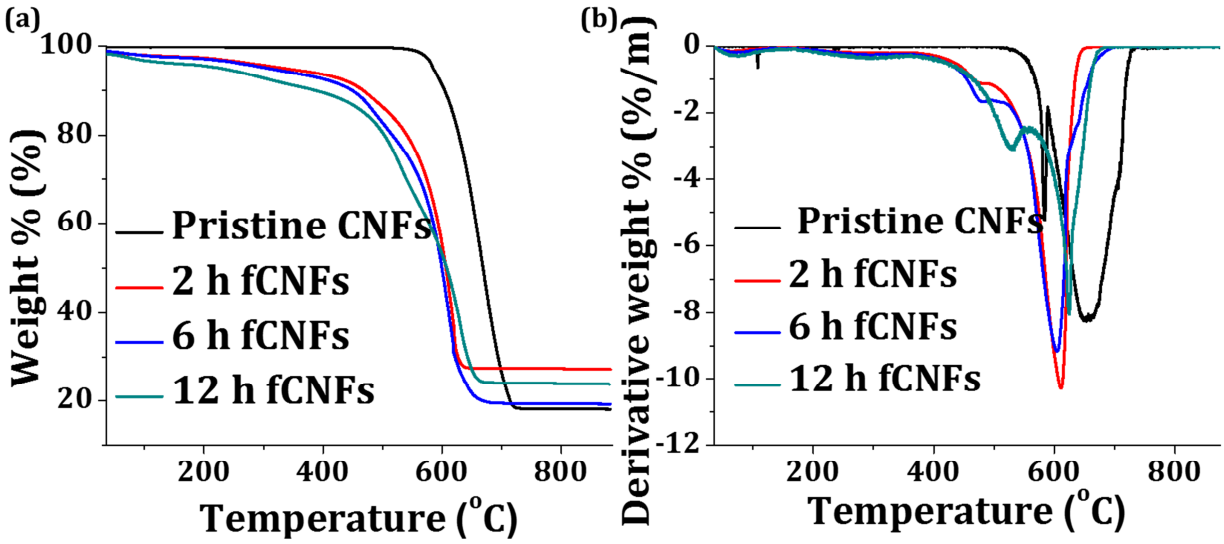

Figure 4.2.7: Thermograms of pristine CNFs (black), 2 h fCNFs (red), 6 h fCNFs (blue) and 12 h fCNFs (turquoise).

In addition it was observed that after functionalisation the fCNFs had a lower decomposition temperatures than the pristine CNFs. This was attributed to the amount of damage and disorder that functionalisation had induced onto the surface of the CNFs. As a general rule it was noted that as more damage was done on the surface of the CNFs, as a result of functionalisation time, they decomposed at lower and lower temperatures by comparison with the pristine CNFs.

Conclusions

Transmission electron microscopy confirmed that the effect of high functionalisation time resulted in the increase of surface defects on the CNFs, as noted by the increased surface roughness that was observed. Laser Raman spectroscopy confirmed the abovementioned observation, as the I_G/I_D ratios decreased as a function of increased functionalisation time. ATR-FTIR spectroscopy confirmed the presence of C=O functional groups after functionalisation. Likewise, increased surface water adsorption was observed with increased functionalisation time. This suggested that the CNFs were more hydrophilic than pristine CNFs after acid functionalisation. The absence of the

broad OH vibration at about 3500 cm^{-1} implied that the C=O group was not a carboxylic group but a carbonyl group.

PXRD analyses showed that all the phases of raw fly ash that were found in pristine CNFs were still found in fCNFs. This implied that acid functionalisation did not remove the fly ash particles. This observation was confirmed by XRF, where it was observed that all the major oxides detectable by XRD were still present after acid functionalisation. However, XRF showed provisionally that the only leachable oxides in the CNFs and fCNFs were: Fe_2O_3, CaO and P_2O_5, which was in agreement with the findings in literature. Furthermore, XRF revealed that a small amount of Fe_2O_3 was leached off as compared to the CaO, which implied that Fe_2O_3 was more tightly bound to the raw fly ash particles than CaO. BET N_2 adsorption and desorption isotherms showed that functionalisation initially caused the surface area to increase by comparison to pristine CNFs. However, with increased functionalisation time the surface area of the fCNFs steadily decreased. Thus the introduction of surface functional groups seemed to be the systematic reason why the fCNFs had lower surface areas. Although the effect of the fly ash amongst the CNFs could not be determined, it was speculated that the closure of pores in the CNFs by the added functional groups had caused this. TGA revealed that functionalisation generally led to the lowering of the thermal stability of CNFs.

4.3 Synthesis of the CNF-TiO_2 hybrids

Since Honda and Fujishima showed the potential of a titania (TiO_2) electrode to split water it has been under intensive research [64], [65]. It is known that TiO_2 is photocatalytic and researchers are striving to enhance its activity. Photocatalysis is a catalytic reaction involving light absorption by a catalyst or substrate.

TiO_2 has three naturally occurring polymorphs: one is orthorhombic (brookite), while rutile and anatase are tetragonal, with different space group symmetries [66]. Among these polymorphs anatase and rutile are more favourable for photocatalysis because brookite is not chemically stable enough to be efficiently photocatalytic [67]. The mobility of electrons in anatase is 89 times higher than in rutile which also has less electron diffusivity as compared to anatase [68]. Thus anatase is better for photocatalytic applications [69]. This owes to the fact that anatase has a broad bandgap of 3.2 eV

(anatase) and thus it can absorb photons with a wavelength equal to or lower than 388 nm (UV light).

When light of the right wavelength penetrates TiO_2 (anatase), electrons are excited from the valence band into the empty conduction band, leaving an electron hole in the valence band (Equation 1). Electrons in the conduction band are good reductants and the holes in the valence band are powerful oxidants. The electron-hole pairs have an oxidising potential of 2.9 V vs the normal hydrogen electrode (NHE), which is enough to oxidise most organic pollutants [67]. Water can interact with the holes generated in the valence band to form hydrogen ions (H^+) and hydroxyl radicals ($HO^\bullet$) (Equation 2) while O_2 gas interacts with the electron in the conduction band to form oxygen radical ions ($O_2^{\bullet-}$) (Equation 3). These ions and radicals can convert most pollutants into H_2O and CO_2 according to the series of equations below:

$TiO_2 + hv \rightarrow h^+ + e^-$ ---------- (Equation 1)

$H_2O + h^+ \rightarrow HO^\bullet + H^+$ ---------- (Equation 2)

$O_2 + e^- \rightarrow O_2^{\bullet-}$ ---------- (Equation 3)

Nano-sized titania particles have a high surface area, which is good for catalytic reactions, but this is not without its own disadvantages. Particle aggregation and recovery of the nanoparticles from reactors is burdensome. Pristine titania as a photocatalyst suffers another disadvantage, in that it has a high recombination rate of the photogenerated electron-hole pair [70]. Thus currently pristine TiO_2 nanoparticles cannot be used for any feasible industrial application.

Numerous ways have been attempted to increase the activity of TiO_2, including: generating defect structures to induce space-charge separation, doping or co-crystallising TiO_2 with other metal or metal oxide nanoparticles, and having TiO_2 nanoparticles anchored on a support that serves as an electron sink [70]. Carbon nanomaterials are known to be potential electron sinks and so many researchers have

attempted to fabricate a nanocarbon-titania hybrid. Acid treated CNFs, synthesised from fly ash, were used as the support for TiO_2 in this present study.

Mixing TiO_2 and carbon in some instances has resulted in the enhancement of photocatalytic activity. Although there is still a dispute as to how this happens per se. Some researchers have implied that simple powder mixing, intimate contact or even wet chemical binding is required to have such an effect [65].

The reason for attempting to chemically bind TiO_2 to carbonaceous substrates is to induce the Ti-O-C bond because it has been suggested that this bond extends light absorption of TiO_2 to longer wavelengths and hence enhances its ability to harvest visible light [65]. Similarly, the interfacial (Ti-O-C) bond can serve as an electron transfer pathway between CNFs and TiO_2, and thus significantly improve the photocatalytic efficiency of the nanohybrid [51]- [55], [71].

Many methods can be employed to make the above-mentioned hybrid, but, the sol-gel [72]- [80] and hydrothermal [47], [81]-[84] techniques are the most widely applied. Numerous scientists have managed in full or partially to coat carbon nanomaterials with TiO_2, particularly carbon nanotubes in their various forms: single-walled and multi-walled [47], [72]-[78], [85]-[87] and carbon nanofibres. In many instances the binding and coating of the TiO_2 was poor and uncontrollable.

Abbasi *et al*. have noted that using sol-gel and other methods to modify the CNT surface resulted in heterogeneous, non-uniform and aggregated decoration of TiO_2 on the surface of CNTs [88]. Woan *et al.* used a hydrothermal method to coat their CNTs with TiO_2 and found that the coverage of these materials was random, and with agglomerates on the surface [80]. Ouzzine *et al.* attempted to coat CNFs with TiO_2 nanoparticles by the sol-gel method and also found that the coating was incomplete, even after these CNFs were acid treated [89]. Xia *et al.* were able to synthesise rice-grain shaped TiO_2 particles next to CNFs using an autoclave-type of hydrothermal reaction; again control of the coverage and the particle size was not possible [90]. The method used in this study was a simple hydrothermal one pot-synthesis done at low temperatures, below 200 °C and atmospheric pressure.

Hydrothermal techniques have been studied in depth and so are better explored than sol-gel methods. Through this technique nano-sized metal oxide particles have been

synthesised at low temperatures, avoiding the calcination step that has been generally required in the sol-gel method [91]. Srivastava *et al.* have confirmed that when the two methods were compared, the hydrothermal one resulted in smaller nanoparticles and used lower temperatures [38]. Yoshimura *et al.* have reviewed methods for the synthesis of such materials and have noted that there were many advantages of using hydrothermal techniques as compared to those like sol-gel, including: energy saving, simplicity, cost-effectiveness, better nucleation control, higher dispersion, higher rate of reaction, better shape control and lower temperature of operation in the presence of an appropriate solvent [82].

In this study a simplified one-pot hydrothermal method to synthesise a CNF-TiO_2 hybrid is presented. Since no one has coated CNFs generated from fly ash with TiO_2, a systematic study of the effect of the reaction time on the extent of TiO_2 coverage on these materials was conducted. Additionally, the effect of increasing the duration of functionalisation of these CNFs on the coating of the TiO_2 nanoparticles was also conducted. In light of the research done by Franklyn *et al.* it was suspected that in the presence of an organic acid (i.e. carboxylic acid functional groups on the surface of CNFs) the $TiCl_4$, in the presence of the fCNFs, would result in the formation of pure anatase only [92].

Experimental and characterisation

Synthesis of the CNF-TiO_2 hybrid

ReagentPlus® grade $TiCl_4$ from Sigma-Aldrich was used for all the experiments. A gram of acid treated CNFs (2, 6 and 12 h fCNFs) were added to round bottom flasks with 200 ml deionised water that was cooled in an ice bath to 0 °C. The mixture was stirred while adding $TiCl_4$ to result in a 10% (m/m) loading of TiO_2 on the fCNFs. The different mixtures were refluxed for 2, 6 and 12 h at 115 °C. The products were centrifuged and rinsed with water to neutrality. They were then oven dried for 8 hours and characterised. All of the samples were synthesised in triplicates.

Characterisation

A Bruker Senterra Dispersive Micro-Raman system equipped with a 532 nm line was used to obtain all of the laser Raman spectra. This technique provided data on the presence of carbon and titania. It also provided the phase of titania that was formed on the fCNFs.

In order to determine the possible presence of the Ti-O-C bond between the fCNFs and the TiO_2, attenuated total reflection-Fourier transform infrared (ATR-FTIR spectroscopy) was used. ATR-FTIR spectra for the CNF-TiO_2 hybrids were obtained using the Bruker Tensor 27 with a ZnSe window (500 – 6000 cm^{-1}).

Thermogravimetric analyses were performed on the CNF-TiO_2 hybrids to determine a number of issues: (i) the amount of fly ash which remained in the products after combustion, (ii) the percentage of TiO_2 present in the hybrids, and (iii) thermal stability changes of the carbon due to the presence of TiO_2. The Perkin-Elmer Simultaneous Thermal Analyser (STA 6000) was used to perform all of these analyses.

Surface area analyses were performed on the CNF-TiO_2 hybrids to compare them to each other and to see if there was any effect of the duration of exposure to $TiCl_4$ to their surface areas, because this can affect the crystallite size. Similarly CNFs which had been functionalised for different durations were studied to see if there was any effect on the dispersion of the TiO_2 nanoparticles and hence the surface area of the CNF-TiO_2 hybrid. The surface area analyses were performed using Micromeritics Tristar 3000 Brunauer-Emmett-Teller surface area analyser.

The phases of the minerals and elements present in the CNF-TiO_2 hybrids were determined by powder X-ray diffraction (PXRD). The diffractometer used was the Bruker D2 PHASER with a LYNXEYE detector. It had a Co K_α source at 30 kV. This technique was used to determine the phase of titania in the hybrid.

The particle size and dispersion of the TiO_2 nanoparticles on the surface of the CNFs and their morphology were also studied using the FEI Tecnai T12 (TEM) which worked at 120 kV.

Results and discussion

CNF-TiO_2 hybrids in this study were synthesised under different conditions to determine the effects of the duration of functionalisation as well as the exposure time of these fCNFs to $TiCl_4$ under different reflux conditions. **Table 4.3.1** provides the naming standard as well as abbreviations that were used in this study for all the data and plots.

The general form for the naming of the hybrids was expressed as: *x* h fNCFs- *y* h $TiCl_4$. Here *x* h and *y* h refer to the number of hours of chemical treatment, be it duration of functionalisation or exposure to $TiCl_4$.

Table 4.3.1: A summary of the CNF-TiO_2 hybrid naming system that was used for independently studying the effects of the duration of functionalisation as well as exposure to $TiCl_4$.

Sample number	***Duration of functionalisation/ h***	***Duration of exposure to $TiCl_4$/ h***	***Sample name***
1	**2**	**2**	**2 h fCNFs - 2 h $TiCl_4$**
2	**6**	**2**	**6 h fCNFs - 2 h $TiCl_4$**
3	**12**	**2**	**12 h fCNFs - 2 h $TiCl_4$**
4	**2**	**6**	**2 h fCNFs - 6 h $TiCl_4$**
5	**6**	**6**	**6 h fCNFs - 6 h $TiCl_4$**
6	**12**	**6**	**12 h fCNFs - 6 h $TiCl_4$**
7	**2**	**12**	**2 h fCNFs - 12 h $TiCl_4$**
8	**6**	**12**	**6 h fCNFs - 12 h $TiCl_4$**
9	**12**	**12**	**12 h fCNFs - 12 h $TiCl_4$**

Laser Raman spectroscopy characterisation

Laser Raman spectra of the CNF-TiO_2 hybrids with fixed functionalisation times at (a) 2 h, (b) 6 h and (c) 12 h, while varying the exposure to $TiCl_4$ time from 2 h, 6 h to 12 h for each set were obtained (**Fig 4.3.1**(**a-c**)).

All these spectra were observed to have had peaks at: 148.6 cm^{-1}, 202 cm^{-1}, 387.8 cm^{-1}, 506.9 cm^{-1}, 624 cm^{-1}. They corresponded to the [E_g], [E_g], [B_{1g}], [$A_{1g}(B_{1g})$] and [E_g] vibration modes of anatase only and no rutile peaks were observed [93].

The peaks at 1343.9 cm^{-1} and 1591.2 cm^{-1} corresponded to the D and G peaks of carbon. In some instances the spectra for 6 h fCNFs- 12 $TiCl_4$ and 12 h fCNFs- 2 h $TiCl_4$ hybrids did not completely show the D and G bands of the CNFs because the intensity of these peaks relative to the anatase peaks caused them to be part of the background (see **Fig 2** (**a & b**) in **Appendix II**).

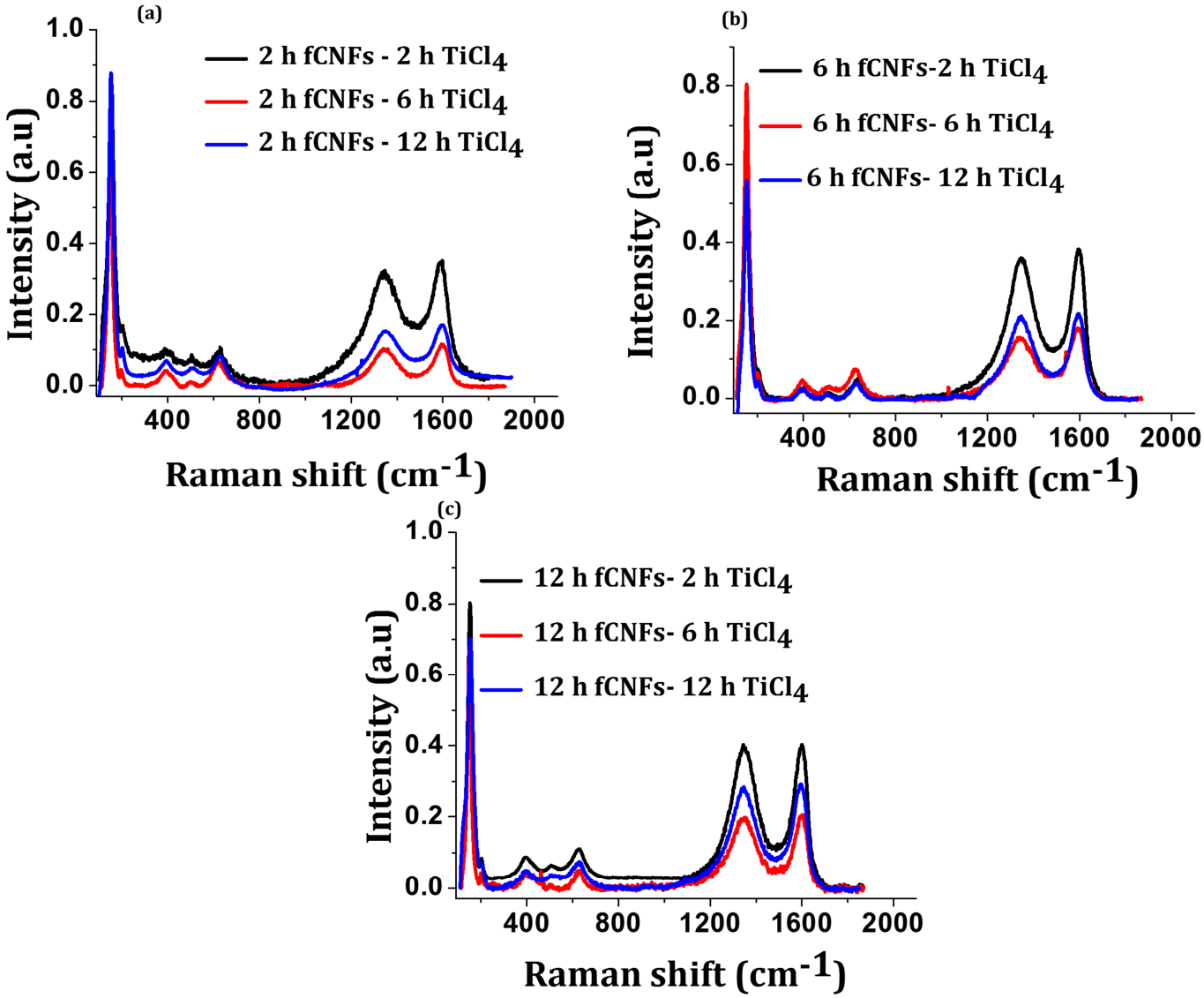

Figure 4.3.1: Laser Raman spectra of the CNF-TiO_2 hybrids showing the effects duration of exposure to $TiCl_4$ to CNFs which were functionalised at: (a) 2 h, (b) 6 h and (c) 12 h.

Laser Raman spectra were obtained for CNF-TiO_2 hybrids which had been prepared for fixed durations of exposure to $TiCl_4$ at: (a) 2 h, (b) 6 h and (c) 12 h, while varying the functionalisation times of the fCNFs from: 2 h, 6 h to 12 h for each set (**Fig 4.3.2** (**a-c**)). All the peaks that were observed for the different exposure times to $TiCl_4$ were observed for the different functionalisation times i.e. anatase and carbon were present throughout. However, as the duration of functionalisation was increased, while the exposure times of $TiCl_4$ were kept constant, no discernible trend in the change in intensity of anatase peaks was observed.

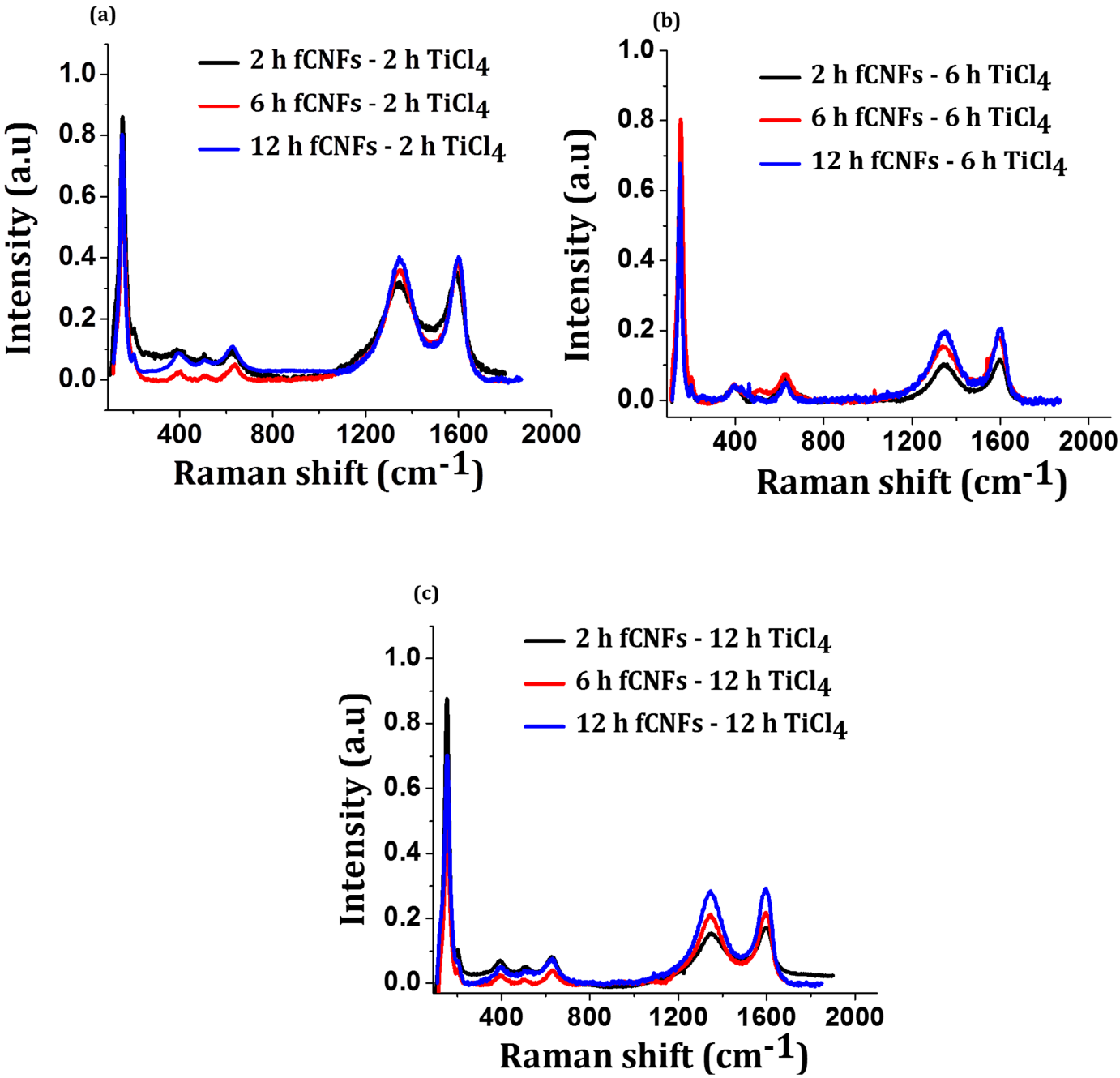

Figure 4.3.2: Laser Raman spectra of the CNF-TiO_2 hybrids showing the effects of the duration of functionalisation of CNFs for: 2, 6 and 12 h on CNFs that were exposed to $TiCl_4$ for: (a) 2 h, (b) 6 h and (c) 12 h.

ATR-FTIR spectroscopy characterisation

ATR-FTIR measurements were performed on selected samples including: the pristine CNFs, fCNFs and a selected CNF-TiO_2 hybrid to track any changes that occurred with subsequent chemical treatment. **Fig 4.3.3** is a plot of the FTIR spectra of the pristine CNFs (blue), fCNFs functionalised for 12 h (red) and CNF-TiO_2 hybrid made from fCNFs that were functionalised for 12 h and exposed to $TiCl_4$ for 2 h (orange).

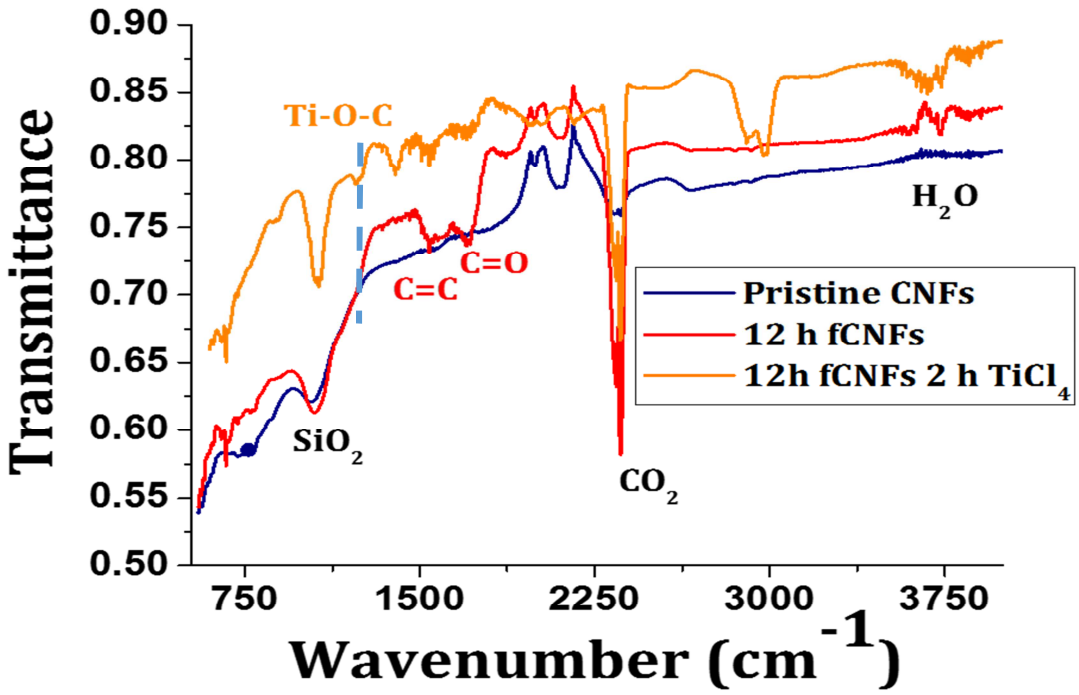

Figure 4.3.3: ATR-FTIR spectra of pristine CNFs (blue), 12 h functionalised CNFs (red) and 12 h fCNF-2 h $TiCl_4$ hybrid (orange) and dashed line indicating the presence of the Ti-C-O bond.

Some peaks were found to be common in all the materials, including: SiO_2 (1047 cm^{-1}), CO_2 (2339 & 2367 cm^{-1}) and anomalous bands (1785 to 2310 cm^{-1}, 2411 to 2697 cm^{-1}) which were probably due to the structure of the CNFs. The SiO_2 bands which originated from the raw fly ash particles were present in all the materials.

Only the fCNFs and the CNF-TiO_2 hybrid showed the presence of adsorbed water (673, 3500-3800 cm^{-1}), whereas these bands were not observed for the pristine CNFs. This was an indicator that functionalisation had resulted in increasing the hydrophilicity of the CNFs and that the hybrid had high affinity for water too. The fCNFs and the CNF-TiO_2 hybrid were observed to have another band at 1707 cm^{-1} that was assigned to the C=O band of the carbonyl functional group, which resulted from functionalisation (refer to **Table 4.3.2**).

A band on the CNF-TiO_2 hybrid at 1349 cm^{-1} was unassigned, but the one close to 1251 cm^{-1} was assigned due to the presence of the Ti-O-C bond [51]-[55]. This suggested that a covalent bond between the fCNFs and the TiO_2 had been made possible by the anchoring of C=O functional groups on the fCNFs through acid treatment (This will be discussed later).

One major difference between the pristine CNFs and fCNFs from the hybrid was the shift of the C-H bands to higher wavenumbers from: 2852 cm^{-1} and 2926 cm^{-1} for pristine fCNFs to 2909 cm^{-1} and 2981 cm^{-1} for the CNF-TiO_2 hybrid. This shift was believed to have qualitatively validated the formation of these Ti-O-C bonds, since the only major difference between the CNF-TiO_2 hybrids and the non-hybrids was the presence of TiO_2 nanoparticles on their surface.

Table 4.3.2: Tabulated summary of differences in the ATR-FTIR data between the: pristine CNFs, fCNFs and the 12 h fCNF- 2 h $TiCl_4$ hybrid.

***Wavenumber* (cm^{-1})**	***CNFs***	***fCNFs***	***CNF-TiO_2***	***Assignment***
1047	√	√	√	O-Si-O (SiO_2)
2339, 2367	√	√	√	O=C=O (CO_2)
673, 3500-3800	**x**	√	√	H-O-H (H_2O)
1556	√	√	√	C=C
1707	**x**	√	√	C=O
2852,2926 (2909, 2981)	√	√	√	C-H
1252	**x**	**X**	√	Ti-O-C
1785-2310 ,2411- 2697	√	√	√	Anomalous bands
1394	**x**	**X**	√	Unassigned band

ATR-FTIR studies were performed on the CNF-TiO_2 hybrids to establish the effects of the duration of functionalisation and exposure time to $TiCl_4$ (**Fig 4.3.4 and Fig 4.3.5**). The variation of the quantity of functional groups that were present on the hybrid as a function of different exposure times i.e. 2, 6 and 12 h to $TiCl_4$ were shown in **Figs 4.3.4** (**a-c**) respectively and the maximum intensities of the Ti-O-C peaks are summarised in **Table 4.3.3**.

Table 4.3.3: Tabulated summary of the maximum intensity of the 1251 cm^{-1} bands across all the CNF-TiO_2 hybrids.

		Functionalisation		
	Time/ h	*2*	*6*	*12*
Exposure to $TiCl_4$	*2*	0.2180	0.0275	0.0290
	6	0.0350	0.0387	0.0390
	12	0.0390	0.0346	0.0510

Table 4.3.3 shows that the maximum intensity of the CNF-TiO_2 hybrids increased with increasing $TiCl_4$ exposure in any of the given hybrids. The exception being the 6 h fCNF-6 h $TiCl_4$ sample as its intensity was higher than that of the 6 h fCNF- 12 h $TiCl_4$ hybrid. This observation suggested that more of TiO_2 was bound to the fCNFs with increasing $TiCl_4$ exposure, which led to the increase in intensity of the Ti-O-C bond. However, these peaks weren't the only ones that intensified with increasing exposure time, H_2O bands were observed to do the same. This suggested that as more TiO_2 was deposited on the surface of the fCNFs, this resulted in more H_2O adsorption capacity of the hybrid. This is to be expected as both gases adsorb strongly to TiO_2. No major shifts in the peak position as a function of varying the duration of exposure to the $TiCl_4$, under constant times of functionalisation, were noticed.

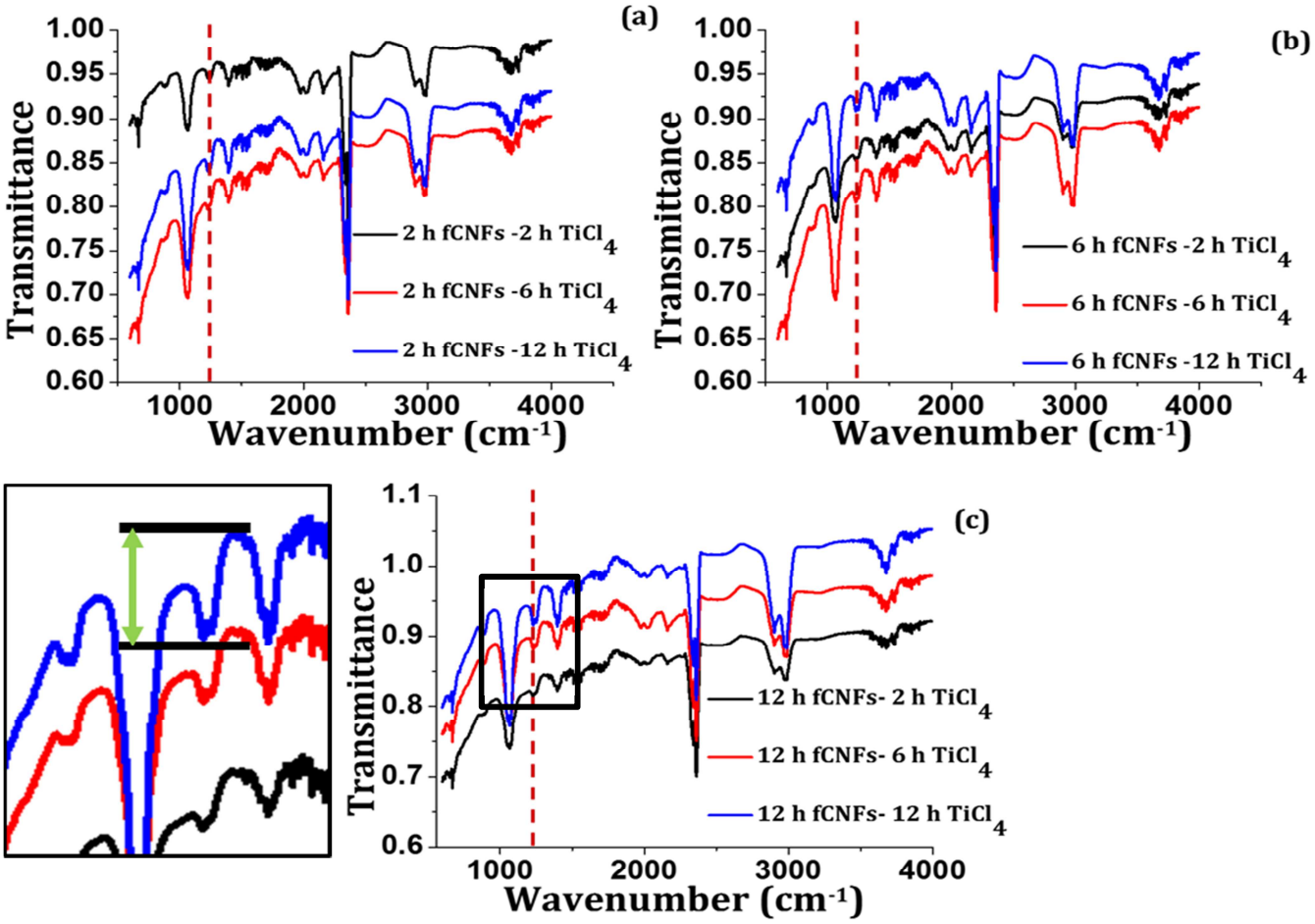

Figure 4.3.4: ATR-FTIR spectra of the CNF-TiO_2 hybrid showing the effects of $TiCl_4$ exposure time of 2, 6 and 12 h for CNFs functionalised at (a) 2 h, (b) 6 h and (c) 12 h and the insert indicating the method for obtaining peak intensities.

In direct contrast, when the effect of functionalisation (2, 6 and 12 h) at fixed $TiCl_4$ exposure times (per functionalisation time i.e. 2, 6 and 12 h) was monitored, it was noted that the Ti-O-C bond was not as affected by the increase in functionalisation time see dotted line in **Figs 4.3.5** (**a-c**) and refer to **Table 4.3.3**.

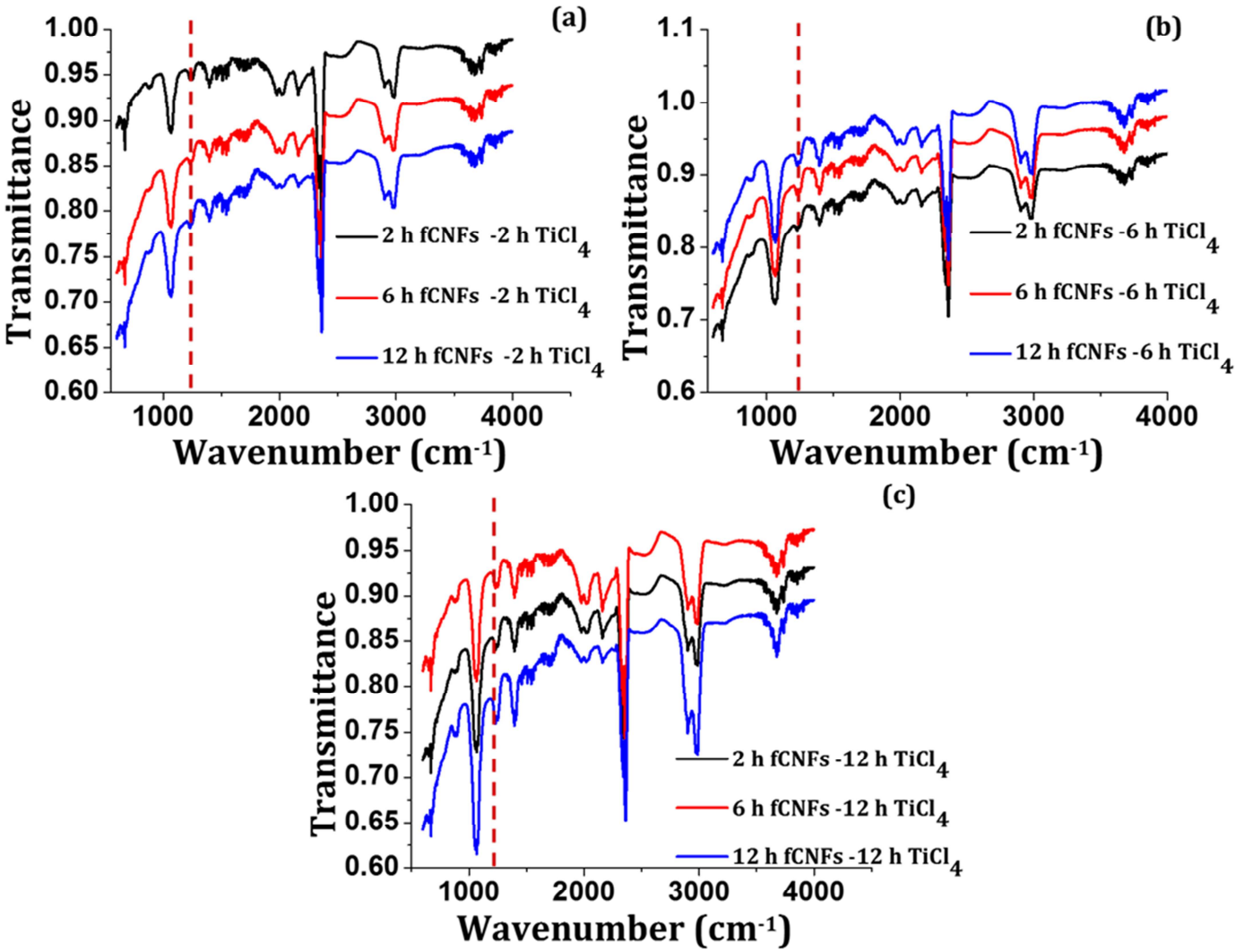

Figure 4.3.5: ATR-FTIR spectra of the CNF-TiO_2 hybrids showing the effects of functionalising CNFs for 2, 6 and 12 h on CNFs exposed to $TiCl_4$ for (a) 2 h, (b) 6 h and (c) 12 h.

Here it was expected that the increase in functionalisation time would have increased the amount of C=O functional groups on the CNF surface, and hence systematically increased the intensity of the Ti-O-C peaks as more TiO_2 was expected to be added and that was so, except when looking at the 6 h fCNF- 12 h $TiCl_4$ hybrid which was lower than that of the 6 h fCNF- 12 h $TiCl_4$ hybrid. However, the change in the Ti-O-C peak

intensity was not as perceptible as it was with the change in duration of exposure to $TiCl_4$, as suggested before.

This suggested that the duration of functionalisation and the duration of exposure to $TiCl_4$ work hand in hand in a complementary way to increase the Ti-O-C bond intensity. This also suggested that the formation of the Ti-O-C is dependent on the amount of C=O functional groups present on the fCNFs, but more so on the time of exposure to $TiCl_4$. Thus even if the fCNFs were functionalised for 12 h, if they were not exposed to $TiCl_4$ for longer periods (6 and 12 h) the Ti-O-C bond intensity increase was not substantially higher than those functionalised at 6 h (5% difference).

Yet, on the other hand, fCNFs functionalised at 2 h had substantial increase in the Ti-O-C bond intensity as a function of increasing the $TiCl_4$ exposure duration from 2 h to 6h (38% difference).

It should be noted as well that this is only a provisional explanation of what might have occurred, since there is no single standard ATR-FTIR of a carbon nanomaterial-TiO_2 hybrid in the literature. Indeed, most of the work that has been performed on carbon nanomaterial-TiO_2 composites thus far has explored ATR-FTIR spectroscopy only in a minor way and even then these results, perhaps due to different starting materials and methods of synthesis, have not been in agreement [36], [70], [82], [84], [90], [93]-[102]. Furthermore, the inconsistency of the possibility of finding the peaks has to do with the difference of starting materials and methods of synthesis.

Thus from this study a band near 1251 cm^{-1} was attributed to the Ti-O-C bond because of its close agreement with a few instances cited in the literature [51]-[55]. These researchers were working with organic polymer-TiO_2 and not carbon nanomaterial-TiO_2 composites. What was found in these articles was that the Ti-O-C bond wavenumbers ranged from 1251 cm^{-1} to 1266 cm^{-1}, thus with a reasonable amount of confidence, since the CNF-TiO_2 hybrids have a peak in this region, it can be said that the Ti-O-C bond was formed between the TiO_2 nanoparticles and the fCNFs.

Another method to confirm the presence of the Ti-O-C bond is using HRTEM image analyses. Epitaxial interactions between the CNFs and the TiO_2 nanoparticle interface, observed using HRTEM, could be used to determine any structural influence the fCNFs may have had on the growth of the anatase nanoparticles. If, during these analyses,

there was evidence showing strain within the nanoparticles or alignment of TiO_2 fringes with the ones on the fCNFs then it could be said that there is a chemical interaction between the two [103]. This method of determining the presence of the Ti-O-C bond within the hybrids will be detailed in the TEM characterisation section.

In order to confirm the phases present in the CNF-TiO_2 hybrids, PXRD analyses were performed on these materials.

PXRD characterisation

PXRD patterns were obtained for all the CNF-TiO_2 hybrids that were synthesised under different conditions. **Fig 4.3.6** (**a**) is a 3D waterfall plot of all these hybrids. It was observed that all the patterns had common peaks throughout, including: carbon, mullite, quartz and haematite (please refer to **section 4.1, Fig 4.1.2**). However, the peaks of focus in this study were those of titania. Here PXRD indicated that there was one phase of titania throughout the different reaction conditions i.e. anatase.

This was evident when a 2D plot of the same patterns was drawn, as shown in **Fig 4.3.6** (**b**). Peaks at 29.6°, 44.6°, 56.6°, 74.8° and 89.7° 2θ angles (see arrows) all belonged to the anatase phase of titania and corresponded to the (011), (112), (020), (024) and (017) reflections. No other titania phases were detected, thus this method produced anatase nanoparticles exclusively.

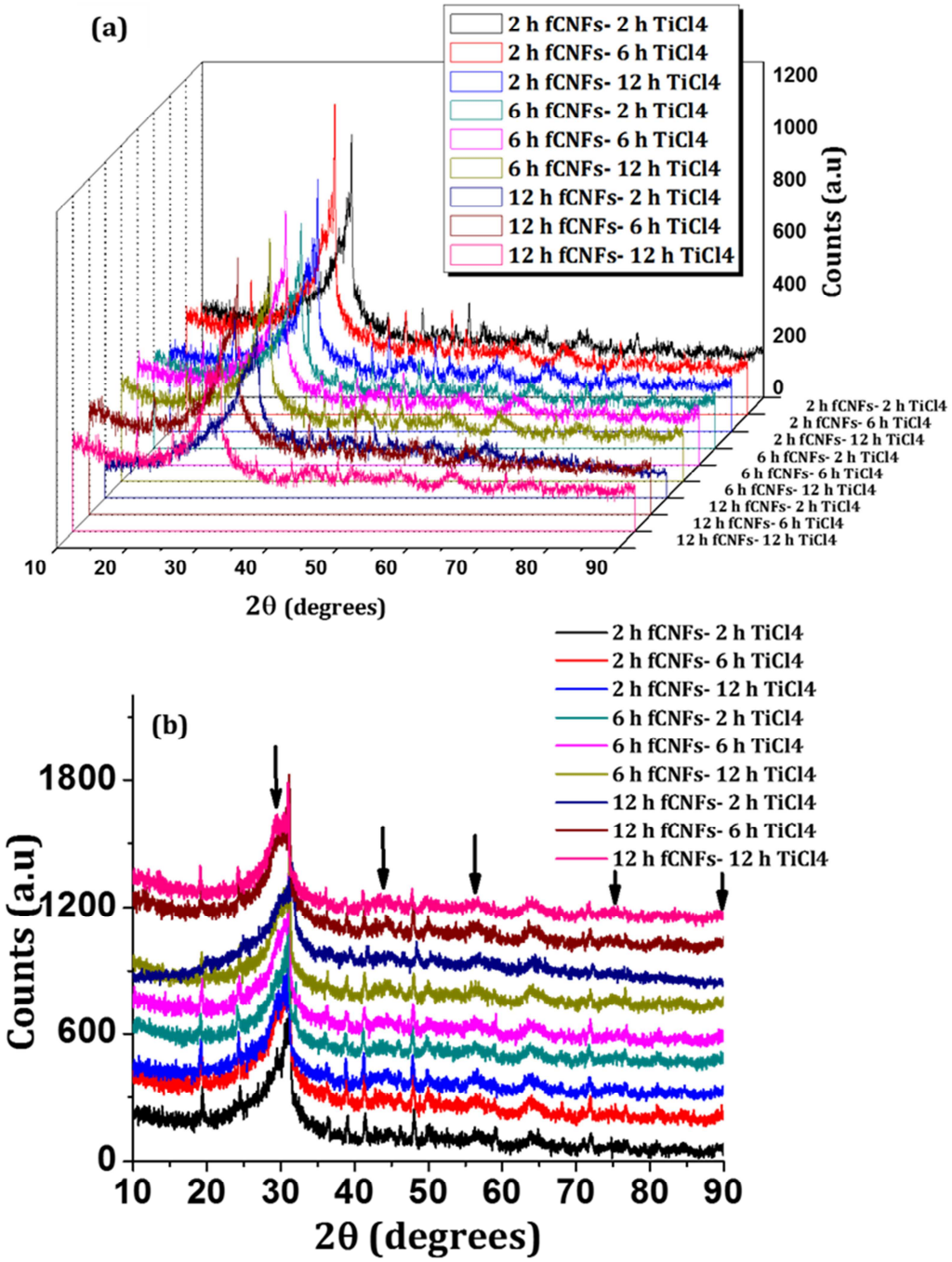

Figure 4.3.6: (a) Waterfall PXRD patterns of the CNF-TiO_2 hybrids showing all the peaks present, (b) superimposed PXRD patterns of the CNF-TiO_2 hybrids showing the anatase peaks at: 29.6°, 44.6°, 56.6°, 74.8° and 89.7° 2θ angles (see arrows).

The surface area of the hybrids were then determined to establish which combination of conditions led to a hybrid that gave the highest surface area.

BET characterisation

N_2 adsorption-desorption isotherms were obtained for the CNF-TiO_2 hybrids to compare the effects of: (i) duration of exposure to $TiCl_4$ at fixed functionalisation times (e.g. samples 1, 4 and 7 in **Table 4.3.4**) and (ii) functionalisation time at fixed $TiCl_4$ (e.g. samples 1, 2 and 3 in **Table 4.3.4**).

Table 4.3.4: A summary of the N_2 BET specific surface areas of various hybrids formed when the effects of the duration of exposure to $TiCl_4$ and functionalisation were studied.

Sample number	***Sample name***	***Specific surface area*** (m^2/g) (***repeat 1***)	***Specific surface area*** (m^2/g) (***repeat 2***)	***Specific surface area*** (m^2/g) (***repeat 3***)	***Standard deviation***	***Average specific surface area*** (m^2/g)
1	**2 h fCNFs - 2 h $TiCl_4$**	63	71	65	3.4	66
2	**6 h fCNFs - 2 h $TiCl_4$**	57	56	70	6.4	61
3	**12 h fCNFs - 2 h $TiCl_4$**	63	64	56	3.6	61
4	**2 h fCNFs - 6 h $TiCl_4$**	62	44	56	7.5	54
5	**6 h fCNFs - 6 h $TiCl_4$**	44	37	42	2.9	41
6	**12 h fCNFs - 6 h $TiCl_4$**	64	41	55	9.5	53
7	**2 h fCNFs - 12 h $TiCl_4$**	64	57	62	2.8	61
8	**6 h fCNFs - 12 h $TiCl_4$**	52	45	49	2.9	49
9	**12 h fCNFs - 12 h $TiCl_4$**	55	57	53	1.6	55

The effect of the duration of exposure to $TiCl_4$ at fixed functionalisation times on surface area

The effects of the exposure to $TiCl_4$ at fixed functionalisation times on the surface area of the resultant hybrids were studied (**Figs 4.3.7**(**a-c**)). All of the isotherms obtained were of the type IV kind according to the IUPAC, which suggested that multi-layer adsorption processes, characteristic of mesoporous materials, had taken place [29].

In all cases it was observed that the final surface area of each hybrid (at fixed functionalisation times) was lower after longer durations of exposure to $TiCl_4$. However, no discernible trend other than this was observed, as exposure to $TiCl_4$ at 2 h (black) and 12 h (green) produced hybrids that had similar surface areas, while exposure to $TiCl_4$ at 6 h (red) produced hybrids that had the lowest surface area. Possible reasons for these observations may include: agglomeration of TiO_2 nanoparticles [105], the amount of fly ash that remained in the CNF-TiO_2 hybrid and the sizes of the TiO_2 nanoparticles that were formed.

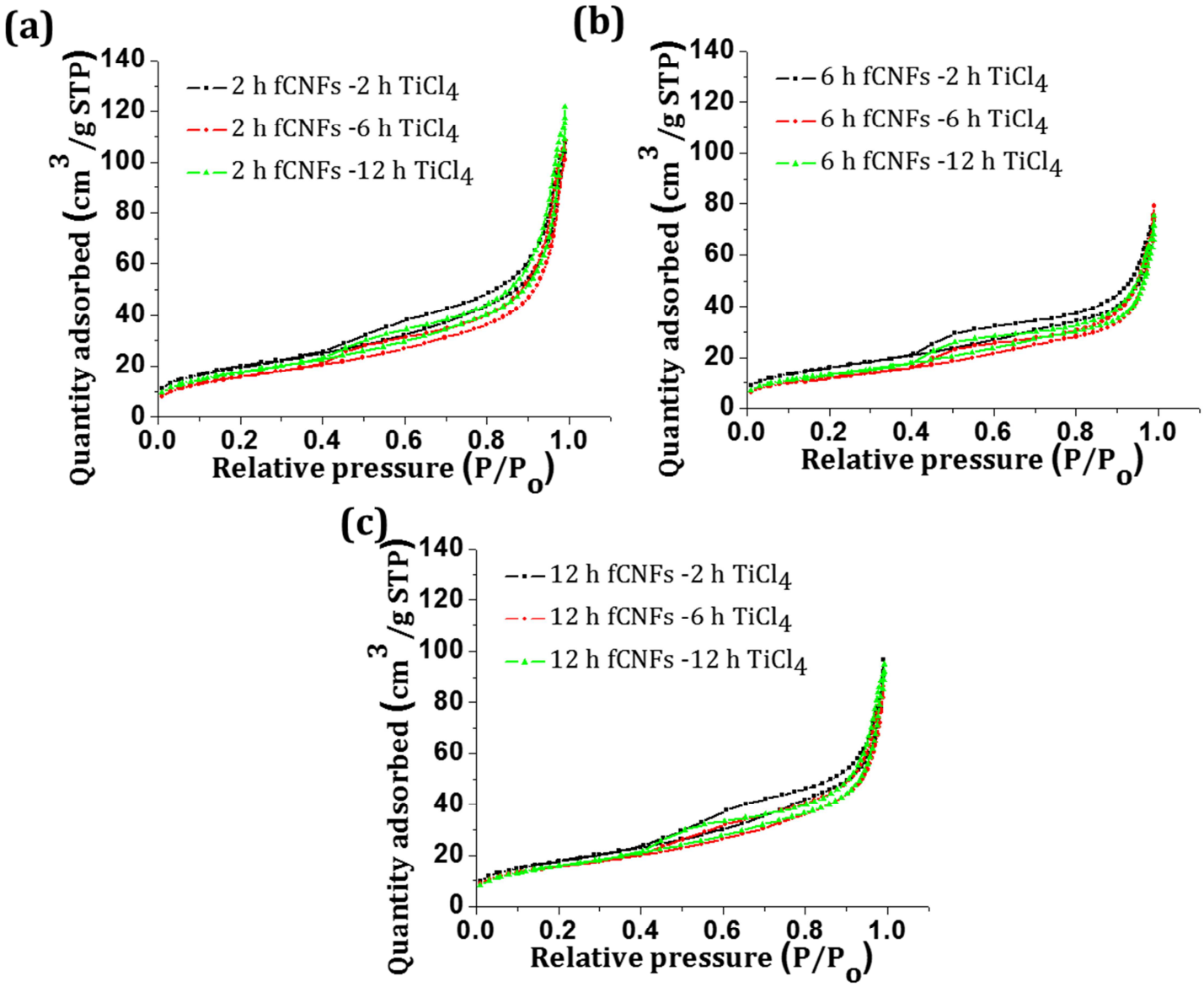

Figure 4.3.7: BET N_2 adsorption isotherms of the CNF-TiO_2 hybrid showing the effects of $TiCl_4$ exposure time of 2 (black), 6 (red) and 12 h (green) for CNFs functionalised at (a) 2 h, (b) 6 h and (c) 12 h.

However, the extent to which each of these factors may have affected the surface area could only be speculated upon without corroborating evidence from other characterisation techniques.

The effect of the functionalisation time at fixed durations of exposure to $TiCl_4$ on surface area

As before, when the N_2-adsorption desorption isotherms were plotted (**Figs 4.3.8 (a-c)**), they were identified as type IV, which were characteristic of mesoporous materials.

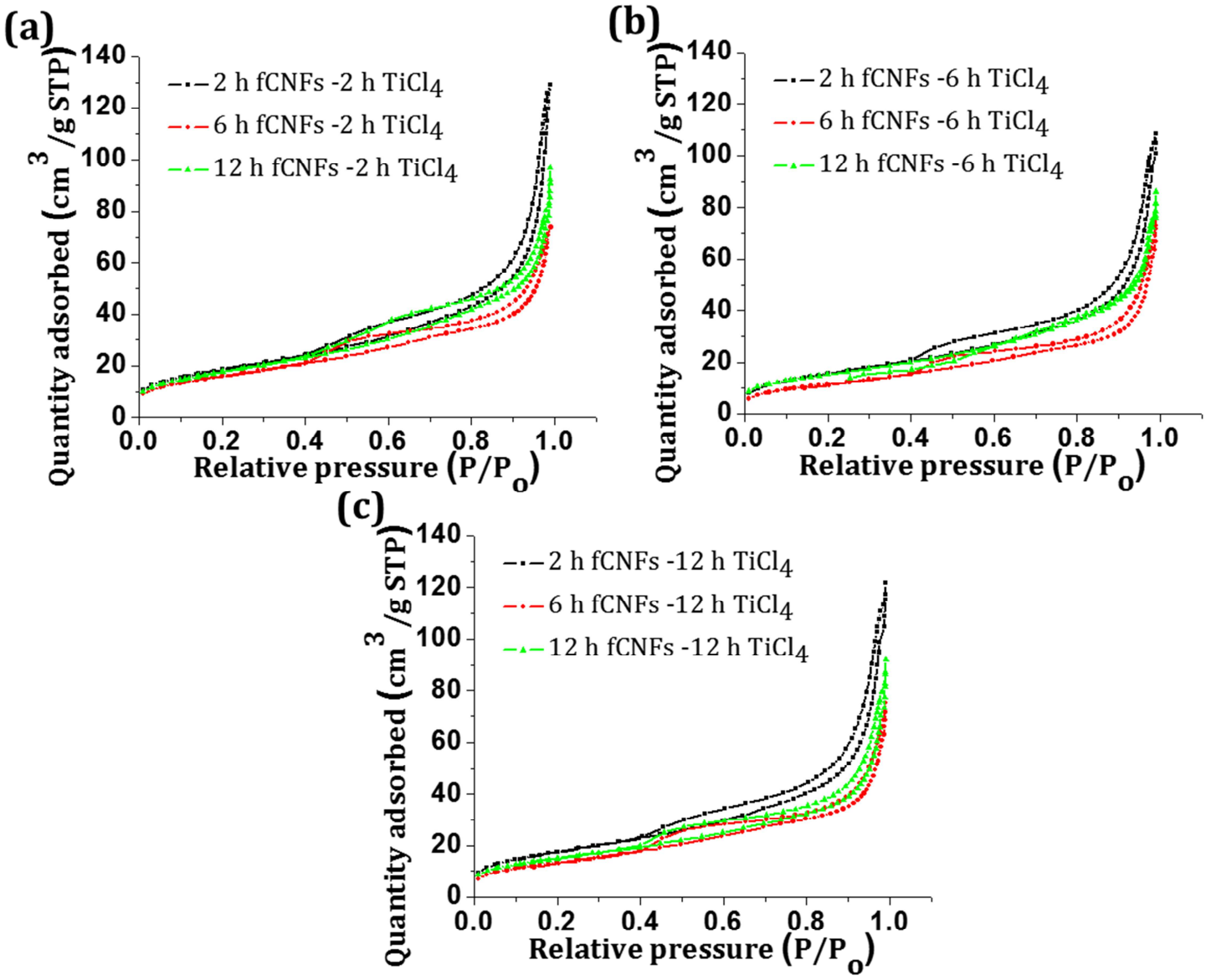

Figure 4.3.8: BET N_2 adsorption isotherms of the CNF-TiO_2 hybrids showing the effects of the duration of CNF functionalisation for 2 h (black), 6 h (red) and 12 h (green) when exposed to $TiCl_4$ for (a) 2 h, (b) 6 h and (c) 12 h.

Similarly, surface areas were found to be lower, in all cases, after longer functionalisation times. Once again, no continuous trend was observed as CNFs which had been functionalised for longer periods (samples 3,6 and 9 in **Table 4.3.4**) had higher surface areas than those that had been functionalised for shorter periods (samples 2,5 and 8 in **Table 4.3.4**).

Again, the results were anomalous- on one hand the functionalisation times may have been expected to cause more surface functional groups which in turn may have been expected to make the TiO_2 particles, which were deposited to be either bigger or more

agglomerated. On the other hand the amount of fly ash in each hybrid may have affected the resulting surface areas. To summarise the above observations in a simpler way to visualise refer to **Fig 4.3.9**.

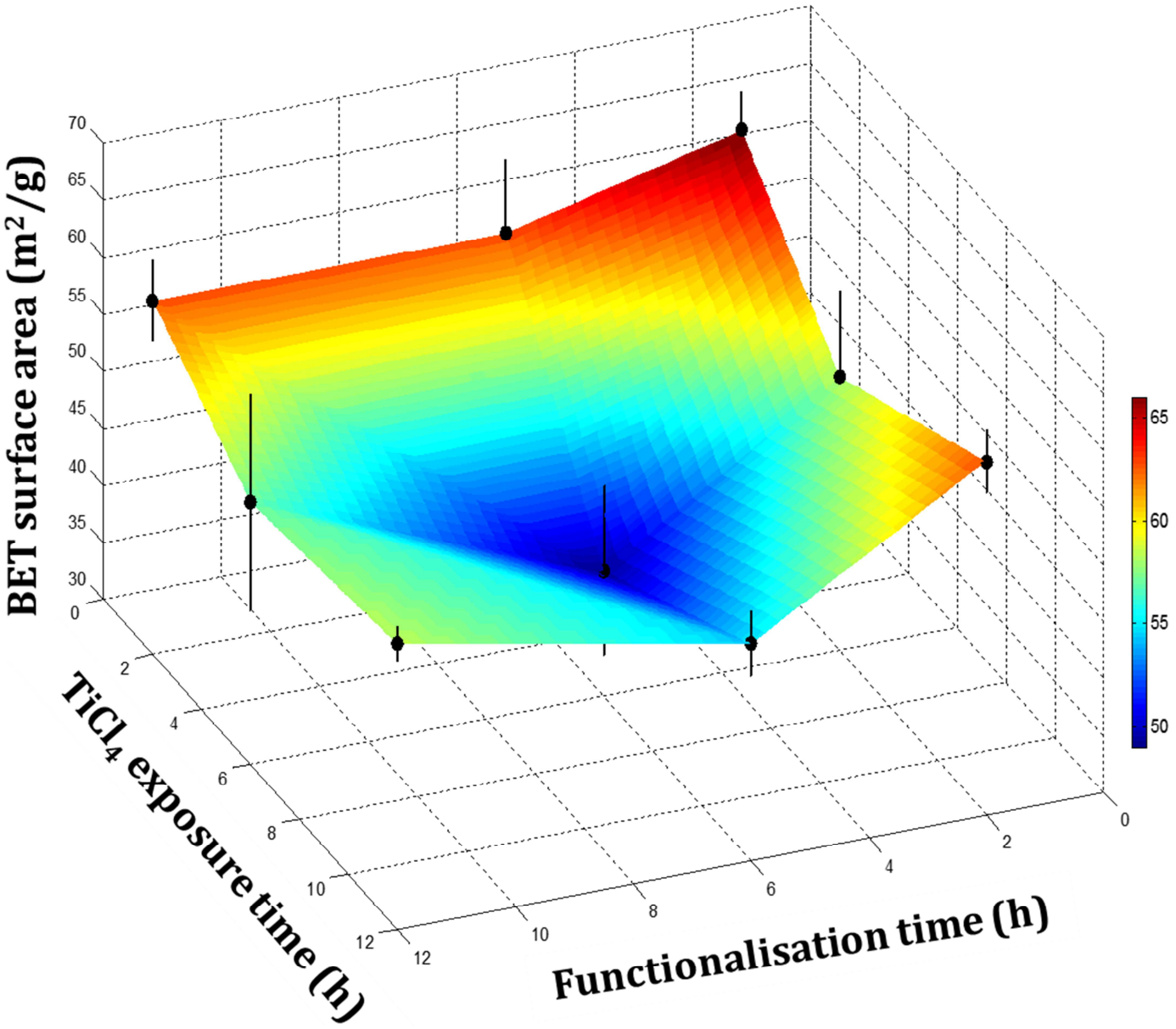

Figure 4.3.9: A 3D surface plot summarising the N_2 BET specific surface areas of various hybrids formed when the effects of the duration of exposure to $TiCl_4$ and functionalisation were studied.

Thermogravimetric analyses of the hybrids were then performed in an attempt to elucidate the possible effects that fly ash and TiO_2 nanoparticles had on the physical characteristics of the resultant CNF-TiO_2 hybrids.

TGA characterisation

Thermograms obtained for the CNF-TiO_2 hybrids that were functionalised at fixed times (a) 2 h, (b) 6 h and (c) 12 h and $TiCl_4$ exposure times that varied from 2 h (black), 6 h (red) and 12 h (blue) are shown in **Figs 4.3.10** (**a-c**). Minor differences in their residual masses were observed among the CNFs that were functionalised at fixed times with different $TiCl_4$ exposure times.

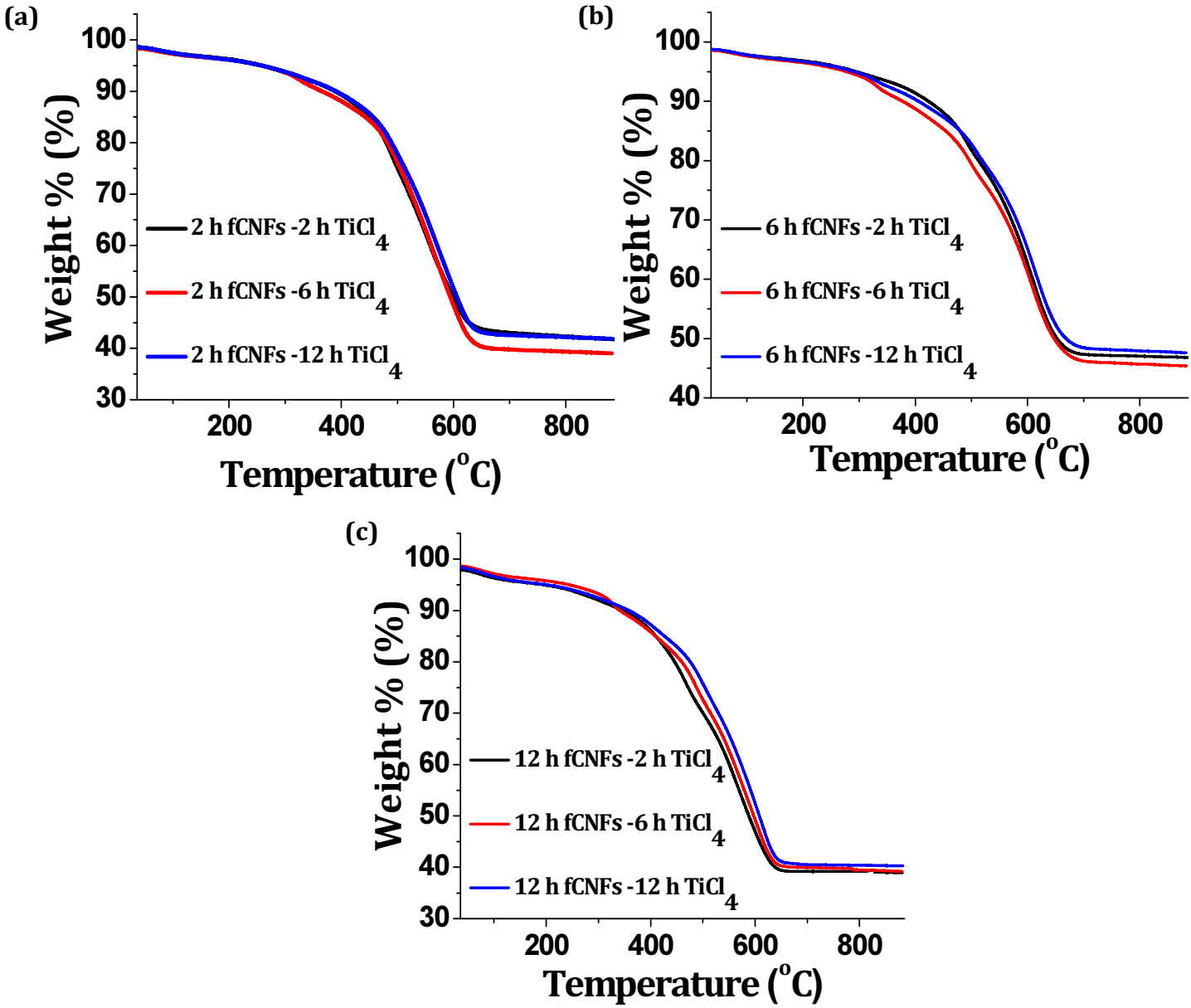

Figure 4.3.10: TGA thermograms of the CNF-TiO_2 hybrids showing the effects of exposure times of $TiCl_4$: 2 (black), 6 (red) and 12 h (blue) for CNFs functionalised at: (a) 2 h, (b) 6 h and (c) 12 h.

These differences could be attributed to the inhomogeneity of the starting material i.e. CFA. As observed in Chapter 4.2 the variance of the residual weight %s of the fly ash in the CNFs and fCNFs ranged from 18~30%. With the assumption that all of the hybrids had 10% of their residual weights accounted for by TiO_2 nanoparticles, the differences of the residual weight %s lie within the 18~30% range, with minor deviations i.e. sample 5 in **Table 4.3.5**.

When the different sets were compared across the various functionalisation times, it was noted that on average the CNFs that had been functionalised for 6 h (samples 2, 5 and 8 in **Table 4.3.5**) had higher residual masses when compared to those at 2 h and 12 h. A tabulated summary of the average residual weight %s left after TGA analyses for all the hybrid samples is presented in **Table 4.3.5**.

Table 4.3.5: A tabulated summary of the residual weight %s that were found when the effect of exposure to $TiCl_4$ and functionalisation on the CNF-TiO_2 hybrids was studied.

Sample number	***Sample name***	***Residual weight %*** (***%***) (***Repeat 1***)	***Residual weight %*** (***%***) (***repeat 2***)	***Residual weight %*** (***%***) (***repeat 3***)	***Standard deviation***	***Average residual weight %*** (***%***)
1	**2 h fCNFs - 2 h $TiCl_4$**	40	42	41	0.74	41
2	**6 h fCNFs - 2 h $TiCl_4$**	41	47	45	2.45	44
3	**12 h fCNFs - 2 h $TiCl_4$**	42	40	34	3.4	39
4	**2 h fCNFs - 6 h $TiCl_4$**	41	39	41	0.88	40
5	**6 h fCNFs - 6 h $TiCl_4$**	47	45	47	0.85	46
6	**12 h fCNFs - 6 h $TiCl_4$**	48	34	36	6.2	39
7	**2 h fCNFs - 12 h $TiCl_4$**	39	42	43	1.70	41
8	**6 h fCNFs - 12 h $TiCl_4$**	39	48	43	3.70	43
9	**12 h fCNFs - 12 h $TiCl_4$**	40	35	39	2.3	38

Thermograms (**Fig 4.3.11** (**a-c**)) obtained for the CNF-TiO_2 hybrids that were exposed to $TiCl_4$ at fixed times for (a) 2 h, (b) 6 h and (c) 12 h and varying functionalisation times from: 2 h (black), 6 h (red) and 12 h (blue).

Based upon the data on **Table 4.3.5** it was observed that on the CNFs that were functionalised at 2 h (samples 1, 4 and 7) and 12 h (samples 3, 6 and 9) seemed to have had lower quantities of residual weight %s when compared to those functionalised at 6 h (samples 2, 5 and 8).

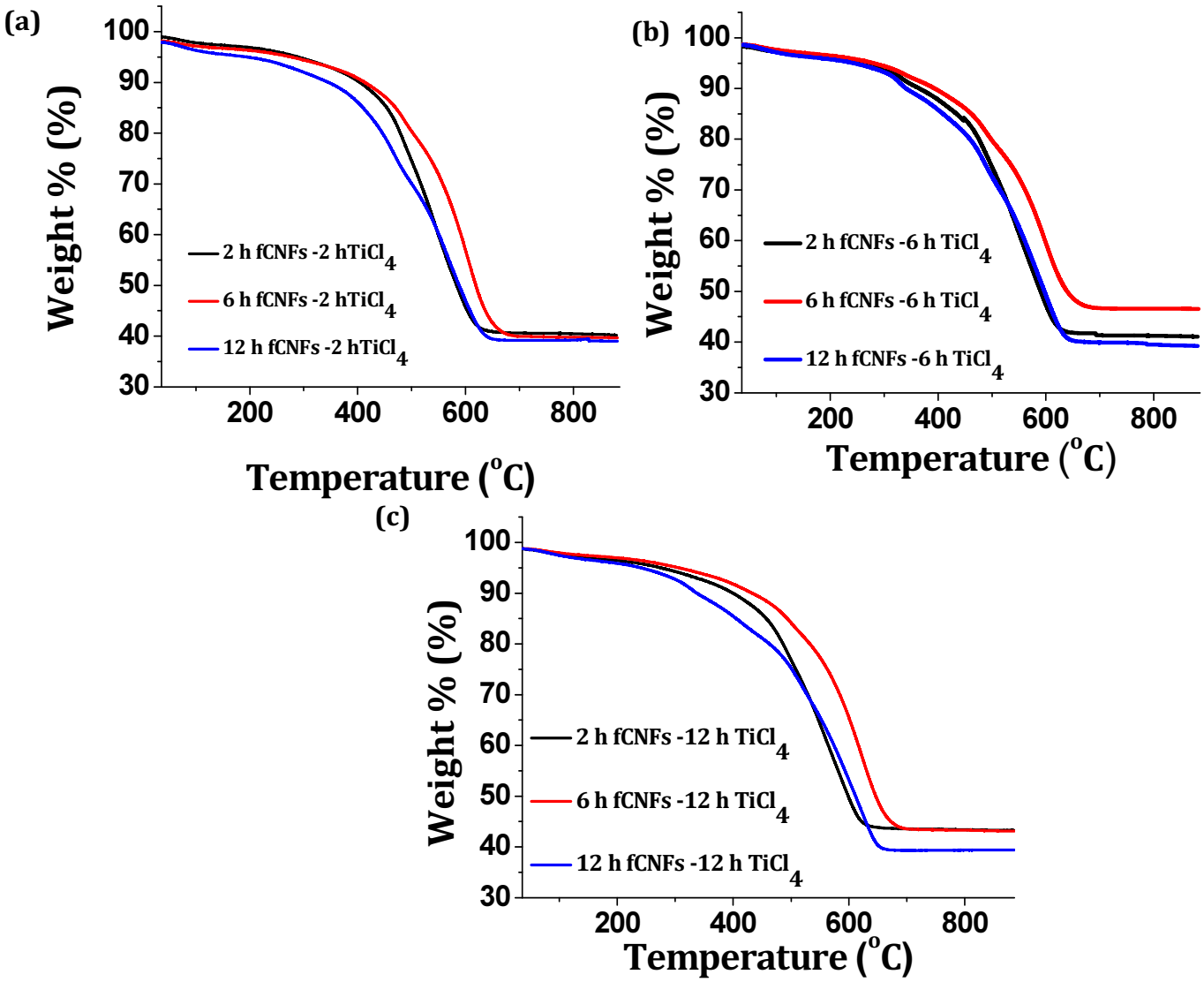

Figure 4.3.11: TGA thermograms of the CNF-TiO_2 hybrids showing the effects of functionalising CNFs for: 2 h (black), 6 h (red) and 12 h (blue) when exposed to $TiCl_4$ for (a) 2 h, (b) 6 h and (c) 12 h.

Thus when the BET data was correlated with the TGA data, this suggested that one of the main reasons that the CNFs that were functionalised at 6 h seemed to have lower specific surface areas than those at 2 h and 12 h, excluding the loading of TiO_2 which was 10% in each case, was the increased presence of fly ash. These observations are summarised in **Fig 4.3.12**.

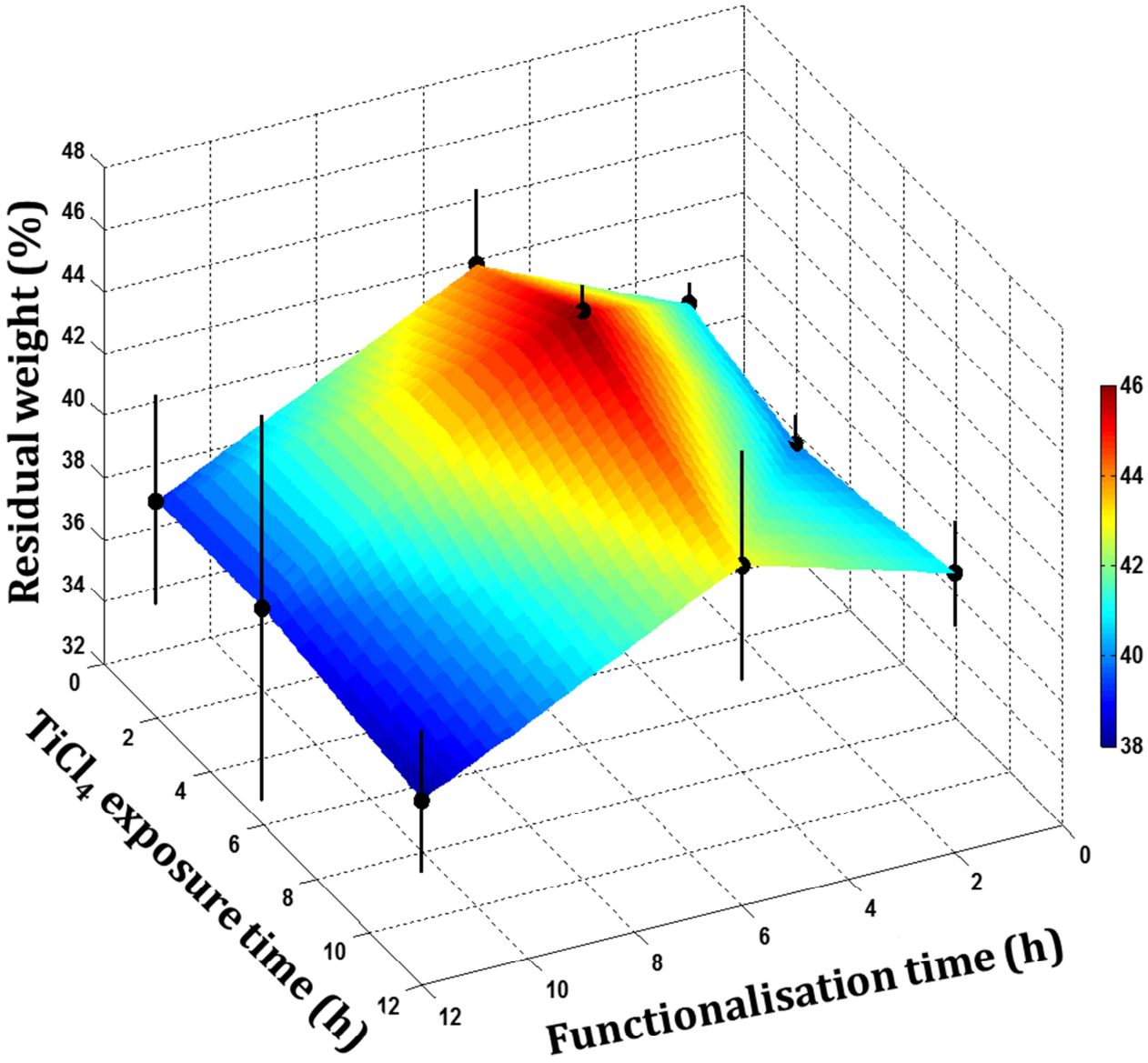

Figure 4.3.12: A 3D surface plot summarising the residual weight %s of various hybrids formed when the effects of the duration of exposure to $TiCl_4$ and functionalisation were studied.

By comparing **Fig 4.3.9** and **Fig 4.3.12** it can be seen that the 6 h fCNF-$TiCl_4$ hybrid corresponding to the highest residual weight % has the lowest surface area. This trend

is a generalised one because it was not consistent throughout. The hybrids that were treated with $TiCl_4$ for 2 h had the overall highest surface areas irrespective of the amount of fly ash within the hybrid. This trend seemed to hold even on hybrids functionalised for 2 h as well. In a different instance the 2 h fCNF-$TiCl_4$ hybrid had the lowest residual weight % but its surface area is not the highest. Although it is evident in some points that the residual weight % plays a major role in affecting the surface area. It is also clear, as previously stated, that the various factors that could have potentially affected the surface area are related in a far more complex way than anticipated.

In order to establish if TiO_2 particle size and/or agglomeration had played any role in these observations, TEM studies were performed on the CNF-TiO_2 hybrids.

TEM characterisation

In an attempt to make sense of the surface area differences and the anomalous trends between the differently treated CNF-TiO_2 hybrids that had been observed, morphological studies were conducted on these materials by TEM. In particular the average size distribution of the TiO_2 nanoparticles, as a function of the exposure to $TiCl_4$ for different durations as well as functionalisation times, were studied.

Manual image analyses of the TEM images is good for assessing the morphology, dispersion and agglomeration of nanoparticles but it is not as effective at determining particle size distribution[106]. The main reason why this is so, is that relatively few particles are examined and there is a high probability of unrepresentative sampling and TEM only shows 2 of 3 dimensions of particles. For any statistically valid representation no less than 500-1000 particles have to be manually measured [106]. That being the case the particles that were counted were below that threshold and some particles were measured more than once, because of the scarcity of clearly formed particles. No automated system could be used because of uneven illumination and the almost identical shade of grey of the fCNFs and the TiO_2 nanoparticles under TEM. This made it hard using software packages such as ***ImageJ*** to resolve the fCNFs from the TiO_2 nanoparticles.

That being said, qualitative particle size distribution plots along with the mean particle sizes of the TiO_2 nanoparticles on the surface of the fCNFs as shown in **Figs 4.3.13 (a-i)**, were obtained. Based upon these measurements from left to right it was noted that the

TiO_2 particle size ranged from 4-6 nm. These plots were arranged from left to right in such a way that the effect of functionalisation, at fixed exposure times to $TiCl_4$, on the particle size of TiO_2 nanoparticles could be observed e.g. **Figs 4.3.13 (a-c)**.

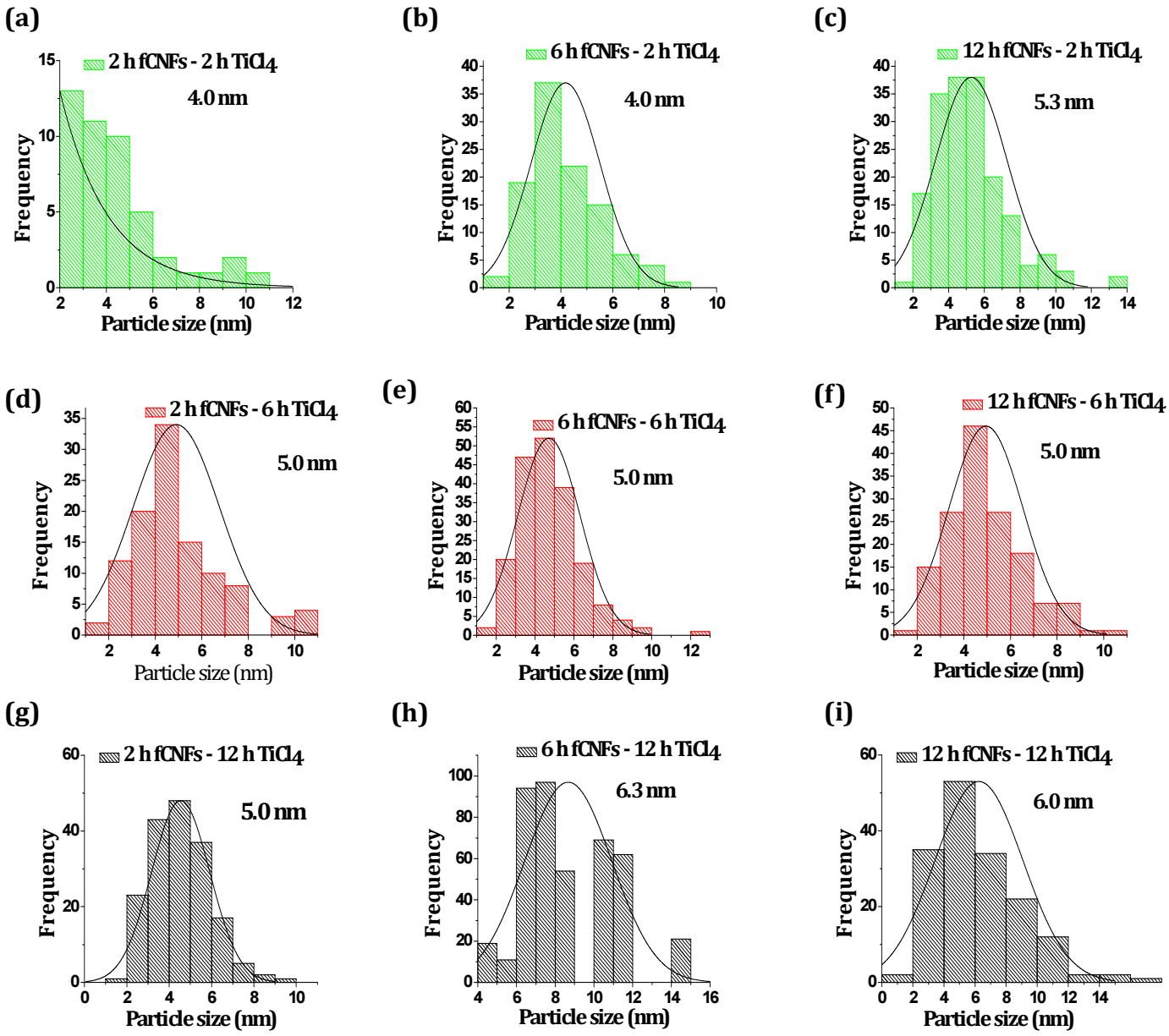

Figure 4.3.13 (a-i): Particle size distribution plots for the different CNF-TiO_2 combinations.

Similarly they were arranged from top to bottom in such a way that the effects of exposure to $TiCl_4$, at fixed functionalisation times, could also be observed e.g. **Figs 4.3.13 (a, d and g)**. It was found that, in general, when the functionalisation time was increased from 2-12 h, for any fixed duration of exposure to $TiCl_4$, the nanoparticles of TiO_2 became larger (e.g. **Figs 4.3.13 (a-c)**). In general when the duration of the

exposure to $TiCl_4$ was increased, for any fixed functionalisation time, the nanoparticles of TiO_2 also became larger (e.g. **Figs 4.3.13** (**a, d** and **g**)).

Although small variations in these trends were noted where the size of the TiO_2 nanoparticles remained constant (e.g. **Figs 4.3.13** (**d, e** and **f**)) or increased then decreased (e.g. **Figs 4.3.13** (**g, h** and **i**)), overall when the fCNFs were exposed to $TiCl_4$ for longer durations the TiO_2 nanoparticles increased in size. This is an expected result because once all the nucleation sites have been used, the particle size will grow. In addition, the TiO_2 nanoparticles increased in size when the time of functionalisation was increased. Again, this can be explained by having many seed sites close to each other and this may lead to having neighbouring particles agglomerate. These variations have indicated that the interaction between the duration of exposure to $TiCl_4$ and functionalisation time of CNFs with fly ash was more complex than originally anticipated.

In order to establish the effects of functionalisation and duration of exposure to $TiCl_4$ on the size of the TiO_2 nanoparticles that were deposited on the surface of the fCNFs, further TEM analyses were conducted.

When the TEM micrographs were assembled in such a way that the effects of functionalisation time, at fixed times of $TiCl_4$, could be visually monitored (i.e. from left to right) it was noted that the extent of surface coverage of TiO_2 increased with increased functionalisation time (e.g. **Fig 4.3.14** (**a, b** and **c**)). This observation was consistent with the increased intensity of the Ti-O-C bond which increased with functionalisation time at fixed duration of exposure to $TiCl_4$ as previously noted in **Fig 4.3.4** (**a-c**), by ATR-FTIR spectroscopy. This implied that as the functionalisation time was increased this resulted in more carbonyl groups throughout the surface of the CNFs, which in turn led to more Ti-O-C bonds which were formed and hence a greater extent of surface coverage of TiO_2 (to see high resolution images of TEM micrographs refer to **Figs 2** (**c-k**) in **Appendix II**)

However, when the TEM micrographs were assembled in such a way that the effects of duration of exposure to $TiCl_4$, at fixed functionalisation times, could be visually monitored (i.e. from top to bottom), it was noted that the surface coverage of the TiO_2

particles appeared to stay fairly constant, but that particles deposited became more agglomerated.

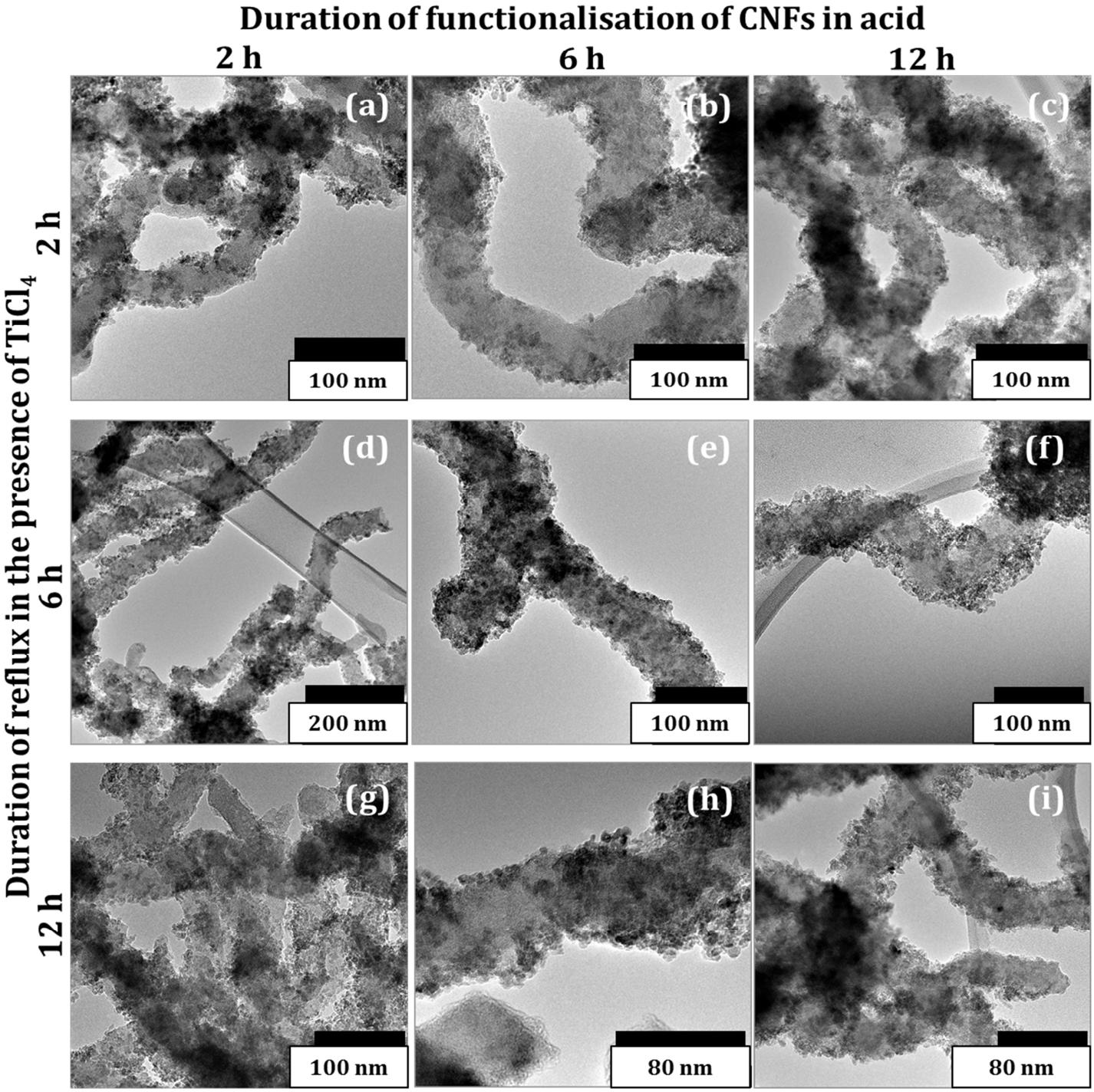

Figure 4.3.14 (a-i): TEM micrographs of CNF-TiO_2 hybrids showing the different effects of functionalisation times, ranging from 2-12 h from left to right, at fixed $TiCl_4$ exposure times i.e. (a-c), (d-e) and (g-i) and the effects of the duration of exposure to $TiCl_4$ from 2-12 h from top to bottom (a, d and g); (b, e and h) and (c, f and i).

Table 4.3.6: A tabulated summary of the average residual weight %s, particle size and the specific surface area of the different CNF-TiO_2 hybrids that were functionalised at different times for fixed durations of exposure to $TiCl_4$.

Sample number	***Sample name***	***Weight %*** (***%***)	***Particle size*** (***nm***)	***Specific surface area*** (g/m^2)
1	**2 h fCNFs - 2 h $TiCl_4$**	41	4.0	66
2	**6 h fCNFs - 2 h $TiCl_4$**	44	4.0	61
3	**12 h fCNFs - 2 h $TiCl_4$**	39	5.3	61
4	**2 h fCNFs - 6 h $TiCl_4$**	40	5.0	54
5	**6 h fCNFs - 6 h $TiCl_4$**	46	5.0	41
6	**12 h fCNFs - 6 h $TiCl_4$**	39	5.0	53
7	**2 h fCNFs - 12 h $TiCl_4$**	41	5.0	61
8	**6 h fCNFs - 12 h $TiCl_4$**	43	6.3	49
9	**12 h fCNFs - 12 h $TiCl_4$**	41	6.0	55

A summary of this data was then drawn up in **Table 4.3.6**. The TiO_2 nanoparticle size appeared to play a minimal role in the anomalous surface a trend that was observed for the CNF-TiO_2 hybrids. For instance, hybrids with TiO_2 nanoparticles which were measured to have mean particles sizes of 4.0 nm (sample 2 in **Table 4.3.6**) displayed the same surface area as those that were made from TiO_2 nanoparticles that were 5.3 nm (sample 3 in **Table 4.3.6**).

Agglomeration of TiO_2 nanoparticles appeared to play a marginal role in the anomalous surface area trend that was observed for the CNF-TiO_2 hybrids. For instance, the hybrids which showed the greatest agglomeration (i.e. samples 7, 8 and 9) had surface areas which on average only slightly differed from those which showed the least agglomeration (samples 1, 2 and 3).

The extent of coverage of TiO_2 nanoparticles on the fCNFs appeared to also play a marginal role in the surface area trend as well. Here the hybrids which had the highest surface coverage, due to prolonged surface functionalisation, had only slightly lower surface areas than those which had the lowest surface coverage (e.g. sample 3 vs sample 1 or sample 4 vs sample 6).

The residual weight % that was left after the combustion of each CNF-TiO_2 hybrid, appeared to play a more significant role in the anomalous surface area trend that was

observed previously. Here the hybrids which had the highest residual weight % after combustion in the TGA, typically had the lowest surface areas (e.g. samples 5 and 8). Since the same loading of TiO_2 was applied to all the fCNFs (i.e. 10% m/m), assuming that all of the samples had the same amount of TiO_2 bound or unbound, the variance in the residual masses was assumed to be due to fly ash.

Additional information on the nature of the physical properties of the CNFs was obtained from TEM. From the previous chapters, the actual structural arrangement of carbon atoms in the CNFs was a matter of speculation. The circled areas labelled **i** and **ii** in **Figs 4.3.15** (**a** and **b**) show a conical-shaped end and an inverse-cone-shaped hole, respectively. This suggested that the CNFs were fish-bone structured (cup-stacked) as imaged by Sato *et al.* in **Fig 4.3.15 (c)** [105].

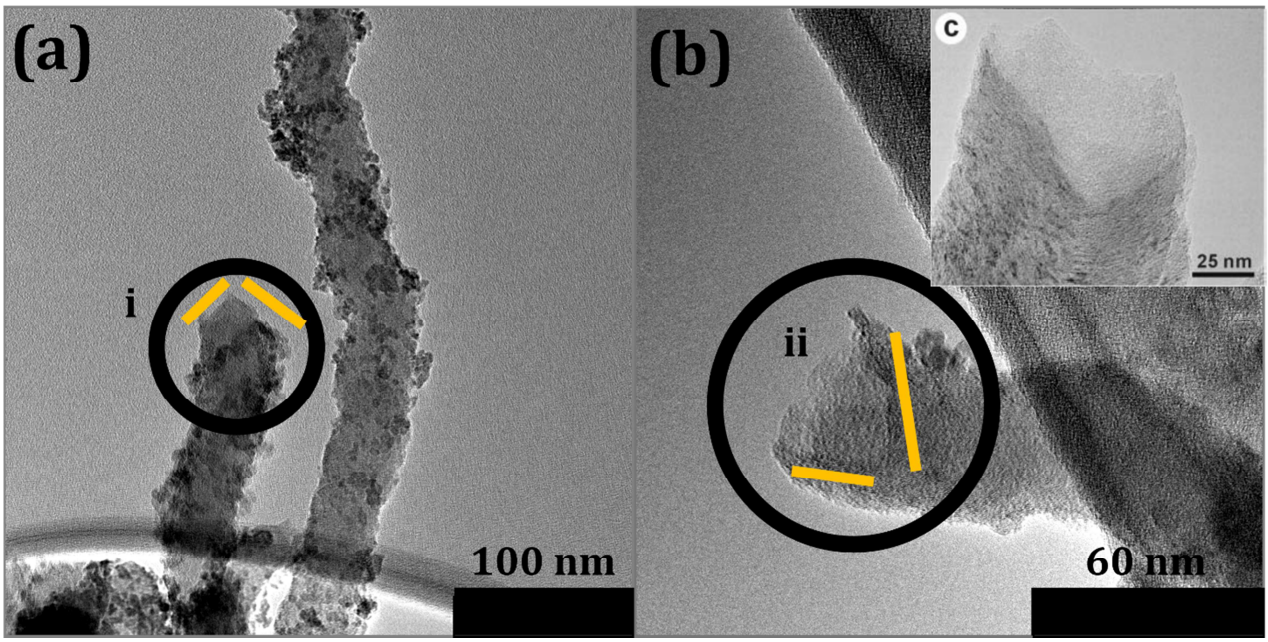

Fig 4.3.15: (a) a cone-shaped end on a CNF in the 2h fCNF-6 h $TiCl_4$ hybrid (i) and (b) an inverse cone-shaped hole on a CNF in a 2 h CNF- 12 h $TiCl_4$ hybrid (ii).

Furthermore, TEM of the CNF-TiO_2 hybrids revealed more supporting data with regards to the growth of the CNFs via tip growth. **Fig 4.3.16** (**a**) shows a 2 h fCNF- 12 h $TiCl_4$ hybrid tip with a particle stuck on it. A high magnification image of the tip (**Fig 4.3.16** (**b**)), showed that the particle may have been responsible for the growth of the CNFs via tip growth. Close inspection of this image showed lattice fringes of carbon around it. The particle is tapered and reflects the cone structure typical of the breaking patterns of the CNFs.

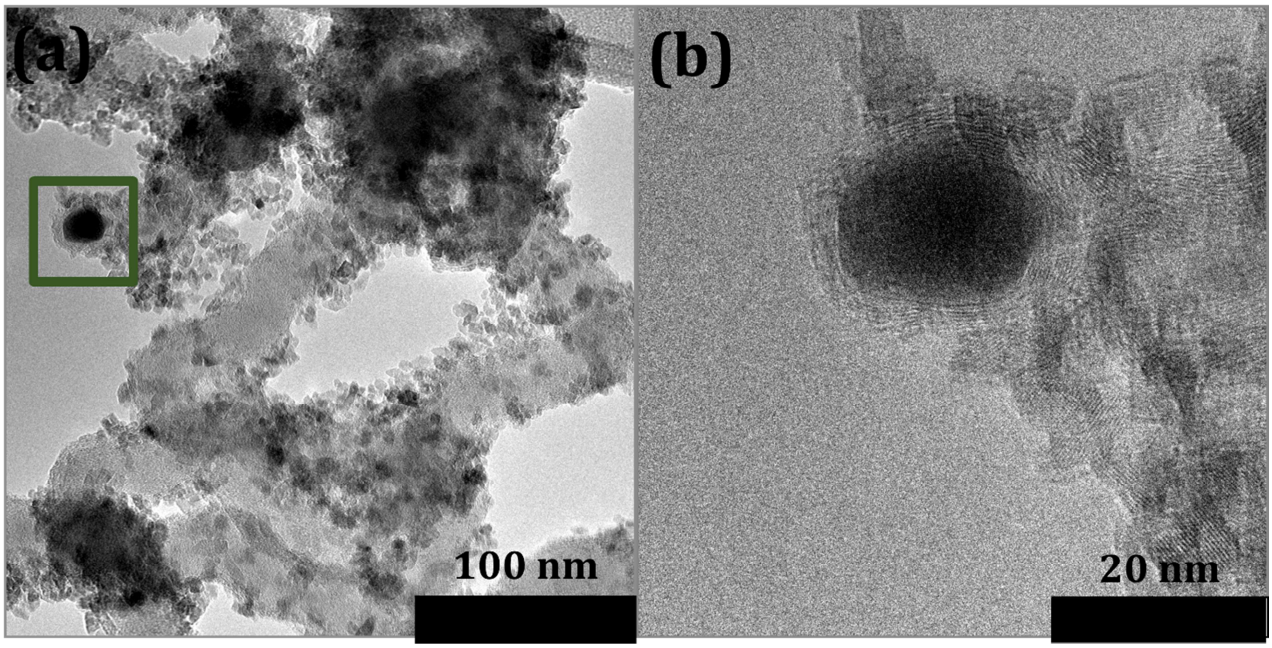

Figure 4.3.16: A 2 h fCNF- 12 h $TiCl_4$ hybrid TEM micrograph showing a particle stuck on the tip of the hybrid and, (b) a high magnification micrograph of the image showing carbon lattice fringes around the particle.

Some of the high magnification images of the CNF-TiO_2 hybrids also showed possible epitaxial relations between the fCNFs and the TiO_2 nanoparticles (**Fig 4.3.17** (**a**, **b** and **c**)). The magnified region in **Fig 4.3.17** (**a**) is shown in **Fig 4.3.17** (**b**) and **Fig 4.3.17** (**c**) is its colour filtered image. The lattice fringes of the anatase nanoparticles seemed aligned with those of the fCNFs as indicated by the blue parallel lines in the filtered image (**Fig 4.3.17** (**c**)). This suggested that the fCNFs and the TiO_2 particles may have a chemical interaction.

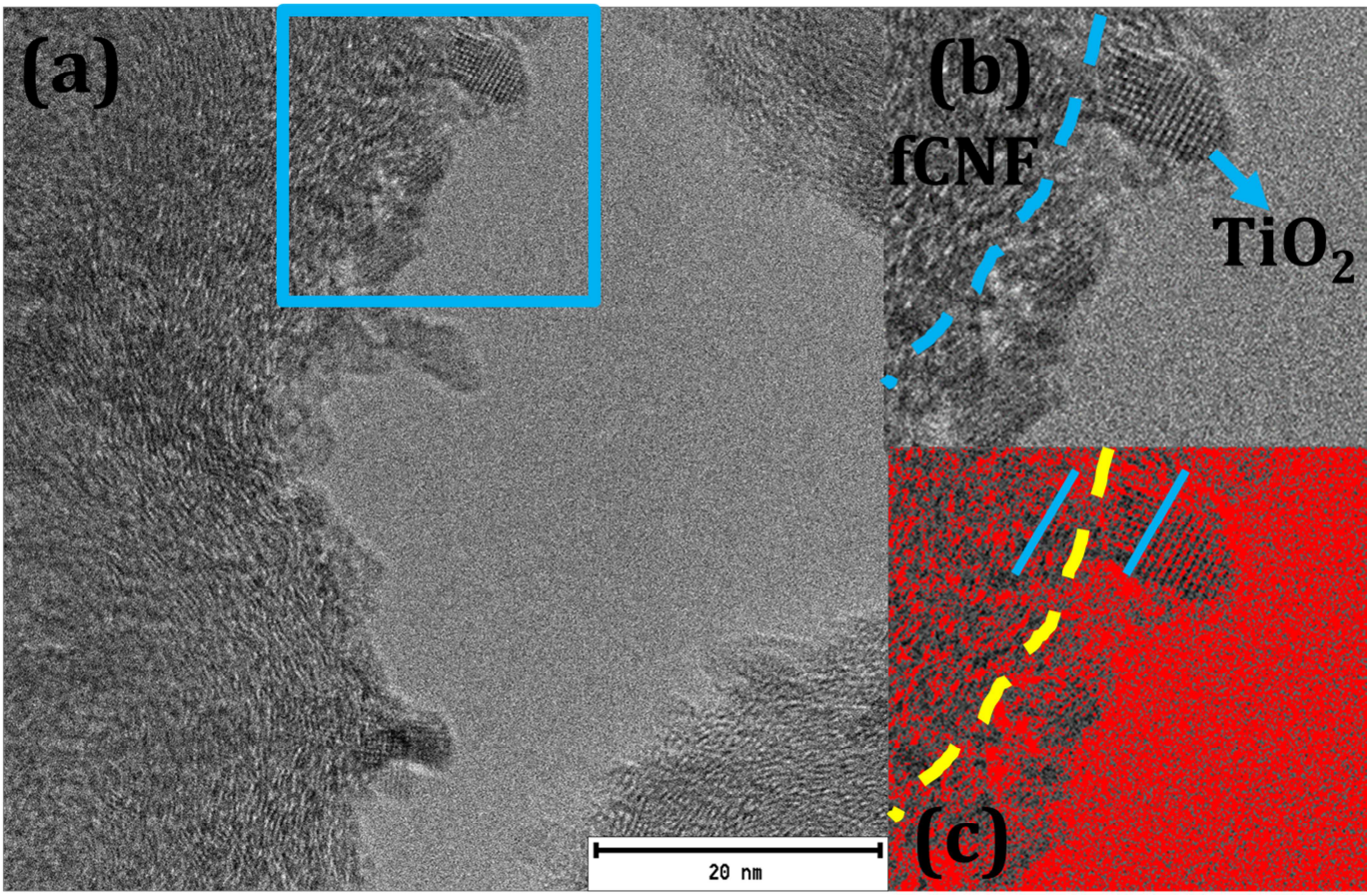

Figure 4.3.17: (a) TEM micrographs of a 6 h fCNF- 2 h $TiCl_4$ hybrid showing carbon and anatase lattice fringes, (b) the zoomed in section of the micrograph showing the TiO_2 and CNF boundary and, (c) a filtered colour image of the zoomed section showing the alignment of the lattice fringes.

Although information such as strain within the TiO_2 nanoparticles could not be observed, high resolution transmission electron microscopy (HRTEM) could be used to validate the suggestion. Given all the above observations, the formation mechanism of pristine anatase nanoparticles on the fCNFs could be postulated as suggested by Franklyn [107]. The work that Franklyn performed indicated that the presence of an organic acid in a $TiCl_4$ and water solution produced anatase nanoparticles only.

Primarily, it was determined that the C=O group of the organic acid moiety hybridised in the presence of the Ti(IV) ions. These ions are oxyphilic so they would draw the negative charge on themselves, this allows for the formation of the Ti-O-C bond. The kinetic differentiation mechanism was proposed to be the main method responsible for the formation of anatase over rutile.

This method involved the formation of anatase nanoparticles resulting from the dehydration of hydroxylated Ti(IV) ions, under the protection of C=O groups in solution, thus helping to control the size. The stability of the anatase nanoparticles depended on their critical particle size (~14 nm) before they would convert to rutile. In this study the particles were below 10 nm and it is possible that the same processes took place in their formation, but this would require further investigation.

Conclusions

The aim of this part of the study was to synthesise an optimal CNF-TiO_2 hybrid that has potential applications as a support for catalysts or as a photocatalyst itself. The study was concerned with establishing the effects of functionalisation time and the duration of exposure to $TiCl_4$ on the fCNFs and on the dispersion of the TiO_2 nanoparticles on their surfaces, their size distributions as well as their physical properties. One of the major objectives was to determine the type of interaction between the fCNFs and the TiO_2, with the intention of verifying if a covalent Ti-O-C bond had been formed.

Laser Raman spectroscopy, ATR-FTIR spectroscopy, PXRD, BET surface area analysis, TGA and TEM studies were all performed on these materials in accordance with trying to establish the above aims and objectives.

Laser Raman spectroscopy confirmed the presence of carbon and titania nanoparticles in the hybrid. In the case of the latter, the only phase of titania detected throughout all the studies on functionalisation time and duration of exposure to $TiCl_4$ was anatase. ATR-FTIR spectroscopy revealed a number of things. Firstly, evidence from the spectra alluded to the presence of fly ash in the hybrid, due to the presence of Si-O vibrational bands that were detected. Similarly the spectra obtained provisionally verified the presence of the Ti-O-C bond, despite the apparent lack of data in the literature concerned with the study of this bond on carbon nanomaterial-TiO_2 hybrids. This data also showed that the Ti-O-C bond increased as a function of increasing duration of exposure to $TiCl_4$ and functionalisation, but more so, the former. PXRD analyses confirmed that the titania particles were crystalline anatase and that carbon was present in the hybrid. PXRD also revealed the presence of other phases in the hybrid which belonged to fly ash entrapped in the hybrid including: mullite, silica and haematite. Data obtained by TGA showed that roughly on average more than 30% of fly

ash remained in the CNF-TiO_2 hybrid after all the chemical treatments that led to it synthesis.

Micrographs obtained by TEM visually revealed the effects of functionalisation time and the duration of exposure to $TiCl_4$ on the resulting hybrids. Here it was observed that in general as the functionalisation time was increased both the TiO_2 particle size and the extent of surface coverage of the CNFs increased. The increase in surface coverage of TiO_2 nanoparticles was assigned to the increase in surface C=O functional groups that were formed during functionalisation, as attested to by ATR-FTIR spectroscopy, which were believed to result in more Ti-O-C bonds. Although TiO_2 particles sizes were observed to have increased with increased exposure to $TiCl_4$, at fixed functionalisation times, surface coverage appeared to remain fairly constant. However, agglomeration of the TiO_2 nanoparticles became evident at higher durations of exposure to $TiCl_4$. This was believed to have occurred when new layers of TiO_2 nanoparticles were deposited on underlying TiO_2 nanoparticles that were already bound to the surfaces of the fCNFs. All of these factors i.e. TiO_2 nanoparticle size, extent of surface coverage and agglomeration were suspected to have played a role when BET surface area analyses were performed. Here, however, it was found that while TiO_2 nanoparticle size, extent of surface coverage of TiO_2 and agglomeration played small roles in the variation of the surface area, the residual weight %s and in the CNF-TiO_2 hybrids appeared to play the biggest role.

Furthermore, TEM revealed that the CNFs that were produced in this study had a cup-stack arrangement. It also revealed that there is a possibility of epitaxy between the fCNFs and TiO_2 nanoparticles, because their lattice fringes were parallel to each other. This observation if verified using HRTEM would validate, conclusively, the fact that the fCNFs and TiO_2 are bonded chemically. In addition to this, the possible reaction mechanism for the formation of pristine anatase was postulated to be the kinetic differentiation.

Therefore, based upon all the data obtained in the various techniques, it could be concluded that CNF-TiO_2 hybrids had been successfully synthesised, and that this was most likely due to the Ti-O-C bond on the surface of CNFs synthesised from CFA, after functionalisation in a 3:1 v/v mixture of HNO_3:H_2SO_4.

References

[1] BP, “BP Statistical review of world energy,” London, 2013.

[2] W. E. Council, “World Energy Resources”.

[3] ESKOM Holdings, Generation Communication, “Ash management in Eskom,” 2014. [Online] Available: http://www.eskom.co.za/AboutElectricity/FactsFigures/Documents/CO0004AshManagementRev10.pdf. [Accessed 27 October 2014].

[4] M. Ahmaruzzaman, “A review on the utilization of fly ash,” *Progress in Energy and Combustion Science*, vol. 36, pp. 327-363, 2010.

[5] G. Fisher, B. A. Prentice, D. Silberman, J. Ondove, A. Bierman, R. C. Ragaini and A. McFarland, “Physical and Morphological Studies of Size-Classified Coal Fly ash,” *American Chemical Society*, vol. 12, no. 4, pp. 447- 451, 1978.

[6] M. Frias and M. I. Sanchez de Rojas, “Microstructural alterations in fly ash mortars: study on the phenomena affecting particle and pore size,” *Cement and Concrete Research*, vol. 27, no. 4, pp. 619-628, January 1997.

[7] R. S. Iyer and J. Scott, “Power Station Fly ash- a review of the value-added utilization outside of the construction industry,” *Resources, Conservation and Recycling*, pp. 217-228, 2001.

[8] X. Querol, N. Moreno, J. Umana, A. Alastuey, E. Hernandez, Lopez-Soler and F. Plana, “Synthesis of zeolites from coal fly ash: an overview,” *International Journal of Coal Geology*, vol. 50, pp. 413-423, 30 January 2002.

[9] W. Chunfeng, L. Jiansheng, S. Xia, W. Lianjun and S. Xiuyun, “Evaluation of zeolites synthesised from fly ash as potential adsorbents for wastewater containing heavy metals,” *Journal of Environmental Sciences*, vol. 21, pp. 127- 136, 2009.

[10] V. Pandey and N. Singh, “Impact of fly ash incorporation in soil systems,” *Agriculture, Ecosystems and Environment*, no. 136, pp. 16-27, 2010.

[11] C. XiaoYan, K. Wendell, J. Zhu, L. JiangLi, Y. Xianxian and Z. Zhijian, "Synthesis of nano-zeolite from coal fly ash and its potential for nutrient sequestration from anaerobically digested swine wastewater," *Bioresource Technology*, no. 110, pp. 79-85 , 2012.

[12] R. H. Matjie, J. R. Bunt and J. H. P. van Heerden, "Extraction of alumina from coal fly ash generated from a selected low rank bituminous South African coal," *Minerals Engineering*, no. 18, pp. 299-310, 2005.

[13] S. Wang, "Application of Solid Ash based Catalyst in Heterogeneous Catalysis," *Environmental Science Technology*, no. 42, pp. 7055-7063, 2008.

[14] O. M. Dunens, K. Mackenzie and A. T. Harris, "Synthesis of multi-walled carbon nanotubes on fly ash derived catalysis," *Environmental Science Technology*, no. 43, pp. 7889-7894, 2009.

[15] D. C. Nath and V. Sahajwalla, "Application of fly ash as a catalyst for the synthesis of carbon nanotube ribbons," *Journal of Hazardous Materials*, no. 192, pp. 691-697, 2011.

[16] A. Yasui, Y. Kamiya, S. Sugiyama, S. Ono, H. Noda and Y. Ichikawa, "Synthesis of carbon nanotubes on fly ashes by chemical vapour deposition processing," *IEEJ Transactions on Electrical and Electronic Engineering*, vol. 4, pp. 787-789, 2009.

[17] N. Salah, S. S. Habib, Z. H. Khan, A. Memic and M. N. Nahas, "Growth of carbon nanotubes on catalysts obtained from carbon rich fly ash," *Digest Journal of Nanomaterials and Biostructures*, vol. 7, no. 3, pp. 1279-1288, September 2012.

[18] N. Salah, A. A. Alghamdi, A. Memic, S. S. Habib and Z. H. Khan, "Formation of carbon nanotubes from carbon rich fly ash: growth parameters and mechanism," *Materials and Manufacturing Processes*, pp. 1-19, 2015.

[19] N. Hintsho, A. Shaikjee, H. Masenda, D. Naidoo, D. Billing, P. Franklyn and S. Durbach, "Direct synthesis of carbon nanofibers from South African coal fly ash," *Nanoscale Research Letters*, vol. 9, no. 387, pp. 1-11, 2014.

[20] K. B. K. Teo, C. Singh, M. Chhowalla and W. I. Milne, “Catalytic synthesis of carbon nanotubes and nanofibers,” in *Encyclopedia of Nanoscience and Nanotechnology*, vol. 10, H. S. Nalwa, Ed., American Scientific Publishers, 2003, pp. 1-22.

[21] J. Prasek, J. Drbohlavova, J. Chomoucka, J. Hubalek, O. Jasek, V. Adam and R. Kizek, “Methods for carbon nanotubes synthesis- review,” *Journal of Materials Chemistry*, vol. 21, pp. 15872-15884, 2011.

[22] A. Chatterjee and B. L. Deopura, “Carbon nanotubes and nanofibre: an overview,” *Fibers and Polymers*, vol. 3, no. 4, pp. 134-139, 2002.

[23] R. T. K. Baker, “Catalytic growth of carbon filaments,” *Carbon*, vol. 3, no. 27, pp. 315- 323, 1989.

[24] N. M. Rodriguez, “A review of the catalytically grown carbon nanofibers,” *The Journal of Materials Research*, vol. 8, no. 12, pp. 3233-3250, 1993.

[25] S. Mori and M. Suzuki, “Non-catalytic, low-temperature synthesis of carbon nanofibers by plasma-enhanced chemical vapour deposition,” in Nanofibers, A. Kumar, Ed., Intech, 2010, pp. 297-308.

[26] Q. Liu, V. Barron, j. Torrent, H. Qin and Y. Yu, “The magnetism of micro-sized hematite explained,” *Physics of the Earth and Planetary Interiors*, vol. 183, pp. 387-397, March 2010.

[27] K. Saranya, A. Subramania and N. Sivasankar, “Influence of earth-abundant bimetallic (Fe–Ni) nanoparticle-embedded CNFs as a low-cost counter electrode material for dye-sensitized solar cells,” *Royal Society of Chemistry Advances*, vol. 5, pp. 43611-43619, March 2015.

[28] K. S. W. Sing, D. H. Everett, R. A. W. Haul, L. Moscou, R. A. Pierotti, J. Rouquerol and T. Siemieniewska, “Reporting physisorption data for gas/solid systems with special reference to the determination of surface area and porosity,” *Pure and Applied Chemistry*, vol. 57, no. 4, pp. 603-619, 1985.

[29] Allwar, "Characteristics of micro- and mesoporous structure and surface chemistry of activated carbons produced by oil palm shell," in *International conference on Chemical, Ecology and Environmental Sciences* (ICEES 2012), Bangkok, 2012.

[30] R. Blissett and N. Rowson, "A review of the multi-component utilisation of coal fly ash," *Fuel*, vol. 97, pp. 1-23, 2012.

[31] P. Ghosh, T. G. K. Soga, T. Jimbo, R. Katoh, K. Sumiyama and Y. Ando, "Effect of sulphur concentration on the morphology of carbon nanofibers produced from a botanical hydrocarbon," *Nanoscale Research Letters*, vol. 3, pp. 242-248, 11 March 2008.

[32] P.-C. Ma, N. A. Siddiqui, G. Marom and J.-K. Kim, "Dispersion and functionalisation of carbon nanotubes for polymer-based nanocomposites: A review," *Composites: Part A*, no. 41, pp. 1345-1367, 2010.

[33] K. P. De Jong and J. W. Geus, "Carbon nanofibers: catalytic synthesis and applications," *Catalysis Reviews: Science and Engineering*, vol. 42, no. 4, pp. 481-510, 2000.

[34] A. Guedes, B. Valentim, A. Prieto, A. Sanz, D. Flores and F. Noronha, "Characterization of fly ash from a power plant and surroundings by micro-Raman spectroscopy," *Coal Geoloy*, vol. 73, pp. 359-370, 2008.

[35] E. Rokhina, M. Lahtinen, K. Makarov, V. Jegatheesan and Virkutyte, "Theoretical and practical aspects of chemical functionalization of carbon nanofibers (CNFs); DFT calculations and adsorption studies," *Bioresource Technology*, vol. 113, pp. 127-131, 2012.

[36] J. Sun, M. Iwasa, L. Gao and Q. Zhang, "Single-walled carbon nanotubes coated with titania nanoparticles," *Carbon*, vol. 42, pp. 885-901, 2004.

[37] R. Yudianti, H. Onggo, Sudirman, Y. Saito, T. Iwata and J. Azuma, "Analysis of functional group sited on multi-wall carbon nanotube surface," *The Open Material Science Journal*, vol. 5, pp. 242-247, 2011.

[38] M. Srivastava, S. Chaubey and A. Ojha, "Investigation on size dependent structural and magnetic behavior of nickel ferrite nanoparticles prepared by sol-gel and hydrothermal methods," *Materials Chemistry and Physics*, no. 118, pp. 174-180, 2009.

[39] A. Micoli, "Functionalization of carbon nanotubes for construction of supramolecular nanostructured materials," Trieste, 2012.

[40] F. B. Bonalume. C, W. G. Lebrao and L. J. Rossi, "Functionalized carbon nanotubes for nanocomposites," in ICCS16 (16th *International Conference on Composite Structures*), Porto, 2011.

[41] V. Mittal, "Carbon nanotubes surface modifications: an overview," in Surface Modification of Nanotube Fillers, V. Mittal, Ed., Weinheim, Wiley-VHC Verlag GmbH& Co. KGaA, 2011, pp. 1-24.

[42] C. Ramirez-Castro, O. Crosnier, L. Athouel, R. Retoux, D. Belanger and T. Brousse, "Electrochemical performance of carbon/MnO_2 nanocomposites prepared via molecular bridging supercapacitor electrode materials," *Journal of the Electrochemical Society*, vol. 162, no. 5, pp. A5179-A5184, January 2015.

[43] J. Stevens, A. Y. Huang, H. Peng, I. W. Chiang, V. N. Khabashesku and J. L. Margrave, "Sidewall amino-functionalization of single-wall carbon nanotubes through fluorination and subsequent reactions with terminal diamines," *Nanoletters*, vol. 3, no. 3, pp. 331-336, 2003.

[44] M. Holzinger, J. Steinmetz, D. Samaille, M. Glerup, M. Paillet, P. Bernier, L. Ley and R. Graupner, "[1+2] Cycloaddition for cross-linking SWCNTs," *Carbon*, vol. 42, pp. 941-947, 2004.

[45] S. K. Kim, D. J. Bae, R. J. Kim, K. A. Park, S. Chu, C. Lim, J.-J. Kim, W. B. Choi, C. Y. Park and Y. H. Lee, "Modification of electronic structures of a carbon nanotube by hydrogen functionalization," *Advanced Materials*, vol. 14, no. 24, pp. 1818-1821, 2002.

[46] S. Aryal, K. C. Kim, K. K. Kim, S. M. Khil and H. Y. Kim, "Multiwalled carbon nanotubes/TiO_2 composite nanofibre by electrospinning," *Materials Science and Engineering C*, vol. 28, pp. 75-79, 2008.

[47] H. Chen, S. Yang, K. Yu, Y. Ju and C. Sun, "Effective photocatalytic degradation of atrazine over titania-coated carbon nanotubes (CNTs) coupled with microwave energy," *The Journal of Physical Chemistry A*, vol. 115, pp. 3034-3041, 2011.

[48] S. Santangelo, G. Messina, G. Faggio, S. Abdul Rahim and C. Milone, "Effect of sulphuric-nitric acid mixture composition on the surface chemistry and structural evolution of liquid-phase oxidised carbon nanotubes," Journal of Raman Spectroscopy, vol. 43, pp. 1432-1442, 2012.

[49] I. Capek, "Dispersions based on carbon nanotubes- biomolecules conjugate," in Carbon nanotubes- Growth and Applications, M. Naraghi, Ed., Rijeka, InTech, 2011, pp. 74-96.

[50] A. Hirsch, "Functionalization of single-walled carbon nanotubes," *Angewandte Chemie, International Edition*, vol. 41, no. 11, pp. 1853-1859, 2002.

[51] P. Lei, F. Wang, S. Zhang, Y. Ding, J. Zhao and M. Yang, "Conjugation-grafted-TiO_2 nanohybrid for high photocatalytic efficiency under visible light," Applied *Materials and Interfaces*, vol. 6, pp. 2370-2378, 2014.

[52] B. Su, X. Liu, X. Peng, T. Xiao and Z. Su, "Preparation and characterisation of TiO/polymer complex nanomaterial," *Materials Science & Engineering A*, vol. 349, pp. 59-62, 2003.

[53] B. Su, Z. Ma, S. Min, S. She and Z. Wang, "Preparation of TiO_2/PS complex nanoparticles," *Materials Science & Engineering A*, vol. 458, pp. 44-47, 2007.

[54] S. X. Min, F. Wang, L. Feng, C. Y. Tong and Z. R. Yang, "Synthesis and photocatalytic activity of TiO_2/conjugated polymer complex nanoparticles," *Chinese Chemical Letters*, vol. 19, pp. 742-746, 2008.

[55] P. Lei, F. Wang, X. Gao, Y. Ding, S. Zhang, J. Zhao, S. Liu and M. Yang, "Immobilization of TiO_2 nanoparticles in polymeric substrates by chemical bonding for multi-cycle photodegradation of organic pollutants," *Journal of Hazardous Materials*, Vols. 227-228, pp. 185-194, 2012.

[56] M. N. Tchoul, W. T. Ford, G. Lolli, D. E. Resasco and S. Arepalli, "Effect of mild nitric acid oxidation on dispersability, size, and structure of single-walled carbon nanotubes," *Chemistry of Materials*, vol. 19, no. 23, pp. 5765-5772, 2007.

[57] V. M. Naseh, A. A. Khodadadi, Y. Mortazavi, A. O. Sahraei, F. Pourfayaz and M. S. Sedghi, "Functionalisation of carbon nanotubes using nitric acid oxidation and DBD plasma," *World Academy of Science, Engineering and Technology*, vol. 3, no. 1, pp. 134-136, 2009.

[58] K. K. Shivpuri, L. B, A. D. Kulkarni and A. K. Dikshit, "Metal leaching potential in coal fly ash," *American Journal of Environmental Engineering*, vol. 1, no. 1, pp. 21-27, 2011.

[59] L. M. Toebes, J. M. P. Van Heeswijk, J. H. Bitter, A. J. Van Dillen and K. P. De Jong, "The influence of oxidation on the texture and the number of oxygen-containing surface groups of carbon nanofibers," *Carbon*, vol. 42, no. 2, p. 307–315, 2004.

[60] E. M. Birch, T. Ruda-Eberenz, M. A. R. Chai and R. L. Hatfiled, "Properties that influence the specific surface areas of carbon nanotubes and nanofibers," *Oxford Journals: Annals of Occupational Hygiene*, vol. 57, no. 9, p. 1148–1166, June 2013.

[61] T. Hemraj-Benny, J. T. Bandosz and S. S. Wong, "Effect of ozonolysis on the pore structure, surface chemistry, and bundling of single-walled carbon nanotubes," *Journal of Colloid and Interface Science*, vol. 317, no. 2, pp. 375-382, January 2008.

[62] J. Zhang, I. Khatri, N. Kishi, T. Soga and T. Jimbo, "Synthesis of carbon nanofibers from carbon particles by ultrasonic spray pyrolysis of ethanol," *IEICE Transactions on Electronics*, Vols. E92-C, no. 12, pp. 1432-1437, 2009.

[63] J. Li, J. M. Vergne, D. E. Mowles, W.-H. Zhong, M. D. Hercules and M. C. Lukehart, "Surface functionalization and characterization of graphitic carbon nanofibers (GCNFs)," *Carbon*, vol. 43, no. 14, pp. 2883-2893, 2005.

[64] A. Fujishima and K. Honda, "Electrochemical photolysis of water at a semiconductor electrode," *Nature*, vol. 238, pp. 8-37, 1972.

[65] R. Leary and A. Westwood, "Carbonaceous nanomaterials for the enhancement of TiO_2 photocatalysis," *Carbon*, vol. 49, pp. 741- 772, 2011.

[66] M. Landmann, E. Rauls and W. Schmidt, "The electronic structure and optical response of rutile, anatase and brookite TiO_2," *Journal of Physics : Condensed Matter*, vol. 24, pp. 1-6, 2012.

[67] S. Lee, "Photocatalytic nanocomposites based on TiO_2 and carbon nanotubes," Florida, 2004.

[68] H. Tang, K. Prasad, R. Sanjines, P. Schmid and F. Levy, "Electrical and optical properties of TiO_2 anatase thin films," *Journal of Applied Physics*, vol. 75, pp. 2042-2047, 1994.

[69] G. Lu and X. Zhao, "Nanoporous materials - An Overview," *Nanoporous materials-Science and Engineering*, pp. 1-12, 2004.

[70] Y. Yu, C. J. Yu, J. G. Yu, Y. C. Kwok, Y. K. Che, J. C. D. L. Zhao, W. K. Ge and P. K. Wong, "Enhancement of photocatalytic activity of mesoporous TiO_2 by using carbon nanotubes," *Applied Catalysis A: General*, vol. 289, pp. 186-196, 2005.

[71] H. Y. Ng, I. V. Lightcap, K. Goodwin, M. Matsumura and P. V. Kamat, "To what extent do graphene scaffolds Improve the photovoltaic and photocatalytic response of TiO_2 nanostructured films?," *Journal of Physical Chemistry Letters*, vol. 1, pp. 2222-2227, 2010.

[72] A. Jitianu, T. Cacciaguerra, M. Berger, R. Benoit, F. Beguin and S. Bonnamy, "New carbon multiwall nanotubes – TiO_2 nanocomposites obtained by the sol-gel method," *Journal of Non-Crystalline Solids*, vol. 345 & 346, pp. 596-600, 2004.

[73] C. S. Gomes da Silva, "Synthesis, spectroscopy and characterisation of titanium dioxide based photocatalysts for the degenarative oxidation of organic pollutants," Porto, 2008.

[74] W. Wang, P. Serp, P. Kalck and J. L. Faria, "Visible light photodegradation of phenol on MWNT-TiO_2 composite catalysts prepared by a modified sol-gel method," *Journal of Molecular Catalysis A; Chemical*, vol. 235, pp. 194-199, 2005.

[75] A. Brioude, P. Vincent, C. Journet, J. Plenet and S. Purcell, "Synthesis of sheathed carbon nanotube tips by sol-gel technique," *Applied Surface Science* , vol. 221, pp. 4-9, 2004.

[76] A. Jitianu, T. Cacciaguerra, R. Benoit, S. Delpeux, F. Beguin and S. Bonnamy, "Synthesis and characterisation of carbon nanotubes-TiO_2 nanocomposites," *Carbon*, vol. 42, pp. 1147-1151, 2004.

[77] P. Vincent, A. Brioude, C. Journet, S. Rabaste, S. Purcell, J. Le Brusq and J. Plenet, "Inclusion of carbon nanotubes in a TiO_2 sol-gel matrix," *Journal of Non-Crystalline Solids*, vol. 311, pp. 130-137, 2002.

[78] B. Gao, G. Z. Chen and G. Puma Li, "Carbon nanotubes/titanium dioxide ($CNTs/TiO_2$) nanocomposites prepared by conventional and novel surfactant wrapping sol-gel methods exhibiting enhanced photocatalytic activity," *Applied Catalysis B; Environmental*, vol. 89, pp. 503-509, 2009.

[79] T. Sugimoto, X. Zhou and A. Muramatsu, "Synthesis of uniform anatase TiO_2 nanoparticles by sol-gel method 4. Shape control," *Journal of Colloid and Interface Science* , vol. 259, pp. 53-61, 2003.

[80] K. Woan, G. Pyrgiotakis and W. Sigmund, "Photocatalytic carbon-nanotube- TiO_2 composites," *Advanced Materials*, vol. 21, pp. 2233-2239, 2009.

[81] K. Byrappa, A. Dayananda, Sajan, C.P, B. Bavasalingu, M. Shayan and M. Yoshimura, "Hydrothermal preparation of ZnO:CNT and TiO_2:CNT composites and their photocatalytic applications," *Journal of Material Sciences*, vol. 43, pp. 2348-2355, 2008.

[82] A. Yoshimura and K. Byrappa, "Hydrothermal processing of materials: past, present and future," *Journal of Materials Sciences*, vol. 43, pp. 2085-2103, 2008.

[83] K. Byrappa, "Novel hydrothermal solution routes of advanced high melting nanomaterials processing," *Journal of the Ceramic Society of Japan*, vol. 117, no. 3, pp. 236-244, 2009.

[84] Y. Yan, J. Lu, C. Deng, Zhang and Xiangmin, "Facile synthesis of titania nanoparticles coated carbon nanotubes for selective enrichment of phosphopeptides for mass spectrometry analysis," *Talanta*, vol. 107, pp. 30-35, 2013.

[85] Y. Hu and C. Guo, "Carbon nanotubes and carbon nanotubes/metal oxide heterostructures: synthesis, characterization and electrochemical property," in Nanotechnology and Nanomaterials; Carbon Nanotubes- Growth and Applications, M. Naraghi, Ed., Croatia, InTech Open Access Pulisher, 2011, pp. 3-35.

[86] Q. Wang, D. Yang, D. Chen, Y. Wang and Z. Jiang, "Synthesis of anatase titania-carbon nanotubes nanocomposites with enhanced photocatalytic activity through a nanocoating-hydrothermal process," *Journal of Nanoparticle Research*, vol. 9, pp. 1087-1096, 2007.

[87] B. Liu and H. Zeng Chun, "Carbon nanotubes supported mesoporous mesocrystals of anatase TiO_2," *Chemical Materials*, vol. 20, pp. 2711-2718, 2008.

[88] S. Abbasi, S. M. Zebarjad and S. H. N. Baghban, "Decorating and filling of multi-walled carbon nanotubes with TiO_2 nanoparticles via wet chemical method," *Engineering*, vol. 5, pp. 207- 212, 2013.

[89] M. Ouzzine, M. Lillo Rodenas and A. Linares Solano, "Carbon nanofibres as substrates for the preparation of TiO_2 nanostructured photocatalysts," *Applied Catalysis B: Environmental*, vol. 127, pp. 291-299, 2012.

[90] X. H. Xia, Z. J. Jia, Y. Yu, Y. Liang, Z. Wang and L. L. Ma, "Preparation of multi-walled carbon nanotube supported TiO_2 and its photocatalytic activity in the reduction of CO_2 with H_2O," *Carbon*, vol. 45, pp. 717-721, 2007.

[91] D. Segal, "Chemical synthesis of ceramic materials," *Journal of Materials Chemistry*, vol. 7, no. 8, pp. 1297-1305, 1997.

[92] P. J. Franklyn, D. C. Levendis, N. J. Coville and M. Maaza, "Phase transformation of hydrothermally synthesized nanoparticle TiO_2: from anatase to rutile nanorods," *South African Journal of Chemistry*, vol. 60, pp. 71-75, 2007.

[93] G. Hu, X. Meng, X. Feng, Y. Ding, S. Zhang and M. Yang, "Anatase TiO_2 nanoparticles/carbon nanotubes nanofibers: preparation, characterization and photocatalytic properties," *Journal Material Science*, vol. 42, pp. 7162-7170, 2007.

[94] W. Fan, L. Gao and J. Sun, "Anatase TiO_2- coated multi-wall carbon nanotubes with the vapour phase method," *Journal of the American Ceramic Society*, vol. 2, no. 89, pp. 731-733, 2006.

[95] S. Shanmugam and A. Gedanken, "Carbon- coated anatase TiO_2 nanocomposite as a high-performance electrocatalyst support," *Small*, vol. 3, no. 7, pp. 1189-1193, 2007.

[96] S. Yu, J. H. Yun, Y. H. Kim and J. Yi, "Carbon-doped TiO_2 nanoparticles wrapped with nanographene as a high performance photocatalyst for phenol degradation under visible light irradiation," *Applied Catalysis B: Environmental*, vol. 144, pp. 893-899, 2014.

[97] S. Kedem, J. Schmidt, Y. Paz and Y. Cohen, "Composite polymer nanofibers with carbon nanotubes and titanium dioxide particles," *Langmuir*, vol. 21, pp. 5600-5604, 2005.

[98] B. Ahmmad, Y. Kusumoto, S. Somekawa and M. Ikeda, "Carbon nanotubes synergistically enhance photocatalytic activity of TiO_2," *Catalysis Communications*, vol. 9, pp. 1410-1413, 2008.

[99] H. Omidvar, F. Mirzaei, M. Rahimi and Z. Sadeghian, "A method for coating carbon nanotubes with titanium," *New Carbon Materials*, vol. 27, no. 6, pp. 401-408, 2012.

[100] P. Zhang, C. Shao, Z. Zhang, M. Zhang, J. Mu, Z. Guo and Y. Lui, "TiO_2@carbon core/shell nanofibers: controllable preparation and enhanced visible photocatalytic properties," *Nanoscale*, vol. 3, pp. 2934-2949, 2011.

[101] W. Zhang, B. Xu and L. Jaing, "Functional hybrid materials based on carbon nanotubes and metal oxides," *Journal of Materials Sciences*, vol. 20, pp. 6383-6391, 2010.

[102] A. Kuvarenga, R. M. Krause and B. B. Mamba, "Multi-walled carbon nanotubes decorated with nitrogen, palladium co-doped TiO_2 (MWCNT/N, Pd co-doped TiO_2) for visible light photocatalytic degradation of eosin yellow in water," *Journal of Nanoparticle Research*, vol. 14, no. 776, pp. 1-16, 2012.

[103] H. Brune and K. Kern, “Heteroepitaxial metal growth: the effects of strain” in Growth and properties of ultrathin epitaxial layers, D.A. King and D. P. Woodruff, Ed., Elsevier Science B.V., 1997, pp. 149-226.

[104] I. Gosens, A. J. Post, L. J. De La Fonteyne, H. E. Jansen, W. J. Geus, R. F. Cassee and W. H. De Jong, “Impact of agglomeration state of nano- and submicron sized gold particles on pulmonary inflammation,” *Particle and Fibre Toxicology*, vol. 7, no. 37, pp. 1-11, 2010.

[105] Y. Sato, K. Shibata, H. Kataoka, Ogino. S, F. Bunshi, A. Yokoyama, K. Tamura, T. Akasaka, M. Uo, K. Motomiya, B. Jeyadevan, R. Hatakeyama, F. Watari and K. Tohji, “Strict preparation and evaluation of water-soluble hat-stacked carbon nanofibers for biomedical application and their high biocompatibility: influence of nanofiber-surface functional groups on cytotoxicity,” *Molecular BioSystems*, vol. 1, pp. 142-145, 2005.

[106] D. T. Carpenter, J. M. Rickman, and K. Barmak, “A methodology for automated quantitative microstructural analysis of transmission electron micrographs,” *Journal of Applied Physics*, vol. 84, no. 11, pp. 5843-5854, 1998.

[107] P. J. Franklyn, “Hydrothermal synthesis and characterisation of titania nanoparticles,” University of the Witwatersrand, MSc, 2007.